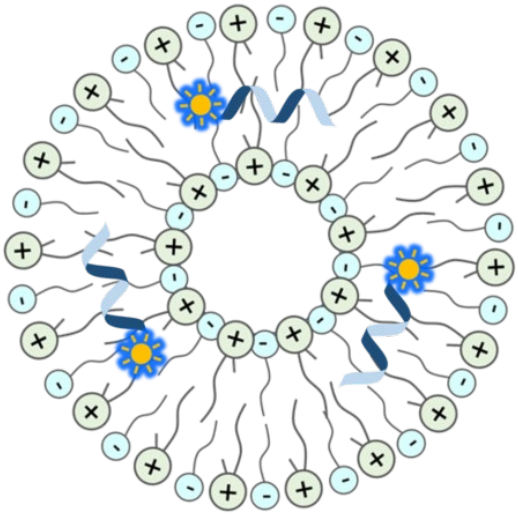


Targeting HER2-positive cell lines by transmembrane peptide based surface-active ionic liquid nanoformulation

Author: Siyuan Liu
Supervisor: Alesia A. Tietze, Volkan Sayin
Examiner: Alexandra Stubelius

DEPARTMENT OF LIFE SCIENCES

CHALMERS UNIVERSITY OF TECHNOLOGY
Gothenburg, Sweden, 28 October 2026
www.chalmers.se

ABSTRACT

Human epidermal growth factor receptor 2 (HER2/ErbB2) is a major oncogenic driver in many cancers, and its extracellular or intracellular domains are the main therapeutic targets. In contrast, the transmembrane domain (TMD), which also plays an important role in receptor dimerization and activation, remains comparatively underexplored as a potential therapeutic target. In this study, ErbB2 TMD-derived peptides were investigated as potential competitive inhibitors of receptor dimerization, while a nicotinium-based biamphiphilic surface-active ionic liquid (Nic BAIL) was developed as a vesicular carrier to address the poor aqueous compatibility of highly hydrophobic transmembrane peptides.

Three ErbB2-TM peptide variants (v1-v3) were purified and characterized by LC-MS. Nic BAIL was synthesized and characterized by NMR, direct-infusion ESI-MS and differential scanning calorimetry (DSC). The Nic BAIL-v3 nanoformulation was prepared and characterized by dynamic light scattering (DLS) and cryogenic transmission electron microscopy (Cryo-TEM), and its colloidal stability was evaluated under storage and dilution conditions. Planar bilayer electrophysiology was employed to investigate membrane activity, while cellular activity was evaluated in BT-474 and NCI-H23 cells, representing high and low ErbB2 expression, respectively. In addition, live-cell imaging was performed to observe morphological changes after treatment.

Nic BAIL formed nanoscale vesicular assemblies, with a predominant nanoscale population maintained following formulation with v3 peptide, although the formulation exhibited time- and concentration-dependent changes in hydrodynamic size and dispersity. Planar bilayer electrophysiology showed that Nic BAIL-v3 increased ionic conductance and decreased electrical resistance across artificial DPhPC bilayers, indicating strongly altered membrane barrier properties. In cell viability assays, free v3 peptide produced similar concentration-dependent effects on BT-474 and NCI-H23 cells, while Nic BAIL-v3 produced an additional significant reduction in BT-474 viability compared to Nic BAIL alone. This enhancement was not observed in NCI-H23 cells. Live-cell imaging further demonstrated sustained cell-associated FAM-v3 fluorescence and progressive morphological deterioration without pronounced acute loss of membrane integrity.

In this thesis, Nic BAIL was developed as a self-assembling membrane-active carrier for delivery of highly hydrophobic ErbB2-derived peptides and that Nic BAIL-v3 formulation exhibited a cell-line-dependent biological effect. But the intrinsic inhibitory activity of Nic BAIL complicates interpretation of observed cellular effects. Peptide loading, membrane localization, HER2-specific targeting, and direct interactions between v3 and HER2-TMD remain unconfirmed and require further investigation.

Keywords: HER2; ERBB2; transmembrane peptide; surface-active ionic liquid; vesicle formulation

Contents

1. Background Information 1
1.1 HER2-positive cancer biology 1
1.1.1 Definition, diagnosis and therapeutic importance of HER2-positive cancers 1
1.1.2 Structure of the HER-family receptors and the molecular basis of HER2 activation 2
1.1.3 HER2-associated signaling networks 4
1.1.4 HER2-targeted therapies 7
1.2 Ionic liquids 12
1.2.1 Concept and fundamental physicochemical properties of ionic liquids 12
1.2.2 Surface-active ionic liquids: molecular design, interfacial activity and self-assembly 13
1.2.3 Biomedical and therapeutic applications of surface-active ionic liquids 15
2. Aim of the project 20
3. Results and discussion 21
3.1 Synthesis and characterization of nicotinium-based bi-amphiphilic surface-active ionic liquid (Nic BAIL) 21
3.2 Purification and characterization of ErbB2-TM peptides 23
3.3 Physicochemical characterization of Nic BAIL vesicles and Nic BAIL-v3 complexes 25
3.4 Planar bilayer electrophysiology of Nic BAIL-v3 formulations 32
3.5 In vitro effects on cell viability in cell lines with different HER2/ERBB2 status 34
4. Conclusions and Perspectives 39
5. Experimental Section 40
5.1 Synthesis of nicotinium-based bi-amphiphilic surface-active ionic liquid (Nic BAIL) 40
5.1.1 Synthesis of dodecyl 2-bromoacetate 40
5.1.2 Synthesis of (R)-1-(2-(dodecyloxy)-2-oxoethyl)-3-(1-methylpyrrolidin-2-yl)pyridin-1-ium bromide (Nic MAIL) 40
5.1.3 Synthesis of (R)-1-(2-(dodecyloxy)-2-oxoethyl)-3-(1-methylpyrrolidin-2-yl)pyridin-1-ium dodecyl sulfate (Nic BAIL) 41
5.2 Characterization of Nic BAIL 41
5.2.1 Nuclear magnetic resonance (NMR) spectroscopy analysis 41
5.2.2 Differential scanning calorimetry (DSC) measurement 41
5.2.3 Direct-infusion ESI-MS characterization 41
5.3 Purification of ErbB2-TM peptides (v1, v2, v3) 42
5.3.1 Preparative HPLC purification 42
5.3.2 Analytical HPLC analysis 42
5.3.3 LC-MS analysis 42
5.4 Generation of Nic BAIL vesicles and incorporation of peptides 42
5.5 Characterization of vesicle-peptide complexes 43
5.5.1 Dynamic light scattering (DLS) measurement 43

5.5.2 Cryogenic transmission electron microscopy (Cryo-TEM) imaging 43
5.5.3 Planar bilayer electrophysiology of the vesicle-peptide complexes 43
5.6 In vitro cell experiments with Nic BAIL-v3 nanoformulation 44
5.6.1 Cell lines and culture 44
5.6.2 Cell viability assay 44
5.6.3 Live cell imaging 44
5.7 Statistical Analysis 44
Acknowledgements 45
Statement on the Use of AI Tools 46
References 47
Appendix 62

List of Abbreviations

ACN	Acetonitrile
ADC	Antibody-drug conjugate
ADCC	Antibody-dependent cellular cytotoxicity
ADCP	Antibody-dependent cellular phagocytosis
Akt	Protein kinase B
ANOVA	Analysis of variance
ASCO	American Society of Clinical Oncology
ATCC	American Type Culture Collection
BAIL	Bi-amphiphilic ionic liquid
BSA	Bovine serum albumin
CAC	Critical aggregation concentration
CAP	College of American Pathologists
CMC	Critical micelle concentration
CPP	Critical packing parameter
Cryo-TEM	Cryogenic transmission electron microscopy
CV	Column volume
CVC	Critical vesicle concentration
DAR	Drug-to-antibody ratio
DCM	Dichloromethane
DLS	Dynamic light scattering
DM1	Mertansine (maytansinoid cytotoxic payload)
DXd	Exatecan-derived topoisomerase I inhibitor payload
DPhPC	1,2-Diphytanoyl-sn-glycero-3-phosphocholine
DSC	Differential scanning calorimetry
ECD	Extracellular domain
EGF	Epidermal growth factor
EGFR	Epidermal growth factor receptor
ERK	Extracellular signal-regulated kinase
ESI	Electrospray ionization
FA	Formic acid
FAK	Focal adhesion kinase
FAM	5-Carboxyfluorescein
FBS	Fetal bovine serum
FDA	U.S. Food and Drug Administration
FRET	Förster resonance energy transfer
HC_{50}	Concentration causing 50% hemolysis
HER2	Human epidermal growth factor receptor 2
HFIP	1,1,1,3,3,3-Hexafluoro-2-propanol
HPLC	High-performance liquid chromatography
HAS	Human serum albumin
IC_{50}	Half-maximal inhibitory concentration
IgG1	Immunoglobulin G1
IHC	Immunohistochemistry
IL	Ionic liquid
IL-6	Interleukin-6
IP3	Inositol 1,4,5-trisphosphate
ISH	In situ hybridization
ITC	Isothermal titration calorimetry

JAK	Janus kinase
JMS	Juxtamembrane segment
LC-MS	Liquid chromatography-mass spectrometry
MAIL	Mono-amphiphilic ionic liquid
MAPK	Mitogen-activated protein kinase
mAbs	Monoclonal antibodies
MCC	4-(N-Maleimidomethyl)cyclohexane-1-carboxylate
MEK	Mitogen-activated protein kinase kinase
MeOH	Methanol
mTORC2	Mechanistic target of rapamycin complex 2
Nic BAIL	Nicotinium-based bi-amphiphilic ionic liquid
Nic MAIL	Nicotinium-based mono-amphiphilic ionic liquid
NIR	Near-infrared
NMR	Nuclear magnetic resonance
NSCLC	Non-small-cell lung cancer
OG	n-Octyl-β-D-glucopyranoside
PB	Phosphate buffer
PC	Polycarbonate
PDA	Photodiode array
PDI	Polydispersity index
PDK1	3-Phosphoinositide-dependent protein kinase 1
PEG4	Polyethylene glycol spacer containing four ethylene glycol units
PI	Propidium iodide
PI3K	Phosphoinositide 3-kinase
PIP2	Phosphatidylinositol 4,5-bisphosphate
PIP3	Phosphatidylinositol 3,4,5-trisphosphate
PKC	Protein kinase C
PLCγ	Phospholipase C gamma
Pro BAIL	Prolinium-based bi-amphiphilic ionic liquid
PTEN	Phosphatase and tensin homolog
PTFE	Polytetrafluoroethylene
PTSA	p-Toluenesulfonic acid
RAF	RAF family of serine/threonine protein kinase
RAS	Rat sarcoma family of small GTPases
RC	Resistance-capacitance
RTK	Receptor tyrosine kinase
SAIL	Surface-active ionic liquid
SD	Standard deviation
SDS	Sodium dodecyl sulfate
SFK	Src family kinase
SH2	Src homology 2
STAT3	Signal transducer and activator of transcription 3
T-DM1	Trastuzumab emtansine
T-DXd	Trastuzumab deruxtecan
TFA	Trifluoroacetic acid
TKD	Tyrosine kinase domain
TKI	Tyrosine kinase inhibitor
TLC	Thin-layer chromatography
TMD	Transmembrane domain

1. Background Information

1.1 HER2-positive cancer biology

1.1.1 Definition, diagnosis and therapeutic importance of HER2-positive cancers

HER2-positive cancers are malignant tumors classified according to tumor-specific pathological criteria as exhibiting clinically significant overexpression of the human epidermal growth factor receptor 2 protein and/or amplification of its encoding gene, ErbB2. Although HER2 overexpression and ErbB2 amplification occur across several solid-tumor types, their diagnostic assessment and clinical application have been most extensively established in breast cancer and gastric or gastroesophageal junction adenocarcinoma[1,2].

In breast cancer, HER2 status is determined primarily using immunohistochemistry (IHC) and in situ hybridization (ISH). IHC assesses the abundance and membrane-localization pattern of HER2 protein in the invasive tumor component, whereas ISH evaluates amplification of the ErbB2 locus. According to the 2023 ASCO-CAP guideline update, IHC 3+ is defined by complete, intense circumferential membrane staining in more than 10% of invasive tumor cells and is interpreted as HER2 positive. IHC 2+ corresponding to weak-to-moderate complete membrane staining in more than 10% of tumor cells is considered equivocal and requires reflex ISH testing or repeat testing on another suitable specimen. If the result is IHC 2+/ISH-non-amplified, it is considered negative for HER2 overexpression or gene amplification. IHC 0 and 1+ are still interpreted as negative for HER2 protein overexpression. Although the term “HER2-low” has been used clinically for IHC 1+ or IHC 2+/ISH-negative metastatic breast cancers, the 2023 ASCO-CAP update does not endorse it as a distinct pathological interpretive category. Instead, laboratories are advised to report specific IHC score together with the conventional HER2 interpretation, thereby enabling better targeted treatment for different patients[1,3].

The definition and scoring of HER2 positivity are tumor-type specific and should not be transferred directly between different malignancies. In advanced gastric and gastroesophageal junction adenocarcinoma, HER2 testing is also generally initiated using IHC, with reflex ISH performed for IHC 2+ cases. However, glandular polarity in gastroesophageal tumors often results in strong basolateral or lateral membrane staining rather than the complete circumferential staining expected in breast cancer. Such staining can satisfy gastric-specific HER2-positive criteria even when it would not qualify as IHC 3+ under the breast cancer scoring system[2,4]. In surgical resection specimens, an IHC score of 3+ generally requires strong complete, basolateral, or lateral membrane staining in at least 10% of tumor cells. In biopsy specimens, a cohesive cluster of at least five tumor cells showing strong complete, basolateral, or lateral membrane staining may be classified as IHC 3+, irrespective of the overall percentage of positive cells. Evaluation of multiple biopsy fragments is therefore important for reducing sampling error and improving detection of focal HER2-positive tumor populations[2,4].

Accurate HER2 classification has both prognostic and predictive significance, although the relative importance of these functions varies among different tumor types. Approximately 15-20% of breast cancers and 11-16% of gastric cancers exhibit HER2 overexpression and/or ErbB2 amplification[5,6]. In a large Australian ISH testing program, 15.8% of early breast cancers were classified as HER2 positive. Before the introduction of effective HER2-directed treatment, ErbB2 amplification was associated with shorter time to relapse and reduced overall survival, particularly in lymph-node-positive breast cancer[7]. HER2 status is also associated with distinct clinicopathological patterns in gastric and gastroesophageal junction adenocarcinoma. Screening

data from the ToGA program identified HER2 positivity in 22.1% of evaluable tumors, with higher rates in gastroesophageal junction than gastric cancers and in intestinal-type than diffuse-type tumors[8]. The independent prognostic effect of HER2 in gastroesophageal cancer has been less consistent across individual studies than in historical breast cancer cohorts, partly because of differences in tumor heterogeneity, disease stage, assay methodology, and scoring criteria. Nevertheless, meta-analyses have reported an association between HER2 overexpression and poorer survival in gastric cancer, while its most firmly established clinical role remains the identification of a molecularly selected patient population for HER2-directed treatment[9].

1.1.2 Structure of the HER-family receptors and the molecular basis of HER2 activation

The human epidermal growth factor receptor (HER/ErbB) family belongs to the receptor tyrosine kinase (RTK) superfamily and has four homologous members: HER1 (EGFR /ERBB1), HER2 (ErbB2), HER3 (ErbB3), and HER4 (ErbB4)[10]. All four receptors share a conserved overall modular organization consisting of an N-terminal extracellular domain (ECD), a single-pass α-helical transmembrane domain (TMD), and an intracellular region composed of a juxtamembrane segment (JMS), a bilobed tyrosine kinase domain (TKD), and a C-terminal tail containing multiple regulatory tyrosine residues. Despite this conserved architecture, the receptors differ substantially in ligand-binding properties, kinase activity, conformational regulation, and dimerization preference[11-14].

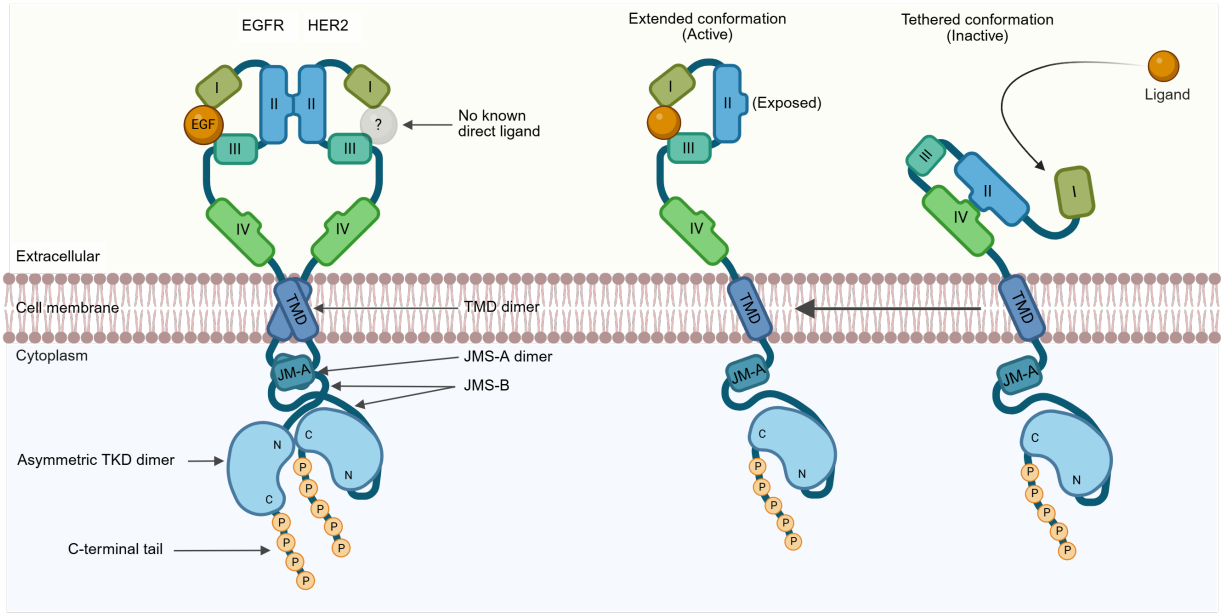


Figure 1. Schematic diagram of tethered and extended conformation of receptor and EGFR-HER2 heterodimer. The diagram illustrates the organization of the extracellular, transmembrane, juxtamembrane, and intracellular kinase domains, together with receptor dimerization and activation-associated phosphorylation. Created with BioRender.com.

The ECD of each HER-family receptor can be divided into four subdomains (I-IV). Domain I (L1) and Domain III (L2) are leucine-rich regions that form the principal ligand-binding surfaces in ligand-responsive family members, whereas Domain II (CR1) and Domain IV (CR2) are cysteine-rich modules involved in conformational regulation, receptor-receptor interactions, and positioning of the ECD relative to the membrane. In ligand-responsive family members (HER1, HER3, and HER4), the ligand binds through a composite interface formed by domains I and III, thereby stabilizing an ECD arrangement competent for receptor dimerization [15]. For HER1, the known activating ligands include epidermal growth factor (EGF), transforming

growth factor-α (TGF-α), amphiregulin (AREG), heparin-binding EGF-like growth factor (HB-EGF), betacellulin (BTC), epiregulin (EPR), and epigen (EPG). HER3 binds primarily to neuregulin-1 (NRG1) and neuregulin-2 (NRG2), whereas HER4 responds to several neuregulins as well as selected EGF-family ligands, including HB-EGF and BTC[16-19]. Structural studies of the unliganded ECD of EGFR, HER3, and HER4 revealed a compact, tethered arrangement in which the domain II dimerization arm contacts the membrane-proximal region of domain IV. This intramolecular interaction reduces the accessibility of the dimerization arm and contributes to extracellular autoinhibition. Ligand binding between domains I and III reshapes this tethered arrangement between domains II and IV and stabilizes an extended, dimerization-competent receptor conformation in which the dimerization arm in domain II becomes available for intermolecular receptor interaction. Two extended ligand-bound receptor molecules can consequently form a back-to-back extracellular dimer[12-14,16,20]. Within this family, HER2 is structurally distinct from the ligand-binding members. In the available ligand-free HER2 ECD structures, domains I-IV adopt an extended arrangement in which the domain II dimerization arm is exposed rather than sequestered by a classical tethered conformation. This conformational feature makes HER2 the preferred dimerization partner for ligand-activated HER receptors and contributes to its prominent role in amplifying signaling output. Productive HER2 activation also depends on receptor abundance, dimer-partner identity, membrane-proximal geometry, and assembly of the intracellular domains[14,21,22].

Downstream of the ECD, each receptor contains a single-pass hydrophobic transmembrane α-helix that participates actively in signal transmission rather than just functioning as a membrane anchor[23]. Interaction between ECDs is coupled to helix-helix association of the TMDs within the membrane, which in turn regulates the organization of the intracellular JMS and TKD[24]. Structural studies of the isolated HER2 TMD identified a symmetric, right-handed dimer mediated by an N-terminal small-residue interface centered on the T652xxxS656xxxG660 motif, which was proposed to represent an activation-compatible conformation. Other studies also identified alternative HER2 TMD packing arrangements, suggesting that HER2 may interconvert between multiple membrane-embedded dimer conformations that may correspond to different effects on kinase activity[25-28]. Because these structures were obtained using isolated TMD or TMD-JMS fragments in membrane-mimetic systems, their assignment to definitive full-length active and inactive states should remain appropriately qualified.

Adjacent to the C-terminus of the TMD is the JMS, which functions as an allosteric coupler between the transmembrane helices and the catalytic intracellular regions. In the activation mechanism established most clearly for EGFR, the JMS can be divided into JMS-A and JMS-B subregions. Ligand-dependent receptor rearrangement promotes formation of an antiparallel helical association between the two JMS-A segments, whereas JMS-B from the activator protomer forms a juxtamembrane latch that helps stabilize the receiver kinase[28,29]. Although this structural model is best established for EGFR, sequence conservation and functional studies support its broader relevance to the HER family[30,31]. Mutational and structural studies have further shown that alterations in the HER2 TMD and JMS can enhance receptor phosphorylation and transforming activity by stabilizing activation-compatible membrane-proximal interactions or altering the geometry transmitted to the kinase domains, underscoring the functional importance of this region[32].

The HER-family TKD consists of a smaller N-terminal lobe and a larger C-terminal lobe separated by an ATP-binding cleft. In this configuration, the C-lobe of one kinase domain (the activator) contacts the N-lobe of the partner kinase domain (the receiver). Catalytic activation is

primarily driven by this interaction, which allosterically reorganizes the receiver kinase into a catalytically active conformation without requiring activation-loop phosphorylation as the principal activation switch. This mechanism was best established for EGFR and subsequently supported for other HER-family receptor combinations. The JMS is structurally compatible with this asymmetric kinase assembly and thereby couples membrane-proximal receptor rearrangements to the activation of the intracellular kinase[29,33,34].

Distal to the kinase domain, the C-terminal tail is highly dynamic and widely regarded as a largely intrinsically disordered regulatory region. The tail's conformational flexibility permits multiple tyrosine residues to become accessible to the activated kinase and to cytosolic signaling proteins. Following receptor activation, phosphorylation of these residues creates sequence-specific docking sites for proteins containing Src homology 2 or phosphotyrosine-binding domains. In this way, the C-terminal tail acts as a flexible phosphotyrosine display platform that recruits adaptor proteins and regulatory components required for activation of downstream pathways[35-39]. Taken together, activation of HER-family receptors is a coordinated, multilevel allosteric process involving ECD conformational rearrangement and dimerization, TMD packing, organization of the JMS, formation of an asymmetric kinase dimer, and phosphorylation-dependent assembly of signaling complexes on the C-terminal tails. HER2 occupies a distinctive position within this system because its extended and dimerization-competent ECD, catalytically active kinase domain, and compatibility with other HER-family partners enable it to amplify both ligand-dependent and, when overexpressed, ligand-independent signaling.

1.1.3 HER2-associated signaling networks

1.1.3.1 PI3K-Akt signaling pathway

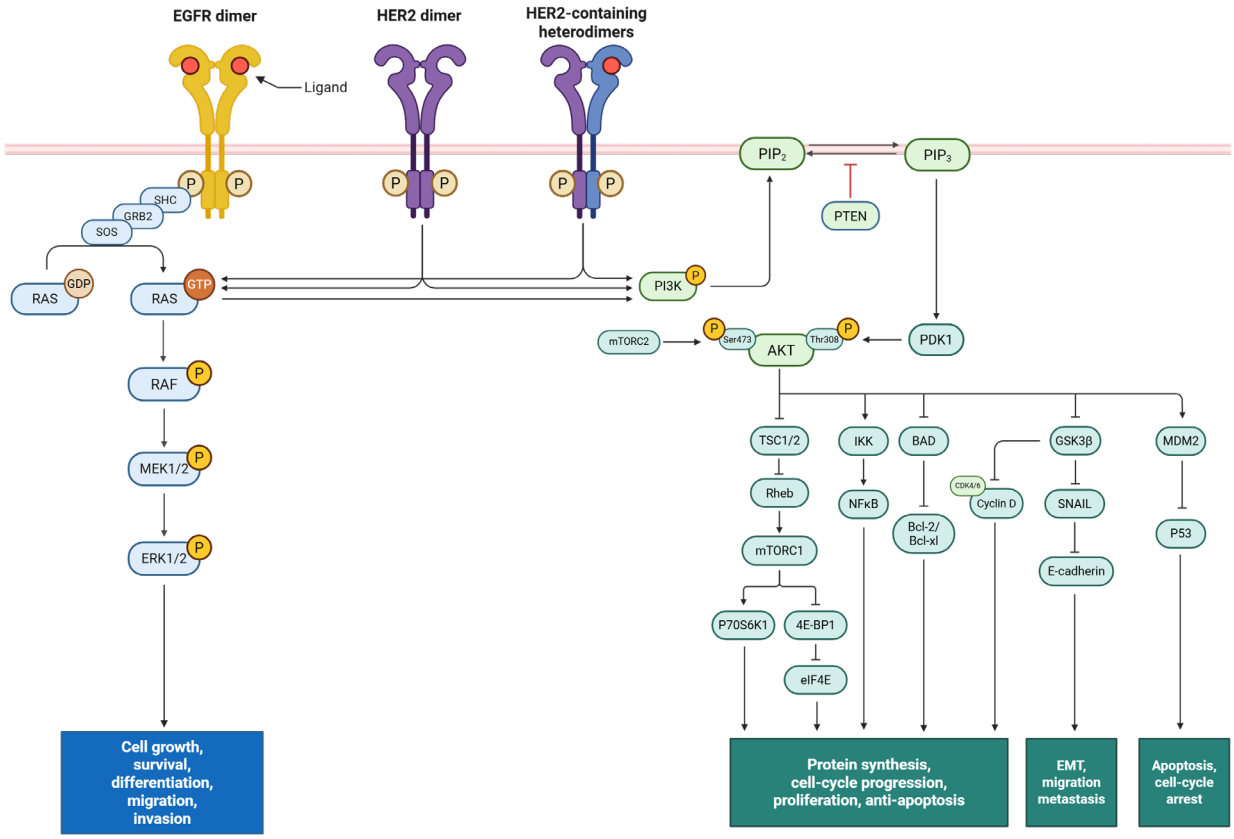


Figure 2. Schematic diagram of HER2-associated signaling pathways. The diagram illustrates signaling through the PI3K-Akt and RAS-RAF-MEK-ERK pathways downstream of HER2 receptor complexes, together with regulatory proteins and downstream cellular responses. Created with BioRender.com.

Among the pathways activated by HER2-containing receptor complexes, the phosphatidylinositol 3-kinase (PI3K)-Akt pathway is a major regulator of HER2-driven tumor cell growth, metabolism and survival. The HER2-HER3 heterodimer is widely regarded as one of the most potent HER-family signaling units for activation of class IA PI3K. Within this complex, HER2 provides the catalytically active kinase, whereas HER3 functions primarily as an efficient receptor-associated scaffold for PI3K recruitment and activation. Upon heterodimerization, the HER2 kinase phosphorylates tyrosine residues within the C-terminal tail of HER3[40-43]. This tail contains six canonical YXXM motifs that can bind the Src homology 2 domains of the p85 regulatory subunit of class IA PI3K. The presence of multiple YXXM motifs enables strong and efficient recruitment of p85 together with its associated p110 catalytic subunit to the plasma membrane[44,45]. In tumors with high-level HER2 overexpression and phosphorylation, the p85 regulatory subunit can bind directly to phosphorylated HER2, but this direct interaction is comparatively weak and becomes quantitatively important under overexpression conditions[42,46]. Therefore, HER3-mediated recruitment remains the predominant and generally more efficient route linking HER2 activation to PI3K activation. Once localized to the plasma membrane, the p110 catalytic subunit of PI3K phosphorylates phosphatidylinositol-4,5-bisphosphate (PIP2) to generate phosphatidylinositol-3,4,5-trisphosphate (PIP3). PIP3 functions as a membrane-associated second messenger that recruits proteins containing pleckstrin homology domains, including Akt and 3-phosphoinositide-dependent protein kinase 1. Membrane colocalization enables PDK1 to phosphorylate Akt at Thr308 within its activation loop, whereas mammalian target of rapamycin complex 2 (mTORC2) phosphorylates the hydrophobic-motif residue Ser473. Together, these phosphorylation events promote complete Akt activation[47,48]. Under conditions of HER2 overexpression or amplification, HER2 and HER3 can form ligand-independent signaling complexes that maintain PI3K-Akt activity[49]. The pathway is negatively regulated by the tumor suppressor PTEN, a lipid phosphatase that converts PIP3 back to PIP2 and therefore limits the abundance of membrane PIP3 and restricts the recruitment and activation of Akt[50]. The pathway can also remain constitutively and persistently activated through alterations downstream of the receptor complex. For example, activating mutations in PIK3CA, which encodes the p110α catalytic subunit, or loss of PTEN function can maintain PI3K-Akt signaling despite reduced upstream receptor input[51]. Activated Akt phosphorylates numerous substrates involved in protein synthesis, glucose and lipid metabolism, cell-cycle progression, suppression of apoptosis and adaptation to cellular stress. Therefore, it can promote malignant progression and reduce sensitivity to HER2-directed pathway inhibition, resulting in decreased treatment responsiveness and poor prognosis[42,46,52].

1.1.3.2 MAPK/ERK signaling pathway

In parallel with PI3K-Akt signaling, the RAS-RAF-MEK-ERK pathway represents a major downstream effector of HER2-containing receptor complexes. Phosphorylated HER-family receptors recruit adaptor complexes containing Shc and Grb2. Grb2 may associate directly with selected receptor phosphotyrosine motifs or indirectly through phosphorylated Shc, while its Src homology 3 domains interact with the guanine nucleotide exchange factor SOS. Recruitment of SOS to the plasma membrane promotes the exchange of GDP for GTP on RAS, generating active RAS-GTP. RAS-GTP recruits and activates RAF-family kinases, which phosphorylate and activate MEK1 and MEK2. MEK1/2 subsequently phosphorylate ERK1/2 within their activation motifs. Activated ERK1/2 phosphorylates a broad range of regulatory substrates, promoting

proliferative gene expression, cell-cycle entry, survival under selected stress conditions and cytoskeletal programs involved in migration and invasion[37,53,54]. In HER2-driven tumors, the MAPK/ERK signaling pathway functionally complements PI3K-Akt, and overlap and cross-regulation also occur between the two pathways. The relative contribution of each pathway depends on receptor composition, genetic background and treatment context. In HER2-overexpressing breast cancer models, pharmacological PI3K inhibition relieved negative feedback restriction on upstream HER-family receptors, resulting in increased receptor phosphorylation and compensatory ERK activation. Cells exposed to prolonged PI3K inhibition consequently acquired increased dependence on ERK signaling for continued survival[55]. The activation of RAS-MAPK signaling can also reduce tumor dependence on HER2. In metastatic HER2-positive breast cancer, alterations associated with increased RAS pathway output, including the loss of the RAS GTPase-activating protein NF1, were enriched in tumors with poor responses to HER2-targeted therapy. Experimental NF1 depletion increased MAPK activity, reduced sensitivity to HER2 inhibition and shifted cell cycle regulation from AKT-dependent to MEK-ERK-dependent control[56]. Additional feedback activation has been observed after repeated HER2 kinase inhibition. For example, prolonged lapatinib exposure can increase RAF, MEK and ERK phosphorylation in HER2-positive breast cancer cells, providing further evidence that suppression of Akt signaling may redirect signaling flux toward the MAPK pathway[57]. In summary, these findings demonstrate that PI3K-Akt and MAPK/ERK constitute a dynamically coordinated signaling network, and therapeutic suppression of one branch may alter feedback regulation and increase dependence on the other.

1.1.3.3 Other signaling pathways

In addition to the PI3K-AKT and MAPK/ERK pathways, the HER2-containing receptor complex activates several other signaling pathway modules, including the PLCγ-PKC pathway, the STAT3-centered signaling pathways, and the Src-FAK-dependent adhesion pathways. These context-dependent pathways cooperate with the two major pathways described above to regulate cancer cell transcriptional plasticity, migration, invasion and adaptation to environmental or therapeutic stress.

The PLCγ/PKC pathway is an important accessory pathway. Phospholipase C-γ (PLCγ) can be recruited to activated receptor tyrosine kinase complexes through its SH2 domains and is activated by tyrosine phosphorylation. Activated PLCγ hydrolyzes PIP2 to generate inositol-1,4,5-trisphosphate and diacylglycerol. IP3 binds to receptors on the endoplasmic reticulum and promotes the release of Ca^{2+} from intracellular stores. DAG remains within the plasma membrane, and together with Ca^{2+}, promotes activation of protein kinase C (PKC). These Ca^{2+}- and PKC-dependent responses regulate cytoskeletal organization, secretion, proliferation and cell motility. In HER2-expressing breast cancer models, PLCγ1 activation has been particularly associated with EGFR-HER2-containing receptor complexes, rather than representing a defining output of the HER2-HER3 dimer. Balz et al. demonstrated functional cooperation between EGFR-HER2-PLCγ1 and HER2-HER3-PI3K signaling in an EGFR/HER2/HER3-expressing breast cancer model. HER3 depletion reduced Akt activation but also altered EGF-induced PLCγ1 activation and cell migration, indicating cross-regulation between the survival and motility branches[58]. These findings suggest that HER2-containing receptor complexes can coordinate PI3K-dependent survival signaling and PLCγ1-dependent motility programs, although the relative importance of this mechanism may vary considerably according to the cellular context.

HER2-driven tumors can also converge on STAT3 signaling, although the molecular

connection is less uniform than that of the PI3K or MAPK pathways. Depending on cellular context, STAT3 activation may involve autocrine cytokine production, JAK-family kinases, Src-family kinases, focal adhesion-associated proteins or other receptor-linked intermediates. Hartman et al. demonstrated that HER2 overexpression induced IL-6 secretion, which activated STAT3 and reinforced an IL-6–STAT3 transcriptional circuit. Both murine and human HER2-amplified breast cancer models showed functional dependence on this pathway, linking HER2 overexpression to inflammatory signaling and tumorigenesis[59]. Subsequent studies showed that inhibition of the IL-6–JAK2–STAT3 axis could suppress HER2-positive tumor growth and enhance the effects of HER2-directed therapy in experimental models[60]. In HER2-overexpressing breast cancer cells, increased STAT3 phosphorylation has also been associated with epithelial–mesenchymal transition, tumorsphere formation and increased expression of stem cell-associated markers, including OCT4, SOX2 and CD44. Pharmacological inhibition of STAT3 reduced these stem-like phenotypes, supporting a functional role for STAT3 in HER2-associated transcriptional plasticity[61]. Clinical-translational evidence further links STAT3 activity with treatment outcome. In primary HER2-positive breast cancer specimens, a constitutive phosphorylated-STAT3-associated gene-expression signature was associated with reduced benefit from trastuzumab-containing therapy, supporting the regulatory role for STAT3 in therapeutic adaptation[62].

HER2 signaling also intersects with Src family kinase (SFK) and focal adhesion kinase (FAK), which regulate cell-matrix adhesion, cytoskeletal dynamics and invasion. FAK is activated through both integrin engagement and growth factor receptor signaling and therefore functions as an integration hub rather than as a purely linear downstream component of HER2. Activated FAK forms signaling complexes with Src, resulting in phosphorylation of focal-adhesion-associated proteins and regulation of adhesion assembly, disassembly and cytoskeletal remodeling. Previous studies have shown that FAK signaling was required for oncogenic transformation and invasion driven by cooperative HER2-HER3 signaling[63]. Genetic or pharmacological interference with FAK markedly reduced the transforming and invasive effects of the receptor pair. Consistent with this finding, subsequent studies have shown that HER2 signaling regulated focal-adhesion turnover and invasive behavior through the Src-FAK axis. Inhibition of HER2 signaling reduced HER2-Src association, decreased Src and FAK activity, stabilized peripheral focal adhesions and suppressed cell migration and invasion[64,65]. FAK inhibition has shown antitumor activity in ER-positive/HER2-positive breast cancer models, further illustrating that HER2 signaling interacts with adhesion-dependent signaling pathways[66].

In summary, these additional signaling modules extend the biological consequences of HER2 activation. They integrate with the PI3K-AKT and MAPK/ERK signaling pathways, creating a flexible regulatory network capable of supporting tumor growth, dissemination and adaptation to changing environmental or therapeutic conditions.

1.1.4 HER2-targeted therapies

Established HER2-targeted therapies can be grouped into three major classes: monoclonal antibodies (mAbs), antibody-drug conjugates (ADCs), and tyrosine kinase inhibitors (TKIs). These therapies target different structural and functional properties of HER2. Monoclonal antibodies recognize extracellular epitopes and modulate receptor function while recruiting immune effector mechanisms. ADCs use HER2 as a tumor-associated surface antigen to facilitate the selective delivery of cytotoxic payloads. TKIs inhibit the intracellular kinase activity of HER2 and other members of the HER receptor family depending on the selectivity profiles.

1.1.4.1 Monoclonal antibodies (mAbs)

Monoclonal antibodies (mAbs) were the first major class of HER2-targeted drugs to demonstrate clinical efficacy and remain a core component of HER2-directed therapy. Trastuzumab is a humanized immunoglobulin G1 (IgG1) mAb that binds to subdomain IV of the HER2 extracellular domain. Because its epitope is distinct from the canonical dimerization interface located in subdomain II, trastuzumab does not directly inhibit HER2 dimerization. Recent structural analysis demonstrated that trastuzumab binding can stabilize an alternative conformation of the HER2 extracellular domain, which may result in reduced compatibility with HER3 binding, a high-affinity binding partner of HER2, thereby preventing the activation of downstream signaling[67,68]. These findings suggest that receptor conformational adaptation may contribute to the attenuation of selected HER2-containing receptor assemblies and their signaling competence[69]. Nevertheless, the effects of trastuzumab on HER2 homo- and heterodimerization appear to be context-dependent, and the precise contribution of this structural mechanism to its overall antitumor activity remains under investigation.

A major component of trastuzumab activity is its capacity to recruit Fcγ receptor-bearing immune effector cells. Following binding of the Fab (fragment antigen-binding) region to HER2 on the tumor-cell surface, the exposed Fc (fragment crystallizable) region interacts with Fcγ receptors on immune effector cells. Clinical and translational evidence supports the conclusion that the engagement of FcγR on natural killer cells promotes antibody-dependent cellular cytotoxicity (ADCC) contributes to trastuzumab-mediated HER2-positive tumor cells killing[70]. Additionally, Shi et al. demonstrated that the engagement of FcγR on macrophages can induce antibody-dependent cellular phagocytosis (ADCP), enabling macrophages to phagocytose and eliminate HER2-high tumor cells both in vitro and in vivo, supporting ADCP as an additional mechanism of action[71]. Trastuzumab may also affect HER2 receptor processing. Molina et al. demonstrated that trastuzumab inhibited both basal and experimentally activated cleavage of the HER2 extracellular domain in breast cancer cells[72]. Inhibition of ectodomain shedding may limit the formation of signaling-competent truncated HER2 species while preserving the extracellular antibody-binding region. In addition, preclinical xenograft studies have reported antiangiogenic and antimetastatic effects of trastuzumab. For example, Lange et al. observed reduced angiogenesis and metastatic dissemination in a spontaneous-metastasis xenograft model of HER2-positive esophageal adenocarcinoma[73]. However, these effects are best regarded as supportive and context-dependent components of trastuzumab activity rather than universally established primary mechanisms.

Pertuzumab is another humanized HER2-targeted mAb, but it recognizes an epitope within subdomain II of the HER2 extracellular domain, which contains the principal extracellular dimerization interface. By occupying subdomain II, pertuzumab sterically interferes with ligand-induced HER2 heterodimerization, particularly formation of the highly signaling-competent HER2/HER3 complex[74]. Because phosphorylated HER3 provides multiple essential binding sites for class IA PI3K, suppression of HER2/HER3 assembly reduces one of the most potent routes of HER-family-mediated PI3K-Akt activation[49]. The distinct epitopes and partially complementary mechanisms of trastuzumab and pertuzumab therefore provide a molecular rationale for dual HER2 antibody blockade[75]. The clinical importance of this complementary inhibition was demonstrated in the phase III CLEOPATRA trial. Addition of pertuzumab to trastuzumab and docetaxel significantly improved survival in patients with previously untreated HER2-positive metastatic breast cancer, establishing dual trastuzumab-pertuzumab blockade as an important therapeutic strategy[76].

Additional mAbs have been engineered to enhance specific aspects of HER2 targeting. Margetuximab is a chimeric, Fc-engineered anti-HER2 IgG1 mAbs that shares HER2 epitope specificity and Fc-independent antiproliferative activity with trastuzumab. Its Fc region contains amino-acid substitutions that increase affinity for the activating Fcγ receptor CD16A/FcγRIIIa and decrease affinity for the inhibitory Fcγ receptor CD32B/FcγRIIb. Preclinical studies showed that this Fc engineering enhanced immune-cell activation and ADCC relative to antibodies containing an unmodified IgG1 Fc region[77]. The phase III SOPHIA trial compared margetuximab plus chemotherapy with trastuzumab plus chemotherapy in patients with previously treated HER2-positive advanced breast cancer. Margetuximab produced a statistically significant but quantitatively modest improvement in centrally assessed progression-free survival, with a median progression-free survival of 5.8 months, compared with 4.9 months for trastuzumab. However, the final overall survival (21.6 months in the margetuximab group and 21.9 months in the trastuzumab group) did not demonstrate a statistically significant overall survival advantage[78,79]. These results provided a rationale for improving HER2-targeted therapy through optimization of Fc-Fcγ receptor interactions while also indicating that enhanced Fc-mediated immune engagement does not necessarily translate into a large improvement in clinical outcomes.

1.1.4.2 Antibody-drug-conjugates (ADCs)

Antibody-drug conjugates (ADCs) combine the antigen specificity of monoclonal antibodies with the cytotoxicity of small molecule payloads. Structurally, an ADC consists of three essential components: a tumor-targeting antibody, a chemical linker, and a cytotoxic payload. After binding to HER2 on the surface of tumor cells, HER2-directed ADCs undergo receptor-mediated internalization and intracellular trafficking. Subsequent linker cleavage and/or proteolytic degradation of the antibody component in intracellular compartments releases active drug species, which then induce tumor-cell death.

Trastuzumab emtansine (T-DM1) was the first HER2-directed ADC to receive broad clinical approval. It consists of trastuzumab linked to the maytansinoid microtubule inhibitor DM1 through a stable, non-cleavable maleimidomethyl cyclohexane-1-carboxylate (MCC) thioether linker, with an average drug-to-antibody ratio (DAR) of approximately 3-3.6. T-DM1 selectively binds to HER2-expressing tumor cells via its trastuzumab component. The HER2-T-DM1 complex then undergoes receptor-mediated endocytosis and is trafficked to lysosomes, where the trastuzumab component is degraded by proteases. Because the MCC linker is non-cleavable and remains chemically attached to DM1, intracellular processing generates the principal active catabolite lysine-MCC-DM1 (Lys-MCC-DM1) rather than freely diffusing DM1[80]. The lysosomal membrane transporter SLC46A3 facilitates the export of maytansinoid-containing catabolites from lysosomes into the cytoplasm, where Lys-MCC-DM1 can binds tubulin and disrupt microtubule dynamics, such as microtubule assembly and polymerization[81]. This interferes with mitotic-spindle formation and chromosome segregation, resulting in mitotic arrest and ultimately inducing apoptosis or mitotic catastrophe[82]. Because Lys-MCC-DM1 is positively charged at physiological pH and has poor membrane permeability, it is largely retained within the cell that internalized the ADC. Consequently, T-DM1 has relatively limited bystander cytotoxicity against adjacent cells with low or absent HER2 expression[83]. The clinical efficacy of T-DM1 was established in the phase III EMILIA trial, in which T-DM1 improved progression-free survival and overall survival compared with capecitabine plus lapatinib in patients with HER2-positive advanced or metastatic breast cancer who had previously received trastuzumab and a taxane treatment[84].

Trastuzumab deruxtecan (T-DXd) is a later-generation HER2-targeted ADC with enhanced cytotoxic delivery capacity compared with T-DM1. T-DXd consists of a trastuzumab-derived anti-HER2 antibody conjugated to the exatecan-derived topoisomerase I inhibitor payload DXd through a plasma-stable but enzymatically cleavable tetrapeptide linker. The relative stability of the linker in circulation is intended to limit premature systemic payload release while permitting efficient intracellular drug liberation following target-mediated uptake[85]. Following binding to HER2, the ADC is internalized and trafficked to lysosomal compartments, where proteolytic cleavage of the linker releases the DXd payload. Under normal conditions, topoisomerase I transiently cleaves one strand of DNA to relieve torsional stress generated during replication and transcription and subsequently religates the strand. DXd stabilizes the covalent topoisomerase I-DNA cleavage complex and prevents DNA religation, thereby leading to replication-associated strand breaks and DNA damage, ultimately disrupting cell-cycle progression and inducing apoptosis[86]. The greater activity of T-DXd compared with T-DM1 can be attributed to several design characteristics. First, T-DXd has a DAR of approximately 8, enabling substantially more payload molecules to be delivered per antibody-binding event. Second, its protease-cleavable linker permits release of an unconjugated and pharmacologically active payload rather than a charged amino acid-linker catabolite. Third, released DXd is sufficiently membrane-permeable to diffuse out of the initially targeted cell and enter neighboring tumor cells[87]. This bystander killing effect allows T-DXd to eliminate adjacent cells with lower or absent HER2 expression and is therefore particularly advantageous in tumors with spatially heterogeneous HER2 expression[88]. In mixed HER2-positive and HER2-negative preclinical tumor models, T-DXd produced marked killing of neighboring HER2-negative cells, whereas T-DM1 showed substantially weaker bystander activity[89].

The phase III DESTINY-Breast03 trial demonstrated that T-DXd produced superior progression-free and overall survival compared with T-DM1 in patients with HER2-positive metastatic breast cancer previously treated with trastuzumab and a taxane[90]. The phase III DESTINY-Breast09 trial evaluated T-DXd plus pertuzumab as first-line treatment for HER2-positive metastatic breast cancer, and this combination therapy produced a significantly lower risk of disease progression or death[91]. The clinical application of T-DXd has subsequently expanded both to earlier treatment lines and beyond conventionally defined HER2-positive breast cancer. On 15 December 2025, the US Food and Drug Administration approved Enhertu (fam-trastuzumab deruxtecan-nxki) with pertuzumab for the first-line treatment of adults with unresectable or metastatic HER2-positive (IHC 3+ or ISH+) breast cancer[92]. On 25 June 2026, supported by the DESTINY-PanTumor02[93], DESTINY-Lung01[94] and DESTINY-CRC02[95], the European Commission expanded the indication of T-DXd to include monotherapy for adults with unresectable or metastatic HER2-positive (IHC 3+) solid tumors who had received prior treatment and had no satisfactory alternative treatment options.

1.1.4.3 Tyrosine kinase inhibitors (TKIs)

Lapatinib was one of the earliest HER2-directed TKIs to demonstrate clear clinical utility. It is an orally administered, reversible dual inhibitor of EGFR and HER2 that competes with ATP for binding to their intracellular kinase domains and stabilizes an inactive-like kinase conformation, thereby preventing catalytic activation[96]. In HER2-dependent tumor-cell models, lapatinib reduced receptor phosphorylation and downstream ERK1/2 and Akt activation, resulting in growth arrest and, in susceptible cellular contexts, apoptosis[97]. The clinical activity of lapatinib was demonstrated in a randomized phase III trial involving patients with HER2-positive advanced breast cancer whose disease had progressed after regimens containing

an anthracycline, a taxane and trastuzumab. Lapatinib plus capecitabine significantly prolonged the time to disease progression compared with capecitabine alone[98]. Although its clinical role has subsequently become more limited with the development of more active HER2-directed agents, lapatinib provided important proof of principle that intracellular inhibition of HER2 kinase activity could produce clinical benefit after prior antibody-based treatment.

Neratinib is an orally administered, irreversible pan-HER TKI that directly inhibits EGFR, HER2 and HER4. In contrast to the reversible binding of lapatinib, neratinib contains an electrophilic group that forms a covalent interaction with a conserved cysteine residue within the ATP-binding region of HER-family kinases. This irreversible binding produces sustained suppression of receptor catalytic activity, autophosphorylation and downstream signaling[99]. The clinical efficacy of extended adjuvant neratinib was evaluated in the phase III ExteNET trial. In patients with early-stage HER2-positive breast cancer who had completed trastuzumab-based adjuvant therapy, one year of neratinib significantly improved invasive disease-free survival compared with placebo, and this benefit remained evident in the protocol-defined five-year analysis[100]. A major limitation of neratinib is its gastrointestinal toxicity, particularly diarrhea. cutaneous adverse events may also occur, which are generally believed to be caused by its broad inhibition of HER-family kinases. It can inhibit EGFR in normal intestinal epithelium, thereby interfering with epithelial renewal, barrier integrity and ion-transport regulation. In the original ExteNET study, in which routine antidiarrheal prophylaxis was not mandated, grade 3 diarrhea occurred in approximately 40% of neratinib-treated patients[101,102]. The subsequent CONTROL study demonstrated that proactive prophylactic antidiarrheal treatment and stepwise dose-escalation strategies can reduce the incidence and severity of neratinib-associated diarrhea and improve treatment tolerability[103].

Tucatinib is a later-generation, orally administered TKI with substantially greater selectivity for HER2 than for wild-type EGFR. Preclinical studies demonstrated that tucatinib reduces receptor phosphorylation and downstream signaling by preferentially inhibiting the ATP-dependent kinase activity of HER2, while relatively preserving EGFR-mediated physiological functions. This selectivity reduces EGFR-inhibition-related adverse effects compared with pan-HER inhibitors[104,105]. The clinical efficacy of tucatinib was established in the randomized phase III HER2CLIMB trial, which enrolled previously treated patients with HER2-positive unresectable locally advanced or metastatic breast cancer. The addition of tucatinib significantly improved both progression-free survival and overall survival compared with the placebo-containing regimen, establishing tucatinib as an effective treatment option in heavily pretreated HER2-positive metastatic breast cancer[106,107]. An important feature of HER2CLIMB was the inclusion of patients with brain metastases, including patients with active, untreated or progressing intracranial disease. In this subgroup, tucatinib improved central nervous system progression-free survival and reduced the risk of intracranial progression or death, demonstrating clinically meaningful activity against HER2-positive disease involving the central nervous system[108]. On the basis of the HER2CLIMB results, the US Food and Drug Administration approved tucatinib in 2020 in combination with trastuzumab and capecitabine for adults with advanced unresectable or metastatic HER2-positive breast cancer, including patients with brain metastases, who had received at least one prior anti-HER2-based regimen in the metastatic setting[109].

More recently, HER2-directed TKI development has expanded beyond ErbB2-overexpressing breast cancer to ErbB2-mutant solid tumors, especially non-small-cell lung cancer (NSCLC). Zongertinib (BI 1810631) is an orally administered, irreversible and

HER2-selective covalent TKI designed to inhibit oncogenic HER2 while largely preserving wild-type EGFR signaling. Zongertinib forms a covalent interaction with Cys805 within the HER2 kinase domain, resulting in sustained inhibition of HER2 phosphorylation and downstream signaling [110][110]. In preclinical studies, zongertinib potently inhibited tumor models driven by several forms of HER2 alteration, including NSCLC xenograft models with acquired resistance to trastuzumab deruxtecan. Furthermore, preclinical combination experiments showed that zongertinib could enhance the antitumor activity of HER2-directed ADCs and $KRAS^{G12C}$ inhibitors without producing evident additive toxicity, suggesting its potential for combination therapy strategies[110]. The Beamion LUNG-1 clinical trial evaluated the efficacy of zongertinib in patients with advanced or metastatic solid tumors carrying HER2 alterations. In the dose-escalation study, zongertinib demonstrated preliminary antitumor activity against HER2-altered tumors. Although treatment-related adverse events occurred, only 10% of patients experienced grade 3 or higher treatment-related adverse events, which were consistent with clinically relevant HER2 inhibition accompanied by reduced, but not absent, EGFR-associated toxicity[111]. Beamion LUNG-1 also demonstrated clinically meaningful activity in previously treated patients with advanced HER2-mutant non-squamous NSCLC, including patients who had previously received a HER2-targeted ADC therapy, supporting the use of zongertinib after earlier treatment[112]. In August 2025, the FDA granted accelerated approval to zongertinib for adults with unresectable or metastatic non-squamous NSCLC harboring an FDA-test-confirmed HER2 tyrosine kinase domain activating mutation after prior systemic therapy. In the approval population, the objective response rate was 75% among patients who had received platinum-based chemotherapy but no previous HER2-directed TKI or ADC, and 44% among patients previously treated with both platinum chemotherapy and a HER2-directed ADC[113]. First-line results reported subsequently showed sustained activity in previously untreated advanced HER2-mutant NSCLC[114]. On February 2026, the FDA expanded the accelerated approval to patients with the same molecularly defined disease who had not received systemic therapy for advanced disease[115].

1.2 Ionic liquids

1.2.1 Concept and fundamental physicochemical properties of ionic liquids

Ionic liquids (ILs) are salts composed entirely of cations and anions and are conventionally defined as having melting points below 100 °C[116]. Most ILs contain at least one organic ion, while the counterion may be either organic or inorganic. Unlike conventional electrolyte solutions, a pure IL contains no separate molecular solvent phase. Instead, its constituent ions form a continuous liquid medium. The low melting points of ILs arise primarily from inefficient crystal packing associated with bulky, asymmetric ions, delocalized charge distributions, conformational flexibility, and weakly coordinating counterions. These structural characteristics hinder efficient lattice packing, reduce the enthalpic stabilization of the solid state and increase conformational disorder, thereby making it difficult to form a tightly ordered lattice structure[117-121]. Common IL cations include imidazolium, pyridinium, pyrrolidinium, ammonium, phosphonium, and cholinium ions, and commonly used anions include halides, tetrafluoroborate, hexafluorophosphate, dicyanamide, alkyl sulfates, carboxylates, and bis(trifluoromethanesulfonyl)imide[119]. ILs may also be classified as aprotic ILs which usually contain quaternized cations without easily transferable protons, or protic ILs which are commonly generated by proton transfer from a Brønsted acid to a Brønsted base[122,123].

A major feature of ILs is their extensive structural tunability. Variation of the cation, anion, alkyl-chain length, charge distribution, functional groups, and hydrogen-bonding capacity can modify properties such as melting behavior, viscosity, density, miscibility, polarity, interfacial activity, chemical reactivity, and biological effects. This structural diversity gives ILs a generally

greater tunability than conventional molecular solvents, and ILs are often therefore described as "custom solvents". However, these properties are usually not independent, and structural modification intended to optimize one characteristic may simultaneously alter several other physicochemical properties[124-126].

Many ILs exhibit relatively high viscosities and, in many cases, higher densities than conventional low molecular weight organic solvents[127-130]. Density is determined by the relationship between the total molar mass of the ion pair and the effective molar volume occupied by the ions. Viscosity reflects a combination of electrostatic interactions, hydrogen bonding, dispersion forces, ion association, and conformational dynamics. In amphiphilic ILs containing sufficiently long hydrocarbon substituents, segregation between polar ionic regions and nonpolar domains can generate nanoscale structural heterogeneity, which influences diffusion, solvation, ionic transport, self-assembly, and interfacial behavior[131-133]. ILs also provide highly diverse solvation environments because they can participate in multiple types of noncovalent interactions and can therefore dissolve or stabilize a wide range of inorganic, organic, polymeric, and biological solutes[134,135]. The empirical Kamlet-Taft solvatochromic parameters are often used to describe three complementary solvent behaviors of IL: acidity (α) which is mainly influenced by the cation, hydrogen-bond-acceptor basicity (β) which is controlled mainly but not entirely by the anion, and dipolarity/polarizability (π*) which reflects contributions from both ions and from the collective polarizability of the liquid environment[136-138]. Changes in the constituent ions can consequently alter solvent-solute interactions, extraction behavior, and the solubility of specific compounds.

Another characteristic of many ILs is their extremely low equilibrium vapor pressure under ambient conditions, which reduces evaporative losses and exposure compared with conventional organic solvents[139]. However, ILs are not completely nonvolatile, some ILs can be distilled under low pressure, while others may undergo substantial chemical decomposition before significant vaporization occurs[139-141]. Because ILs consist entirely of mobile ions, ILs also exhibit intrinsic ionic conductivity, although conductivity depends not only on ion concentration but also on viscosity, ion size and shape, ion association, structural relaxation, self-diffusion, and the extent to which cation and anion movement are associated[128-130,142-144]. Notably, their physicochemical properties are particularly sensitive to water content, as most ILs are hygroscopic: absorbed water can weaken cation-anion interactions, disrupt or reorganize hydrogen-bond networks, reduce viscosity, and increase ionic mobility and conductivity. Furthermore, as the water concentration increases, the IL-dominated liquid can transform into an aqueous electrolyte solution[145,146].

1.2.2 Surface-active ionic liquids: molecular design, interfacial activity and self-assembly

Surface-active ionic liquids (SAILs) constitute a subclass of ionic liquids whose molecular architecture combines a charged or strongly hydrated ionic region with one or more hydrophobic regions, typically composed of long alkyl chains or other nonpolar substituents. This amphiphilicity enables SAILs to adsorb at interfaces and undergo concentration-dependent self-assembly in aqueous solutions. Amphiphilicity can be introduced by the cation, the anion, or both. Systems in which both constituent ions contain substantial hydrophobic regions are commonly called biamphiphilic ionic liquids (BAILs). In such systems, electrostatic association between oppositely charged amphiphilic ions, together with synergistic hydrophobic interactions between their nonpolar regions, can generate an effective molecular geometry that promotes significant self-assembly[147,148].

The hydrophobic structure is one of the main factors determining SAIL aggregation. Before substantial aggregation occurs in the bulk phase, SAIL molecules preferentially adsorb at interfaces. At air-water or oil-water interface, the hydrophobic regions minimize its contact with water, while the ionic headgroups remain preferentially hydrated, thus reducing the interfacial free energy. Consequently, increasing SAIL concentration usually leads to a progressive decrease in

surface tension until the interface approaches saturation[149,150]. Further addition of amphiphilic molecules favors association in the bulk phase, thereby reducing the unfavorable free energy contribution associated with hydration of the nonpolar regions[149,151]. When experiments confirm that the resulting aggregates are micelles, the concentration associated with the initiation of micellization is conventionally referred to as the critical micelle concentration (CMC)[153]. For amphiphilic ionic liquids capable of forming non-micellar structures, the more general term critical aggregation concentration (CAC) is more preferable because it does not presuppose the morphology of the aggregates. In vesicle-forming systems, the transition associated with the appearance of vesicular assemblies has sometimes been described as the critical vesicle concentration (CVC). The relationship between molecular geometry and aggregate morphology can be qualitatively described using the critical packing parameter (CPP). Relatively small CPP values favor the formation of highly curved micellar structures, while increasing the hydrophobic volume and/or decreasing the effective headgroup area reduces spontaneous curvature and can favor the formation of cylindrical aggregates, bilayers, and vesicles[152]. However, the CPP should be regarded as a qualitative geometric framework rather than a strict criterion, because ion association, hydration, molecular interdigitation, chain conformation and solution composition can dynamically alter the effective molecular packing[152]. Thus, SAIL self-assembly has been reported to generate a variety of structures, including spherical, ellipsoidal, cylindrical, and worm-like micelles, bilayers, unilamellar and multilamellar vesicles, as well as lamellar and other ordered phases[147,154,155].

Increasing alkyl-chain length generally enhances the hydrophobic driving force for association and decreases the concentration required for self-assembly. Singh et al. synthesized ester-functionalized nicotine-derived SAILs, [C_nENic][Br] (n = 8, 10, and 12), all of which exhibited concentration-dependent self-assembly behavior in water, with the CMC decreasing with increasing alkyl-chain length[156]. A similar dependence was observed by Jiao et al. for 1-alkyl-3-methylimidazolim alkyl sulfates ([$C_n$mim][C_mSO_4]) SAILs, in which increasing the alkyl-chain length of either ionic component promoted aggregation[157]. Rao et al. also demonstrated that variation of the hydrophobic-chain lengths of both ions in biamphiphilic imidazolium alkyl sulfate ILs significantly affected their surface activity and self-assembly behavior in aqueous solution[158]. However, hydrophobic-chain length alone does not determine aggregation behavior. Headgroup hydration, charge density and delocalization, functional group chemistry, linker structure, steric constraints, and conformational flexibility can all influence the balance between hydration and hydrophobic association[147,148].

Although the removal of hydrophobic regions from direct contact with water is a major thermodynamic driving force for aggregation, counterion association also plays an important role. Counterion identity can influence interfacial adsorption, CAC, aggregate size and morphology through differences in charge density, hydration, molecular size, polarizability, hydrophobicity, and specific interactions with the ionic headgroups[159]. The counterion effect is particularly pronounced in alkyl sulfate-based SAILs. Jiao et al. demonstrated that replacement of Na^+ in sodium dodecyl sulfate (SDS) with organic imidazolium or pyrrolidinium counterions generated SAILs with lower CMC and higher surface activity than SDS[160]. Studies of SAILs containing quaternary ammonium counterions have also shown that counterion structure can significantly affect aggregation behavior and aggregate size in aqueous solutions[161]. Therefore, replacing a small inorganic counterion with an organic amphiphilic ion is a strategy to transform traditional ionic surfactants into an amphiphilic system with enhanced surface activity and stronger association between the constituent ions.

External electrolytes provide another way to regulate SAIL self-assembly. The added electrolytes can shield electrostatic repulsion between charged headgroups, enhance counterion association, and generally reduce the concentration required for aggregation. However, depending on ion identity and molecular architecture, this effect may not be limited to a simple change in CAC, but may also induce significant reorganization of the supramolecular structure. Rao et al. showed that dodecylbenzenesulfonate-based SAILs formed micellar aggregates in water but underwent a NaBr-induced micelle-to-vesicle transition[162]. Conversely, studies by Sun et al. on acyl amino acid surfactants demonstrated that increasing ionic strength or introducing specific counterions, like tetraalkylammonium ions, could promote a vesicle-to-micelle transition, illustrating the importance of ion-specific effects on headgroup hydration and interfacial packing[163]. These observations suggest that electrolyte effects depend not only on ionic strength but also on the chemical properties and interfacial affinity of the ions involved.

Temperature is also an important variable affecting the interfacial activity and self-assembly of SAILs. It can influence not only the CAC but also aggregate dimensions and morphology, and the direction of these changes is highly system-dependent. Roy et al. demonstrated a reversible temperature-induced vesicle-to-micelle transition in assemblies containing the SAIL 1-hexadecyl-3-methylimidazolium chloride (C_{16}mimCl) and 5-methyl salicylic acid (5mS)[164]. Similarly, a catanionic system composed of cetyltrimethylammonium bromide (CTAB) and 1-butyl-3-methylimidazoliumdodecyl sulfate ([bmim][DS]) exhibited temperature- and composition-dependent transitions among vesicular, cylindrical, and spherical micellar structures[165]. These findings emphasize that aggregate morphology determined under specific experimental conditions cannot necessarily be generalized to a different temperature, ionic environment, or solvent composition.

Overall, SAILs are highly tunable and their interfacial adsorption and supramolecular organization can be modulated through the size and structure of the hydrophobic domains, the chemical properties of the ionic headgroups, counterion identity, ionic environment, and temperature. Their significant surface activity and capacity for self-assembly enable SAILs not only to solubilize hydrophobic compounds but also to form nanoscale assemblies that can load payloads and interact with biomembranes. These physicochemical characteristics lay the foundation for the biomedical and therapeutic applications of SAILs.

1.2.3 Biomedical and therapeutic applications of surface-active ionic liquids

Surface-active ionic liquids (SAILs) have attracted increasing attention as multifunctional components in pharmaceutical and biomedical formulations due to their interfacial activity and self-assembly behavior. Depending on their molecular structure and concentration, SAILs can function as solubilizers, permeability modifiers, self-assembling nanocarriers, or bioactive amphiphilic molecules. Their ionic composition can be modified to tune hydrophobicity, surface charge, aggregation behavior, and interactions with drugs and biomembranes, thereby enabling the formulation and delivery of compounds with poor aqueous solubility or limited membrane permeability[134,135,166].

Poorly water-soluble molecules can partition into the nonpolar domains of SAIL aggregates, while charged or polar compounds can interact with ionic headgroups through electrostatic interactions, hydrogen bonding, and other non-covalent interactions. Therefore, self-assembly can provide hydrophobic region for cargo incorporation while maintaining a hydrated ionic interface with the surrounding aqueous medium. Pal et al. investigated the interactions between lidocaine hydrochloride with the SAILs 1-dodecyl-3-methylimidazolium chloride ([C_{12}mim][Cl]), and 1-tetradecyl-3-methylimidazolium chloride (C_{14}mim][Cl]). Addition of the drug decreased the

critical aggregation concentration and generated significant interactions with the interfacial region of the SAILs aggregates, supporting their potential use as drug-carriers[167]. Kulshrestha et al. reported a magnetic proline-derived SAIL ([$ProC_{10}$][$FeCl_3Br$]) which can self-assemble into vesicles in water. These vesicles were able to incorporate the model hydrophobic molecule pyrene and the antibiotic ciprofloxacin and subsequently release the incorporated compounds in a controlled manner[168].

Amphiphilic ionic liquids can interact with biological barriers and alter the organization of membrane lipids and associated biomolecules. Therefore, they may influence drug transport across biological barriers rather than simply functioning as solubilizers. This property has been extensively investigated for transdermal drug delivery[135,166]. Tahara et al. employed choline-fatty acid ionic liquids to facilitate the incorporation of an antigenic peptide into an oil-based permeation-enhancing formulation. The optimized system significantly increased transdermal peptide transport compared to an aqueous carrier and induced antitumor vaccination response with no detectable skin irritation under the tested conditions[169]. Uddin et al. developed lipid-based biocompatible ionic-liquid nanodispersions for the the peptide drug leuprolide acetate and reported improvements in formulation stability, drug loading, and transdermal transport. The optimized formulation produced a significant increase in peptide transport compared with the corresponding aqueous carriers[170].

However, the molecular properties that promote membrane association and enhanced delivery may also contribute to biological toxicity. Therefore, cytotoxicity is one of the major limitations in the biomedical development of SAILs. Biological responses to ILs depend on cation and anion structure, alkyl-chain length and concentration, aggregation state, exposure time, and cell type[135,166]. The charged region of an amphiphilic IL can interact with polar or charged membrane components, while its hydrophobic domain can partition into the lipid acyl-chain region. Increasing hydrophobicity generally enhances membrane partitioning and may alter lipid packing, membrane fluidity and membrane permeability. Kumar et al. reported IC_{50} values spanning several orders of magnitude across structurally different ILs on MCF-7 human breast cancer cells, demonstrating that the structures of both cations and anions have a substantial contribution, particularly for cations containing long alkyl substituents[171]. Cook et al. further found that within a homologous series of alkylimidazolium ILs, increasing hydrophobicity was associated with stronger partitioning and permeabilization of model phospholipid membranes, which was associated with toxicity to bacterial, yeast, and mammalian cells[172]. High membrane activity is not necessarily harmful in all biomedical contexts. Strong membrane interactions may contribute positively to antimicrobial activity or permeability, whereas the same properties may be undesirable for carriers intended to deliver selective therapeutic agents. Therefore, SAIL design must find a balance between sufficient amphiphilicity to support stable self-assembly, cargo incorporation, and membrane associated perturbation and toxicity. Aggregation state is also crucial because free SAIL molecules and pre-formed micellar or vesicular aggregates may not interact with biomembranes in the same manner. Therefore, biological effects should be interpreted by combining both absolute concentration and associated aggregation state.

Hemolysis provides a complementary measure of membrane compatibility of amphiphilic compounds because erythrocytes are particularly sensitive to surfactant-induced membrane damage. Therefore, hemoglobin release could serve as a functional indicator of membrane-disruptive activity. Just like cytotoxicity, hemolytic activity is also strongly dependent on hydrophobic structures. García et al. investigated a homologous series of cholinium-based ILs, $C_nCholBr$ (n = 10, 12, 14, and 16), and observed a pronounced increase in hemolytic activity with

increasing hydrocarbon chain length. The concentrations required to induce 50% hemolysis of red blood cells (HC_{50}) were 420 ± 2 μg mL^{-1} for C_{12}, 34 ± 0.2 μg mL^{-1} for C_{14}, and 11 ± 0.1 μg mL^{-1} for C_{16}[173]. These results demonstrate that relatively modest structural changes within a homologous series can substantially alter erythrocyte compatibility. A similar chain-length dependent HC_{50} was observed for ester-functionalized cholinium-based ILs, C_nECholBr (n = 10, 12, and 14), for which HC_{50} values of >2500 μM, 232 ± 2 μM, and 56 ± 1 μM were reported for the C_{10}, C_{12}, and C_{14} homologues, respectively[174]. Although the HC_{50} values in two studies reported in different units, both homologous series clearly showed a trend of increasing hemolytic activity with increasing hydrophobicity.

Biodegradability is another important consideration in the development of SAILs for biomedical and pharmaceutical applications. Earlier studies have demonstrated that several conventional ionic-liquid structures, including some imidazolium-based compounds, exhibit limited susceptibility to biodegradation[175,176]. Therefore, the incorporation of biologically derived building blocks, including choline, amino acids, and fatty acid-derived ions, has been explored as a strategy for developing more environmentally friendly ILs. For example, lauroyl sarcosinate-based SAILs containing biologically relevant cations exhibited substantial biodegradation, and some morpholinium- and piperidinium-containing compounds undergoing extensive or complete biodegradation under the investigated conditions[177,178]. However, biological origin alone does not guarantee complete biodegradability. Their biodegradability must be assessed based on the complete ionic structure. Several structural characteristics have been shown to be associated with improved biodegradability. Accessible, unbranched aliphatic structures and the introduction of hydrolysable or oxidizable functional groups, such as hydroxyl, carbonyl, carboxyl, ester, and, in suitable molecular environments, amide groups, may facilitate microbial transformation. Conversely, extensive branching, quaternary carbon centers, halogenation, and certain chemically persistent heterocyclic structures may hinder biodegradation[178,179]. These relationships should be regarded as general molecular-design tendencies rather than deterministic rules because the final biodegradation depends on the complete molecular structure, bioavailability to microorganisms, and toxicity toward the microbial populations responsible for degradation. For SAILs, increasing the length of a metabolically accessible linear alkyl chain does not necessarily improve their biodegradability. García et al. evaluated the aerobic biodegradation of C_nCholBr (n = 10, 12, 14, and 16) using the OECD 310 CO_2 headspace test. After 28 days, biodegradation values of 78 ± 5.7%, 69 ± 1.8%, 52 ± 4.9%, and 0% were obtained for the C_{10}, C_{12}, C_{14}, and C_{16} homologues, respectively[173]. Importantly, the C_{16} homologue caused approximately 85% inhibition of the microbial inoculum in the associated inhibition assay. Therefore, the extremely low biodegradation under these conditions was attributed mainly to its strong antimicrobial activity toward the microorganisms responsible for mineralization rather than to an intrinsically non-metabolizable hydrocarbon chain. This example demonstrates that experimentally measured biodegradation reflects not only structural susceptibility to metabolism but also bioavailability and toxicity to the degrading microbial community.

One strategy to improve degradation behavior while maintaining surface activity is to introduce functional groups that are unstable to hydrolysis or enzymatic degradation. Ester-bond is particularly attractive because its cleavage can break down a long-chain amphiphile into smaller products that may subsequently be more suitable for microbial metabolism. García et al. evaluated ester-functionalized cholinium-based SAILs, C_nECholBr (n = 10, 12, and 14), using the OECD 310 CO_2 headspace test and found that all three compounds reached more than 60%

biodegradation after 28 days[174]. Compared with the corresponding non-ester-functionalized cholinium-based SAILs investigated previously, the ester-containing SAILs exhibited superior degradation kinetics, supporting introduction of a cleavable ester-bond as a useful molecular-design strategy for enhancing biodegradability while retaining amphiphilic functionality.

Interaction with proteins is another important factor determining the behavior of SAIL in biological media. Protein-SAIL association may involve electrostatic attraction or repulsion, hydrophobic interactions, hydrogen bonding, counterion-mediated effects, and interactions with pre-existing micellar or vesicular aggregates. Therefore, the resulting response is strongly dependent on SAIL structure, concentration, aggregation state, protein identity, pH, and solvent environment. Paul et al. investigated human serum albumin (HSA) in the presence of submicellar concentrations of 1-butyl-3-methylimidazolium octylsulfate ([BMIM][OS]) and observed spectroscopic changes consistent with partial perturbation of the native protein conformation[180]. This finding demonstrates that significant interactions with serum proteins may occur even below the aggregation concentration of a SAIL. However, aggregation does not necessarily result in protein destabilization. Bharmoria et al. investigated the vesicle-forming SAIL, 3-Methyl-1-octylimidazolium dodecylsulfate ([C_8mim][$C_{12}OSO_3$]), and confirmed that its interaction with bovine serum albumin (BSA) is concentration-dependent. The protein-SAIL interactions observed in the low-concentration differed substantially from those observed at and above the vesicular forming concentration, while BSA remained comparatively stable in the vesicular and post-vesicular states[154]. Alves et al. also reported that aggregates formed by the fluorinated SAILs cholinium perfluorobutanesulfonate [$N_{1112(OH)}$][$C_4F_9SO_3$], and 1-ethyl-3-methylimidazolium perfluorobutanesulfonate [C_2C_1Im][$C_4F_9SO_3$], could stabilize BSA and promote a more compact protein conformation under the investigated conditions[181]. These findings demonstrate that the outcome of protein-SAIL interactions depends strongly on molecular structure and aggregation state.

Recent studies have further highlighted the importance of aggregate surface charge in SAIL vesicle-protein interactions. Sardar et al. compared cationic-rich and anionic-rich vesicles formed from the long-chain SAIL 1-hexadecyl-3-methylimidazolium chloride (C_{16}MimCl) and aerosol OT in their interactions with human serum albumin (HSA). The tertiary structure of HSA was largely preserved in the presence of cationic-rich vesicles but was significantly perturbed by anionic-rich vesicles. After HSA adsorption, the size of cationic-rich vesicles increased significantly, while the anionic-rich vesicles underwent structural disruption and generated smaller vesicular structures. Zeta-potential measurements indicated that electrostatic attraction played a dominant role in protein adsorption to the cationic-rich vesicles, whereas electrostatic repulsion led to destabilization of the anionic-rich assemblies[182]. These observations suggest that the effective surface charge and ionic composition of SAIL aggregates can strongly affect protein conformation and vesicle stability. However, it should be recognized that most mechanistic studies on protein-SAIL interaction were conducted using purified HSA or BSA in relatively simple aqueous media. Complete serum contains a complex mixture of albumin, immunoglobulins, apolipoproteins, complement components, enzymes, electrolytes, and other biomolecules that can compete for association with the surface of a SAIL aggregate. Therefore, protein interactions observed in simplified buffer systems cannot be directly interpreted as evidence of compatibility or colloidal stability in serum-containing biological media.

Overall, the structural versatility of SAILs provides opportunities for drug solubilization, self-assembled nanocarrier formation, permeability enhancement, antimicrobial activity, and

delivery of peptide or protein therapeutics. At the same time, their amphiphilic and surface-active nature introduces potential limitations, including nonspecific membrane disruption, hemolysis, variable biodegradability, protein binding, and altered colloidal behavior in complex biological media. In addition, the in vivo distribution, metabolism, clearance, immunological effects, and long-term toxicity of many SAILs remain insufficiently characterized. Moreover, development of SAIL-based pharmaceutical formulations requires rigorous control of chemical purity, residual synthetic reagents, aggregate size distribution, batch-to-batch reproducibility, and formulation stability. Consequently, most biomedical applications of SAIL-based formulations remain in the preclinical stage, including physicochemical characterization, cell-based studies, and tests on animal models.

2. Aim of the project

Human epidermal growth factor receptor 2 (HER2/ErbB2) plays a crucial role in the development and progression of HER2-positive cancers through receptor dimerization and activation of downstream signaling pathways, including the PI3K/Akt and MAPK/ERK cascades. Clinically established HER2-targeted therapies mainly target on the extracellular domain (ECD) or the intracellular kinase domain (TKD) of the receptor, while research on the TMD as a therapeutic target is comparatively underexplored, although recent studies have shown that the TMD also plays an important role in receptor dimerization.

Based on the functional importance of the HER2 transmembrane domain, three HER2-TMD-derived peptide variants (v1, 2 and 3) were designed as potential competitive inhibitors of receptor dimerization. Our hypothesis was that incorporation of a HER2-TMD-derived peptide into the cell membrane could interfere with native transmembrane-domain packing and receptor dimerization, thereby inhibiting the activation of HER2-associated intracellular signaling pathways. However, the hydrophobicity of transmembrane peptides generates substantial challenges during synthesis, purification, physicochemical characterization, and delivery in biological environments. The peptide constructs were therefore chemically modified to improve their aqueous dispersibility, while bi-amphiphilic surface-active ionic liquid (BAIL) vesicles were investigated as nanocarriers for incorporation and delivery of the hydrophobic peptide to cancer cells. The overall aims of this project are:

1) Synthesize nicotinium-based bi-amphiphilic surface-active ionic liquid (Nic BAIL); Characterize Nic BAIL using appropriate analytical techniques to confirm its chemical identity and relevant physicochemical properties.

2) Purify three hydrophobic HER2-TM-derived peptide variants using suitable chromatographic methods and confirm their molecular identities by mass spectrometry.

3) Generate the Nic BAIL-v3 nanoformulation and evaluate its physicochemical properties, including vesicle formation, peptide incorporation, size distribution, morphology and colloidal stability.

4) Investigate the interaction of the Nic BAIL-v3 nanoformulation with artificial lipid membrane model by planar bilayer electrophysiology.

5) Evaluate the biological activity of the Nic BAIL-v3 nanoformulation on cell lines with different HER2/ErbB2 status.

3. Results and discussion

3.1 Synthesis and characterization of nicotinium-based bi-amphiphilic surface-active ionic liquid (Nic BAIL)

A nicotinium-based bi-amphiphilic surface-active ionic liquid (Nic BAIL) was synthesized via a two-step route. In the first step, the nicotinium-based mono-amphiphilic ionic liquid (Nic MAIL) was prepared. This synthesis involved (i) Fischer esterification of bromoacetic acid with dodecan-1-ol to afford dodecyl 2-bromoacetate, followed by (ii) Menshutkin quaternization of nicotine at the pyridine nitrogen with the bromoacetate intermediate to yield Nic MAIL.

Under solvent-free conditions, dodecan-1-ol was esterified with bromoacetic acid in the presence of *p*-toluenesulfonic acid (PTSA) as catalyst to form dodecyl 2-bromoacetate. The progress of the reaction was monitored by thin layer chromatography (TLC). After purification, dodecyl 2-bromoacetate was isolated in 82% yield. Subsequent quaternization of the pyridine nitrogen of nicotine with dodecyl 2-bromoacetate proceeded via nucleophilic substitution to give Nic MAIL in 65% yield after purification (Figure S1).

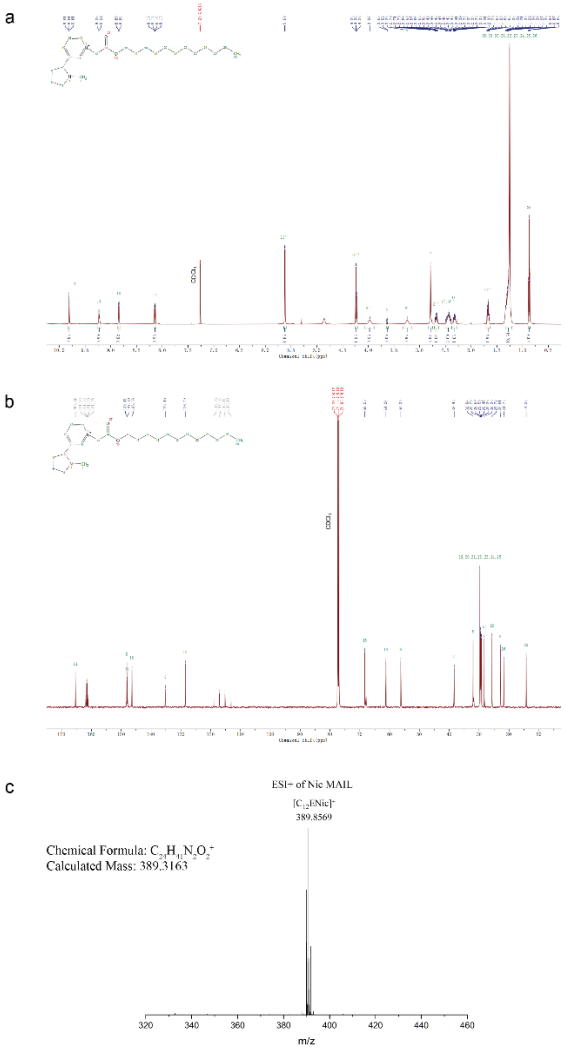


Figure 3. 1H NMR (600 MHz, $CDCl_3$) spectrum of Nic MAIL (a): δ 9.81 (s, 1H), 9.23 (d, *J* = 8.2 Hz, 1H), 8.85 (d, *J* = 6.3 Hz, 1H), 8.14 (dd, *J* = 8.2, 6.1 Hz, 1H), 5.62 (s, 2H), 4.24 (t, *J* = 6.9 Hz, 2H), 3.97 (s, 1H), 3.63 (t, *J* = 6.7 Hz, 1H), 3.25 (s, 1H), 2.79 (s, 3H), 2.72–2.63 (m, 1H), 2.51–2.37 (m, 1H), 2.36–2.28 (m, 1H), 1.71–1.64 (m, 2H), 1.34–1.25 (m, 36H), 0.87 (t, *J* = 7.0 Hz, 3H); 13C NMR (151 MHz, $CDCl_3$) spectrum of Nic MAIL (b): δ 165.27, 148.11, 147.89, 146.35, 135.16, 128.49, 68.26, 61.24, 56.30, 38.45, 32.04, 29.75, 29.69, 29.56, 29.47, 29.26, 28.35, 25.72, 22.81, 21.75, 14.23; Nic MAIL under ESI+ mode (c).

The successful formation of Nic MAIL was confirmed by NMR and mass spectrometry. In the 1H NMR spectrum (Figure 3a), quaternization of the pyridine nitrogen caused pronounced downfield shifts of the aromatic protons relative to nicotine, with the aromatic resonances appearing in the δ 8.00-10.00 ppm region. This characteristic deshielding is consistent with formation of a pyridinium-type cation, in which the positive charge on nitrogen withdraws electron density from the aromatic ring. In addition, the signal at δ 0.87 ppm was assigned to the terminal methyl group of the alkyl chain, the signal at δ 1.25 ppm to the methylene envelope of the dodecyl chain, and the singlet at δ 5.62 ppm to the methylene group directly attached to the quaternized nitrogen (-N^+-CH_2-), further supporting successful introduction of the dodecyl 2-bromoacetate moiety. In the 13C NMR spectrum (Figure 3b), the resonance at δ 61.24 ppm was assigned to the carbon of the -N^+-CH_2- group, while the ester carbonyl carbon appeared at δ 165.27 ppm. These NMR data are consistent with formation of Nic MAIL. In ESI+ mass spectrometry (Figure 3c), a main ion peak at m/z 389.8569 for the nicotinium ester cation $[C_{12}ENic]^+$ ($C_{24}H_{41}N_2O_2^+$) was observed, consistent with the expected molecular mass.

In the second step, the Nic BAIL was prepared by anion exchange of Nic MAIL with sodium dodecyl sulfate (SDS), thereby replacing bromide with dodecyl sulfate (DS^-). After purification, Nic BAIL was obtained in 47% yield.

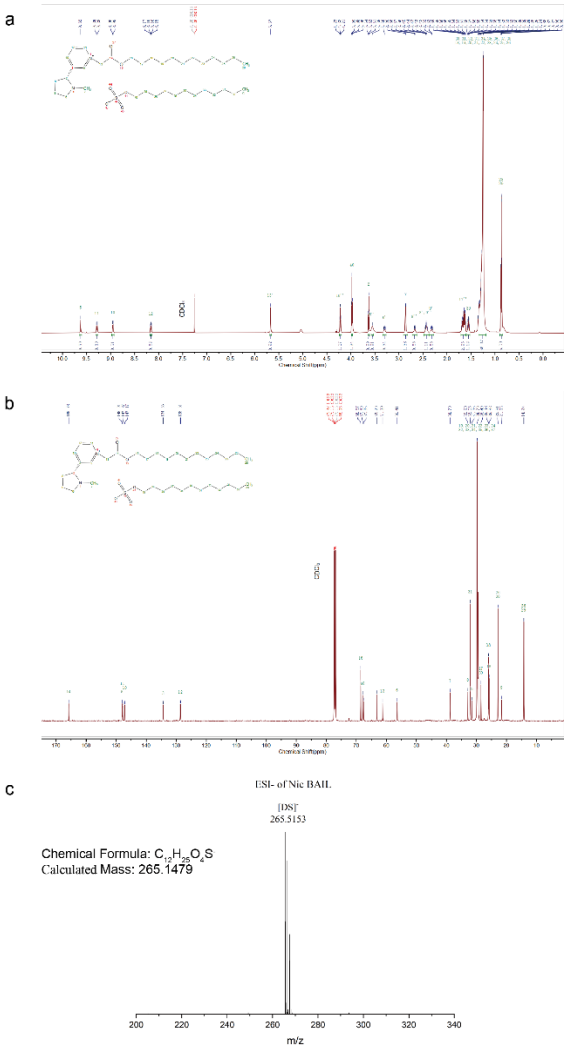


Figure 4. 1H NMR (600 MHz, $CDCl_3$) spectrum of Nic BAIL (a): δ 9.62 (s, 1H), 9.28 (d, J = 8.2 Hz, 1H), 8.95 (d, J = 6.1 Hz, 1H), 8.16 (dd, J = 8.2, 6.1 Hz, 1H), 5.67 (s, 2H), 4.22 (t, J = 7.0 Hz, 2H), 3.98 (t, J = 6.9 Hz, 4H), 3.62 (t, J = 6.7 Hz, 1H), 3.55 (s, 1H), 3.34–3.26 (m, 1H), 2.86 (s, 3H), 2.71–2.62 (m, 1H),

2.47–2.38 (m, 1H), 2.35–2.27 (m, 1H), 1.71–1.61 (m, 2H), 1.58–1.52 (m, 2H), 1.35–1.24 (m, 36H), 0.87 (dt, *J* = 6.6Hz, 6H); 13C NMR (151 MHz, $CDCl_3$) spectrum of Nic BAIL (b): δ 165.78, 148.01, 147.87, 147.17, 134.33, 128.61, 68.57, 67.89, 67.63, 63.20, 61.29, 56.41, 38.70, 32.90, 32.05, 31.53, 29.79, 28.49, 25.98, 25.82, 22.81, 21.65, 14.24; Nic BAIL under ESI- mode (c).

Conversion of Nic MAIL to Nic BAIL was supported by both NMR and mass spectrometry. Compared with the 1H NMR spectrum of Nic MAIL, the resonances in the 1H NMR spectrum of Nic BAIL (Figure 4a) at δ 0.87 and 1.25 ppm, corresponding to the terminal methyl and methylene protons of the alkyl chains, respectively, showed increased integral intensities, consistent with the introduction of an additional dodecyl chain from the dodecyl sulfate anion. Moreover, a characteristic triplet at δ 3.98 ppm was assigned to the methylene group adjacent to the sulfate headgroup in the dodecyl sulfate anion ($-CH_2-O-SO_3^-$). The aromatic multiplets in the δ 8.00-10.00 ppm region were retained, indicating preservation of the nicotinium aromatic core during the ion-exchange process. In the 13C NMR spectrum of Nic BAIL (Figure 4b), the signal at δ 67.89 ppm further supported the presence of the methylene carbon adjacent to the sulfate group. In ESI+ mass spectrometry, consistent with Nic MAIL, a main ion peak signal belonging to the nicotinium ester cation was observed, while in ESI- mode (Figure 4c), a main ion peak signal at m/z 265.5153 for dodecyl sulfate anion DS^- ($C_{12}H_{25}SO_4^-$) was observed, consistent with the expected molecular mass. Together, these data support the presence of the nicotinium cation and dodecyl sulfate anion, supporting successful anion exchange.

3.2 Purification and characterization of ErbB2-TM peptides

Three peptide derivatives (Table 1) were designed and synthesized based on the amino acid sequence corresponding to residues 653-675 of the human HER2 transmembrane (TM) domain, SIISAVVGILLVVVLGVVFGILI. The native TM part is 23 amino acids long with and is dominated by highly hydrophobic residues like Ile, Leu, and Val. Its highly hydrophobicity is consistent with its native function as a membrane-spanning α-helical domain, but also presents practical challenges during synthesis, purification and physicochemical characterization. Therefore, we introduced structural modifications to improve the physicochemical properties of the peptide and facilitate its subsequent experimental applications. The v1 construct (SIISAVVGILLVVVLGVVFGILI-Ado-KKKK) was designed as the non-fluorescent parent peptide. In this construct, Ado (8-amino-3,6-dioxaoctanoic acid) serves as a short miniPEG spacer connecting the hydrophobic TM part to a C-terminal poly-lysine tag (KKKK). The hydrophilic poly-lysine tag was introduced to improve the solubility in aqueous solution. To enable fluorescence-based detection and visualization in subsequent cellular uptake studies, 5(6)-carboxyfluorescein (FAM) was conjugated to the N-terminus of v1 to generate v2 (FAM-SIISAVVGILLVVVLGVVFGILI-Ado-KKKK). FAM is a widely used fluorophore with strong visible light absorption and fluorescence, exhibiting a distinct absorption band around 490 nm under near-neutral aqueous conditions. In v3, an additional PEG4 linker was introduced between FAM and the TM sequence (FAM-PEG4-SIISAVVGILLVVVLGVVFGILI-Ado-KKKK) to increase the spatial separation between the fluorophore and the core TM sequence, thereby minimizing potential steric and physicochemical perturbations associated with direct attachment of FAM to the TM sequence. Furthermore, the PEG4 linker could additionally enhance the hydrophilicity of the construct and was expected to reduces the tendency of aggregation and facilitate solubility and stability.

Crude ErbB2-TM derivative peptides (v1-v3) were purified by preparative HPLC on an ISAspher 100-5 Si (RP) column (250 × 20 mm) under HILIC conditions using H_2O/ACN

containing 0.1% TFA as the mobile phase. The crude peptides were purified using a gradient from 85% to 50% ACN+0.1% TFA over 60 min. PDA detection was performed at 214 nm for all peptides to monitor peptide-bond absorbance. For the FAM-labeled peptides (v2 and v3), chromatograms were additionally monitored at 450 nm for fluorescence-selective detection (Figure S2). Although FAM exhibits a distinct absorption band at approximately 490 nm under near-neutral aqueous conditions, a stronger chromatographic response was experimentally observed at 450 nm under acidic conditions (ACN/H_2O with 0.1%TFA) used for purification. Therefore, 450 nm was chosen as the additional monitoring wavelength. The collected fractions were lyophilized to remove solvent and afford the purified peptides, with yields of v1, 54%; v2, 55%; and v3, 54%.

Analytical HPLC chromatograms of the purified peptides showed a dominant product peak accompanied only by very weak impurity peaks eluting at 4.1-4.5 min (Figure 5). The retention times (*t*R) at 214nm of the purified peptides were 5.792 min for v1, 5.777 min for v2, and 5.895 min for v3. Based on peak-area normalization, the purities of v1, v2, and v3 were estimated to be 98.14%, 97.68%, and 98.77%, respectively (Table 1). All peptides showed purities above 95%, suggesting that the preparative HPLC method removed most UV-detectable impurities under these analytical conditions.

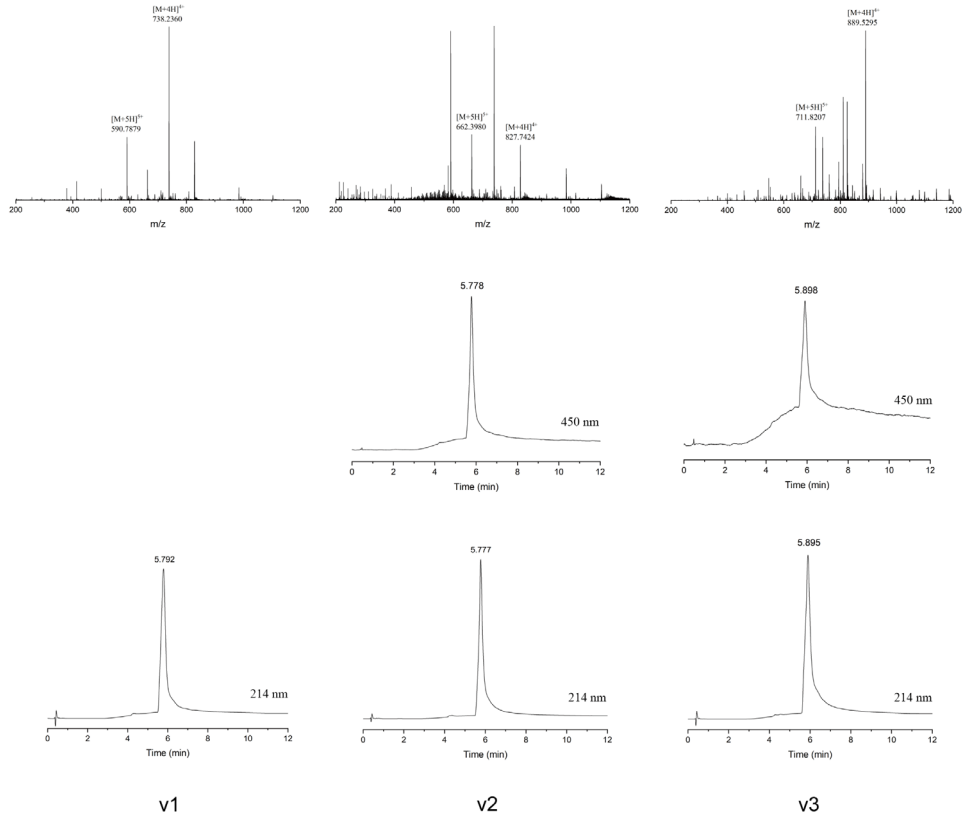


Figure 5. HPLC and LC-MS analysis of v1-v3 peptides.

Peptides	Sequences	tR (min)	Theoretical m/z	Measured m/z	Mass error (ppm)
v1	SIISAVVGILLVVVLGVVFGILI-Ado-KKKK	5.792	738.2453	738.2360	-12.6
v2	FAM-SIISAVVGILLVVVLGVVFGILI-Ado-KKKK	5.777	827.7572	827.7424	-17.9
v3	FAM-PEG4-SIISAVVGILLVVVLGVVFGILI-Ado-KKKK	5.895	889.5427	889.5295	-14.8

Table 1. Sequences and analytical characterization of v1-3 peptides. Retention time (tR) is based on 214 nm detection. The detected mass peak and calculated mass error are based on $[M+4H]^{4+}$.

After purification and lyophilization, the identities of v1-3 peptides were confirmed by LC-MS in positive electrospray ionization (ESI+) mode. The mass spectra (Figure 5) exhibited the characteristic multiply protonated ion distributions expected for these peptides. For v1, characteristic ion clusters were observed at m/z 590.7879 and 738.2360, assigned to $[M+5H]^{5+}$ and $[M+4H]^{4+}$ charge states, respectively; For v2, the $[M+5H]^{5+}$ and $[M+4H]^{4+}$ ions were detected at m/z 662.3980 and 827.7424, while v3 exhibited the corresponding ions at m/z 711.8207 and 889.5295. These signals are in close agreement with the calculated mass and are consistent with charge-state distribution of the target peptide, supporting the assignment to the target molecular species. Taken together, the chromatographic profiles and ESI-MS results confirmed the successful purification and molecular identity of v1-3 peptides.

3.3 Physicochemical characterization of Nic BAIL vesicles and Nic BAIL-v3 complexes

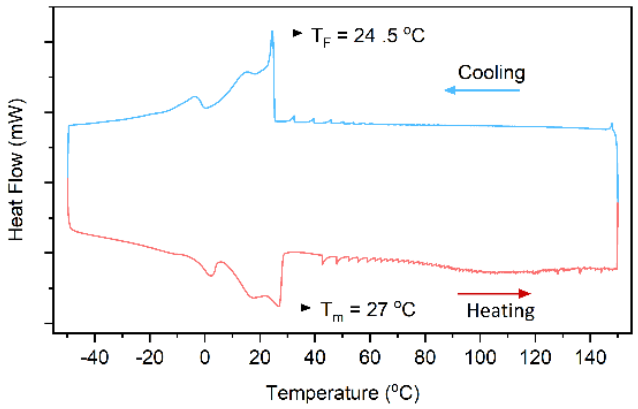


Figure 6. Differential scanning calorimetry (DSC) analysis of Nic BAIL. The figure shows the heating cycle (red), cooling cycle (blue), melting (Tm) and freezing (Tf) temperature of Nic BAIL.

The thermal behavior of Nic BAIL was investigated by differential scanning calorimetry (DSC) to define an appropriate temperature window for vesicle preparation and characterization. The thermogram (Figure 6) showed a reproducible major phase transition near room temperature, with the principal transition temperatures observed at 27.0 °C during heating and 24.5 °C during cooling. The relatively small thermal hysteresis between the heating and cooling scans indicates that this transition is largely reversible, although accompanied by a certain degree of structural rearrangement during the phase transition process. This main thermal event is consistent with an ordering-disordering transition of the amphiphilic Nic BAIL, most likely associated with rearrangement of the hydrophobic alkyl chains. In addition to the main transition, several weaker broad peaks were observed, which may reflect more subtle structural rearrangements or heterogeneity in molecular packing. Overall, the DSC results provide a physicochemical basis for performing vesicle extrusion above the transition temperature. At 37 °C, Nic BAIL was above the observed thermal transition, justifying performing extrusion of vesicles and preparation of nanoformulation at this temperature. On this basis, dynamic light scattering (DLS) and cryogenic transmission electron microscopy (Cryo-TEM) were employed to characterize the size, morphology, and stability of Nic BAIL vesicles and Nic BAIL-v3 complexes.

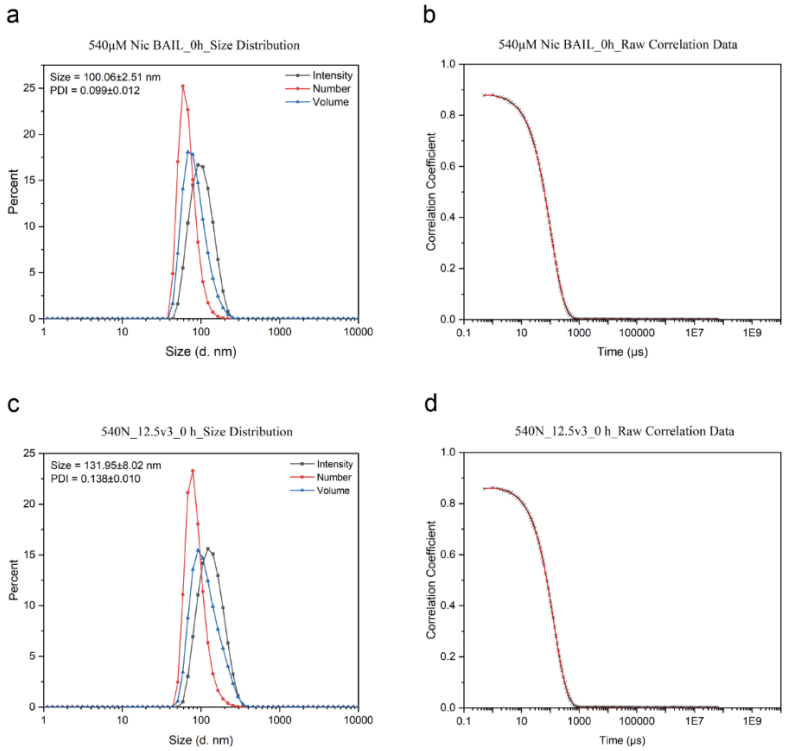


Figure 7. DLS profiles show the intensity, number and volume distribution of hydrodynamic size of freshly prepared 540 μM Nic BAIL vesicles suspension (a) and 540 μM Nic BAIL-12.5 μM v3 nanoformuulation (c) in 10 mM pH7.4 PB at 37 ℃, with corresponding correlation coefficient vs decay time diagrams (b, d). Data are presented as mean ± SD (n=3).

DLS measurements performed at 37 ℃ showed that freshly prepared Nic BAIL vesicles exhibited a unimodal nanoscale size distribution, indicating the formation of a relatively homogeneous vesicle population (Figure 7a). Upon addition of v3 peptide (12.5 μM), the intensity-, volume-, and number-weighted size distributions all shifted slightly toward larger diameters, suggesting a modest increase in hydrodynamic size after peptide addition (Figure 7c). This observation shows a change in apparent hydrodynamic size after peptide addition. Importantly, no pronounced secondary population at larger diameters was observed, suggesting that no dominant large-aggregate population was detected under these measurement conditions. The corresponding correlograms (Figure 7b and 7d) displayed high intercepts and smooth single-step decays, further supporting good quality and the absence of a dominant slowly diffusing population.

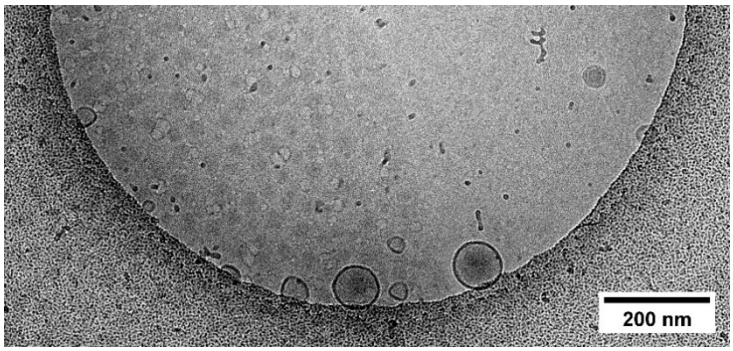


Figure 8. Cryo-TEM image of Nic BAIL vesicles at ×36000.

Subsequent cryo-TEM imaging further showed that Nic BAIL vesicles exhibited a vesicular morphology with diameters of approximately 50-100 nm (Figure 8). No marked morphological changes or obvious large-scale structural perturbations were observed after the incorporation of

v3 peptide. The absence of pronounced morphological changes may be attributed to the small molecular dimensions of v3 peptide compared with the overall vesicle size, meaning that potential peptide association or membrane insertion would not produce detectable alterations in vesicle morphology. Although the slight increase in hydrodynamic diameter observed by DLS is consistent with possible peptide-vesicle assosiation, neither this observation nor the cryo-TEM images provide direct evidence of peptide incorporation into the vesicle membrane. Furthermore, individual v3 peptides could not be resolved under the present cryo-TEM imaging conditions, preventing direct assessment of their localization. Taken together, the results demonstrate the preservation of nanoscale vesicle-like structure, but do not independently confirm peptide loading, the extent of peptide-vesicle association, or the localization of v3 within the vesicle.

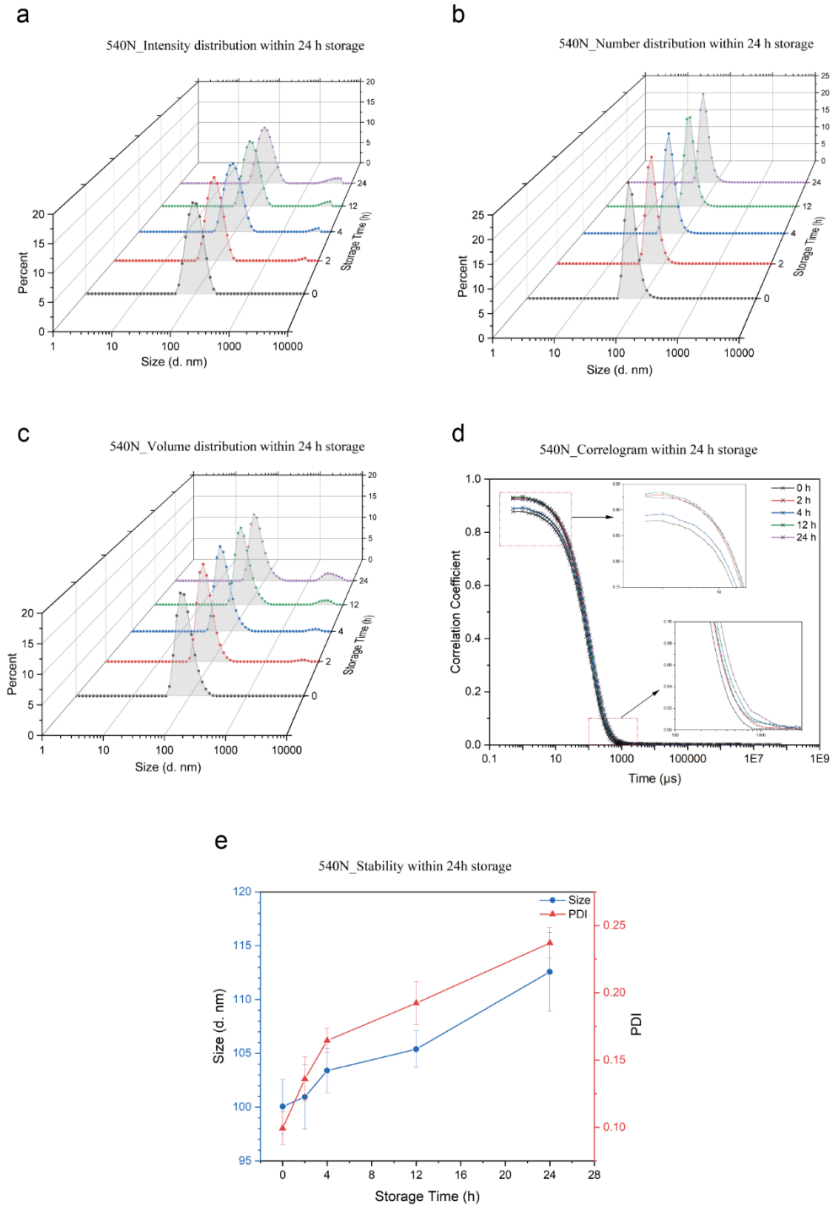


Figure 9. DLS profiles show the intensity (a), number (b) and volume (c) distribution of hydrodynamic size of 540 μM Nic BAIL vesicles suspension during 24 h storage in 10 mM pH7.4 PB at 25 ℃, with corresponding correlation coefficient vs decay time diagrams (d). The line graph (e) shows the changes in hydrodynamic size and PDI during storage. Data are presented as mean ± SD (n=3).

Following the formation of the vesicle-peptide nanoformulation, its stability was subsequently evaluated. The room-temperature (25 ℃) storage stability of Nic BAIL vesicles (540 μM) was evaluated by DLS over 24 h (Figure S4). At 0 h, the vesicle suspension exhibited a

unimodal nanoscale size distribution with a Z-average diameter of 100.06 ± 2.51 nm and a low PDI of 0.099 ± 0.012, indicating a relatively narrow particle-size distribution at the initial time point. Over time, the hydrodynamic diameter increased gradually to 112.56 ± 3.63 nm at 24 h, and in parallel, the PDI increased progressively to 0.237 ± 0.011, indicating a gradual broadening of the particle size distribution and increasing heterogeneity during storage. Inspection of the intensity- (Figure 9a), number- (Figure 9b), and volume-weighted size distributions (Figure 9c) showed that the vesicles remained dominated by a nanoscale main population throughout the 24 h period. However, minor larger-size populations became more apparent in the intensity- and volume-weighted distributions with increased storage time, particularly at later time points of 12 h and 24 h. The correlograms (Figure 9d) remained smooth and well-defined throughout the study, but shifted progressively toward longer decay times, consistent with a gradual increase in hydrodynamic size and heterogeneity. Collectively, these results indicate that Nic BAIL vesicles remain relatively stable during the first several hours of room-temperature storage, but undergo gradual particle growth and increasing heterogeneity over time, with early signs of aggregation becoming evident after 24 h. Therefore, the Nic BAIL vesicles used in subsequent formulations were all freshly prepared and used as soon as possible.

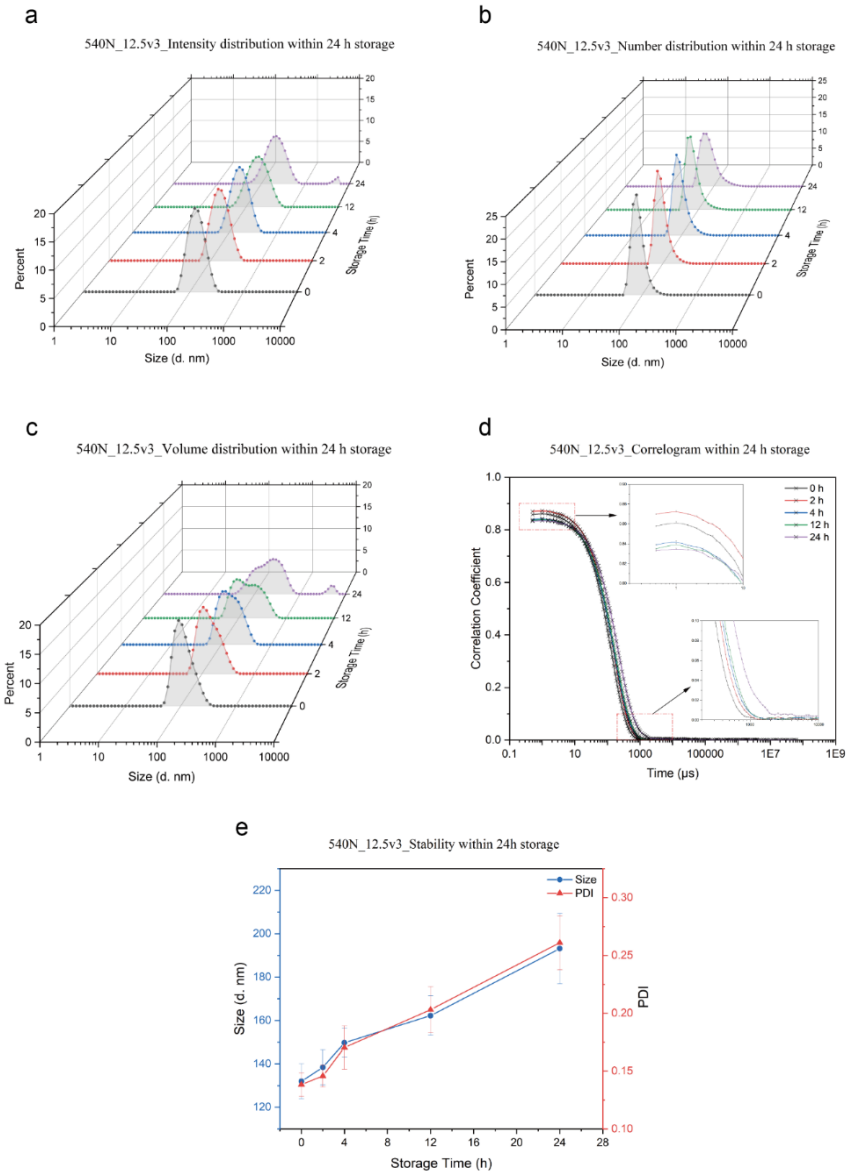


Figure 10. DLS profiles show the intensity (a), number (b) and volume (c) distribution of hydrodynamic size of 540 μM Nic BAIL-12.5 μM v3 nanoformulation during 24 h storage in 10 mM pH7.4 PB at 25 °C,

with corresponding correlation coefficient vs decay time diagrams (d). The line graph (e) shows the changes in hydrodynamic size and PDI during storage. Data are presented as mean ± SD (n=3).

Next, the room-temperature (25 °C) storage stability of the concentrated formulation (540 μM Nic BAIL-12.5 μM v3) was also evaluated by DLS over 24 h (Figure S5). At 0 h, the sample exhibited a unimodal nanoscale size distribution with a well-fitted correlogram, indicating a relatively homogeneous particle population. The fresh formulation displayed an initial hydrodynamic diameter of 131.95 ± 8.02 nm with a PDI of 0.138 ± 0.010. At 2 h, the intensity-weighted distribution (Figure 10a) remained dominated by a single nanoscale population, although the main peak shifted slightly toward larger diameters, accompanied by a modest increase in hydrodynamic diameter to 138.45 ± 8.13 nm and PDI to 0.145 ± 0.009. By 4 h, the intensity-weighted distribution still remained largely unimodal, whereas the volume-weighted distribution (Figure 10c) began to broaden toward larger diameters and showed a shoulder extending to around 200 nm. This trend became more evident at 12 h, where the contribution of the larger-size region increased further, while the intensity-weighted distribution continued to shift toward larger diameters. Consistently, the hydrodynamic diameter increased to 149.76 ± 6.65 nm at 4 h and 162.26 ± 9.05 nm at 12 h, while the PDI rose to 0.170 ± 0.019 and 0.203 ± 0.020, respectively, indicating progressive particle growth and increasing heterogeneity. Furthermore, it is worth noting that an additional micron-sized population became apparent in the intensity- and volume-weighted distributions at 24 h, indicating the emergence of a minor fraction of large aggregates. At this time point, the hydrodynamic diameter increased to 193.19 ± 16.19 nm and the PDI reached 0.261 ± 0.023. Throughout the storage period, the correlograms (Figure 10d) remained smooth but progressively shifted toward longer decay times, while the intercept tended to be lower at later time points, supporting a gradual increase in hydrodynamic size and increasing heterogeneity of the particle population.

Collectively, these results indicate that although the formulation retained a predominant nanoscale main population during the first several hours of room-temperature storage, it underwent progressive particle growth and increasing heterogeneity, with clear signs of aggregation after prolonged storage, particularly at 24 h. The proximity of the DSC transition to room temperature (25 °C) provides a hypothesis for the observed changes. Therefore, the formulation used in subsequent in-vitro cell experiments was freshly prepared and used as soon as possible to avoid deterioration.

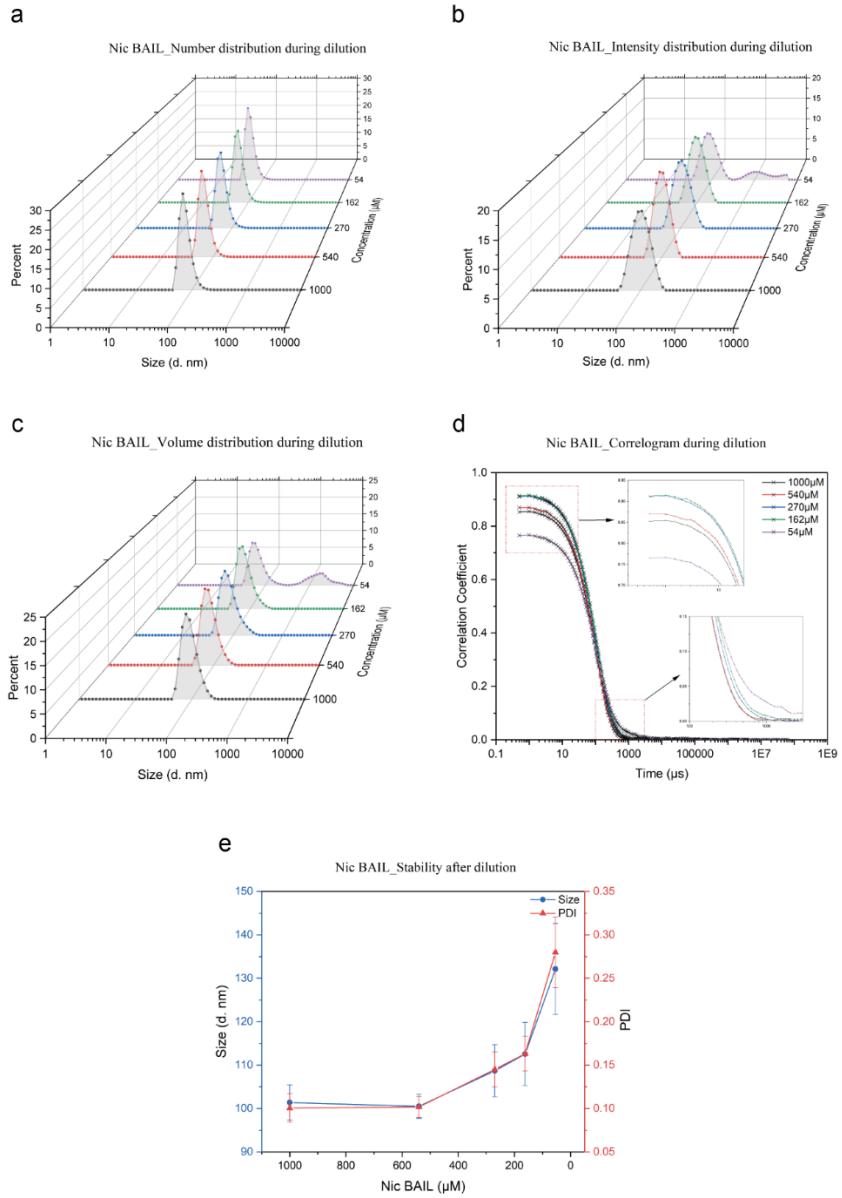


Figure 11. DLS profiles show the intensity (a), number (b) and volume (c) distribution of hydrodynamic size of 1000 μM Nic BAIL vesicles suspension during stepwise dilution with 10 mM pH7.4 PB at 25 °C, with corresponding correlation coefficient vs decay time diagrams (d). The line graph (e) shows the changes in hydrodynamic size and PDI during dilution process. Data are presented as mean ± SD (n=3).

Because the cell experiments were performed at a working concentration of 54 μM Nic BAIL-1.25 μM v3 rather than at the concentrated stock solution, the dilution stability of the carrier system was first evaluated by DLS (Figure S3). Freshly prepared Nic BAIL vesicles remained narrow, unimodal nanoscale size distributions upon dilution from 1000 μM to 540 μM, exhibiting hydrodynamic diameters of 101.38 ± 4.08 and 100.06 ± 2.51 nm, respectively, together with low PDI of 0.100 ± 0.016 and 0.099 ± 0.012, indicating homogeneous vesicle populations. Upon further dilution to 270 μM and 162 μM, the vesicles remained predominantly nanosized, but the peak broadened and shifted modestly toward larger diameters, with increases in hydrodynamic size and dispersity (108.68 ± 5.99 and 112.54 ± 7.26 nm; PDI = 0.145 ± 0.020 and 0.163 ± 0.020). The most pronounced change was observed at the concentration of 54 μM, where the hydrodynamic diameter increased to 132.13 ± 10.46 nm and the PDI rose to 0.280 ± 0.040. At this concentration, the intensity- (Figure 11a) and volume-weighted distributions (Figure 10c) showed a broadened main peak of nanoscale population together with an additional

small peak of larger-size aggregates. Consistently, the correlogram (Figure 11d) at 54 μM displayed a lower intercept and a more pronounced slow-decay tail, supporting reduced homogeneity and the presence of a minor fraction of larger, slowly diffusing particles.

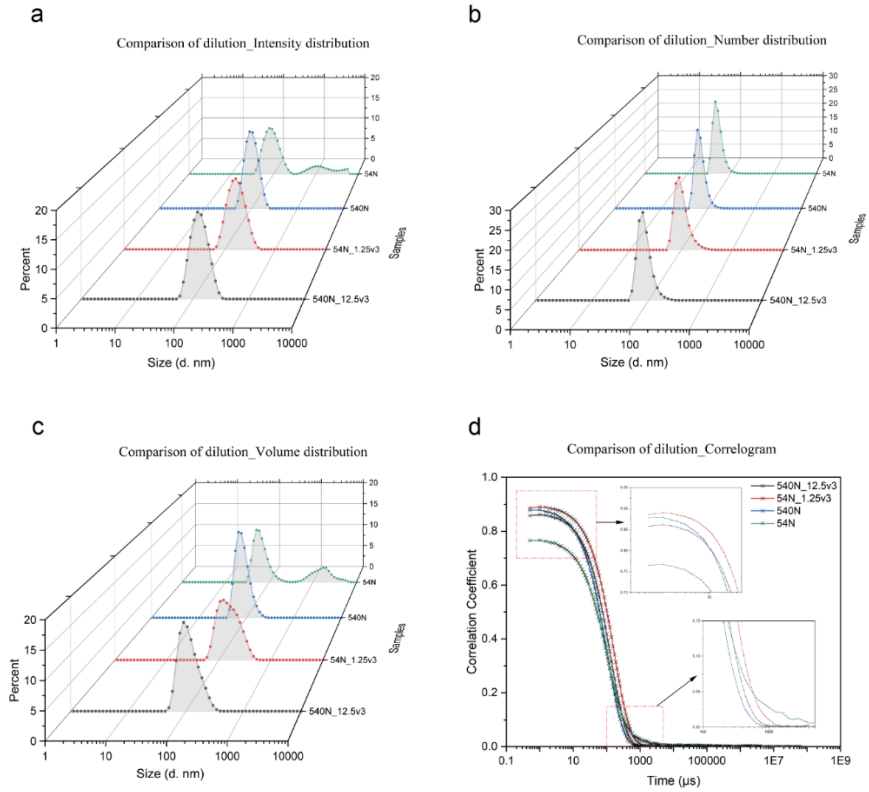


Figure 12. DLS profiles show the intensity (a), number (b) and volume (c) distribution of hydrodynamic size of 540 μM Nic BAIL-12.5 μM v3 nanoformulation and 540 μM Nic BAIL vesicles suspension during direct dilution to working concentration with 10 mM pH7.4 PB at 25 °C, with corresponding correlation coefficient vs decay time diagrams (d).

After completing the evaluation of the dilution stability of the carrier itself, the dilution behavior of the concentrated formulation was evaluated by direct dilution to the final working concentration used in cell experiments (Figure S6). Upon dilution, the peptide-loaded formulation remained dominated by a nanoscale population, but its hydrodynamic size increased from 131.95 ± 8.02 nm to 156.74 ± 4.93 nm, together with an increase in PDI from 0.138 ± 0.010 to 0.191 ± 0.025. The intensity- (Figure 12a), number- (Figure 12b), and volume-weighted distributions (Figure 10c) all shifted toward larger diameters. The diluted Nic BAIL-v3 formulation still showed a relatively well-defined main population without the pronounced large-size fraction observed in blank Nic BAIL at 54 μM. The correlogram (Figure 12d) also retained a high intercept and a smooth decay profile after dilution, despite shifting to longer decay times than the concentrated formulation. In contrast, dilution of blank Nic BAIL vesicles from 540 μM to 54 μM resulted in a stronger loss of homogeneity, as reflected by the appearance of a minor larger-size population in the intensity- and volume-weighted distributions and a marked rise in PDI from 0.099 ± 0.012 to 0.280 ± 0.040. Taken together, these results indicate that direct dilution to the biological working concentration affects the stability of the system, but the peptide-loaded system remains colloidally better defined than the corresponding blank Nic BAIL. This suggests that incorporation of v3 may partially suppress the severe heterogeneity that develops in the blank vesicle system upon dilution. However additional experiments need to be performed to statistically solidify this statement.

3.4 Planar bilayer electrophysiology of Nic BAIL-v3 formulations

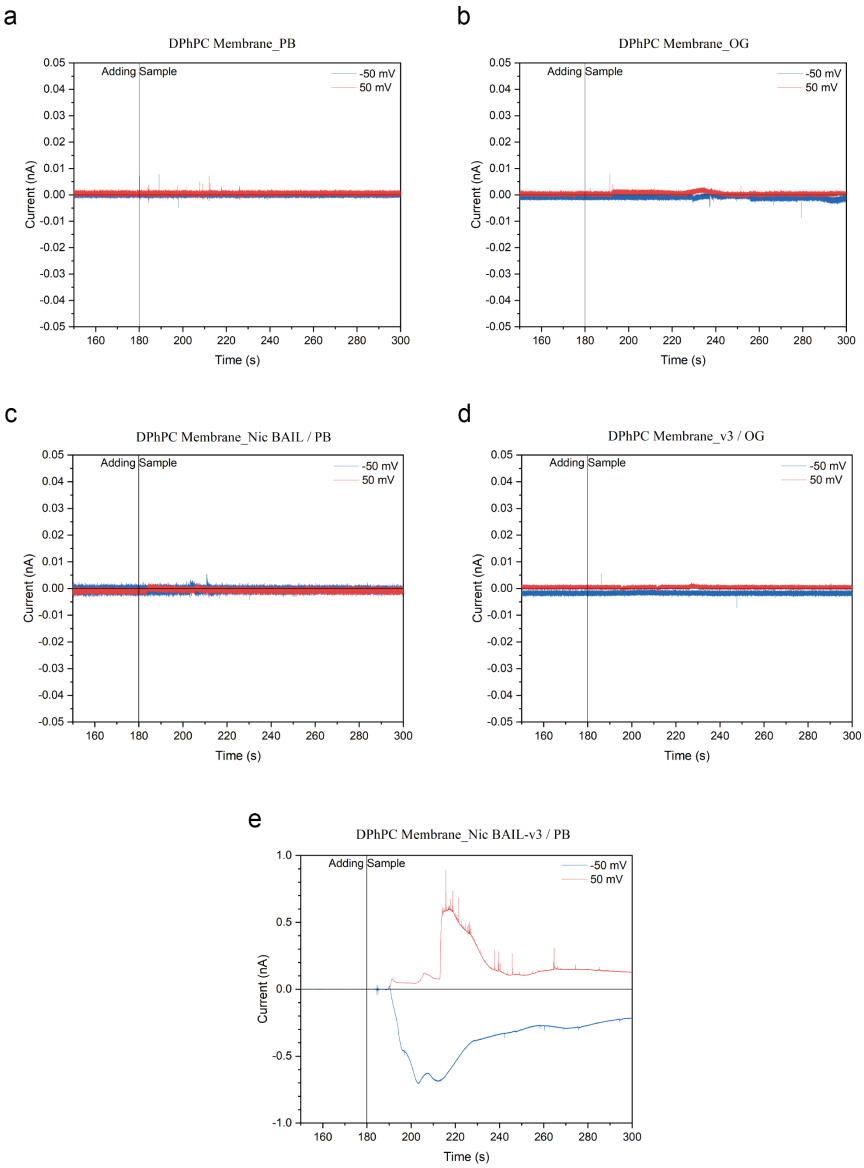


Figure 13. Planar lipid bilayer electrophysiology of Nic BAIL nanoformulation. Current responses measured at ± 50 mV before and after addition of the samples to preformed DPhPC bilayers: Phosphate buffer (PB) (a); n-octyl-β-d-glucoside (OG) (b); Nic BAIL / PB (c); v3/OG (d); and Nic BAIL-v3 / PB (e). The vertical grey line shows the time point of the sample addition.

Group	Voltage	Capacitance [pF]	Resistance [GΩ]	Mean [pA]	RMS [pA]
PB only	-50 mV	15.7806	21.2199	-0.65159	0.359295
	+50 mV	17.5689	14.3507	0.486676	0.38526
OG only	-50 mV	14.2381	8.86225	-0.929656	0.409356
	+50 mV	10.3756	28.4589	0.713966	0.32232
v3/OG	-50 mV	15.9736	4.93928	-1.92367	0.382629
	+50 mV	15.8314	22.8523	0.538545	0.32223
Nic BAIL/PB	-50 mV	11.2419	27.2439	-0.317554	0.267306
	+50 mV	10.4871	48.2395	0.205978	0.383077
Nic BAIL-v3/PB	-50 mV	31.0213	13.8316	-0.761127	0.780102
	+50 mV	32.7546	10.6792	0.276398	0.346151

Table 2. Electrophysiology parameters of DPhPC lipid bilayer before adding samples.

Group	Voltage	Capacitance [pF]	Resistance [GΩ]	Mean [pA]	RMS [pA]
PB only	-50 mV	15.1254	23.3514	-0.696444	0.354112
	+50 mV	17.1478	15.4127	0.499153	0.369405
OG only	-50 mV	18.4903	8.18503	-0.717375	0.50489
	+50 mV	10.335	22.4951	0.56213	0.315308
v3/OG	-50 mV	14.8804	6.77434	-1.70997	0.383064
	+50 mV	24.2809	23.4264	0.418278	0.324743
Nic BAIL/PB	-50 mV	9.1703	29.4768	-0.288876	0.260226
	+50 mV	9.9878	49.9099	0.213613	0.375697
Nic BAIL-v3/PB	-50 mV	26.1219	0.25004	-290.844	2.26658
	+50 mV	26.4418	0.18139	144.674	1.99844

Table 3. Electrophysiology parameters of DPhPC lipid bilayer after adding samples.

The v3 peptide was designed to interact with the transmembrane domain of HER2, its delivery requires interactions with the lipid environment of the cell membrane. Therefore, investigating the direct effects of the Nic BAIL-v3 formulation on lipid membrane integrity or permeability is important for evaluating its membrane-interacting properties. To investigate whether the Nic BAIL-v3 nanoformulation could alter membrane barrier properties, planar bilayer electrophysiology was performed using an artificial DPhPC lipid bilayer on the Orbit Mini platform.

Before sample addition, all bilayers exhibited stable baseline currents close to zero at both -50 and +50 mV, indicating successful formation of intact sealing membranes on cavities. This was further supported by the high membrane resistances which were in the GΩ range, and capacitance values consistent with formed bilayers (Table 2). Addition of PB alone (Figure 14a), OG alone (Figure 14b), Nic BAIL/PB (Figure 14c), or v3/OG (Figure 14d) caused only minor transient fluctuations and did not produce a sustained increase in current. In the control groups, the mean baseline current remained close to zero both before and after sample addition, and the noise reports showed only minimal changes. Likewise, membrane resistances remained in the GΩ range after treatment, indicating that neither buffer, OG, free v3 peptide, nor Nic BAIL alone could cause substantial bilayer permeabilization under these conditions v3/OG (Table 3). In contrast, addition of the Nic BAIL-v3 formulation induced a pronounced and persistent increase in transmembrane current at both holding potentials (Figure 14e). At -50 mV, the mean current shifted from -0.76 pA before treatment (Table 2) to -290.84 pA after treatment (Table 3), while it increased from 0.28 pA to 144.67 pA at +50 mV. This large current response was accompanied by an increase in baseline current fluctuations, from 0.78 to 2.27 pA at -50 mV and from 0.35 to 2.00 pA at +50 mV, indicating increased conductance and current fluctuations. RC analysis was consistent with increased conductance. For the Nic BAIL-v3 group, the membrane resistance dropped dramatically from 13.83 and 10.68 GΩ before treatment to 0.25 and 0.18 GΩ after treatment at -50 and +50 mV, respectively. At the same time, the membrane capacitance remained relatively high, decreasing moderately from 31.02 and 32.75 pF to 26.12 and 26.44 pF. By contrast, the control groups retained high RC values and near-baseline mean currents after sample addition.

Collectively, these findings demonstrate that the Nic BAIL-v3 formulation markedly increases ionic conductance of DPhPC bilayers, while the individual components and control group did not produce comparable sustained responses under the tested conditions. The increase in transmembrane current and decrease in membrane resistance are consistent with membrane permeabilization, potentially involving conductive membrane destabilization or perturbations of

the lipid bilayer structure. However, the artificial DPhPC bilayer lacks the molecular complexity of biological membranes, current observations cannot directly determine the extent or consequences of membrane permeability changes in living cells, necessitating further investigation in biological systems.

3.5 In vitro effects on cell viability in cell lines with different HER2/ERBB2 status

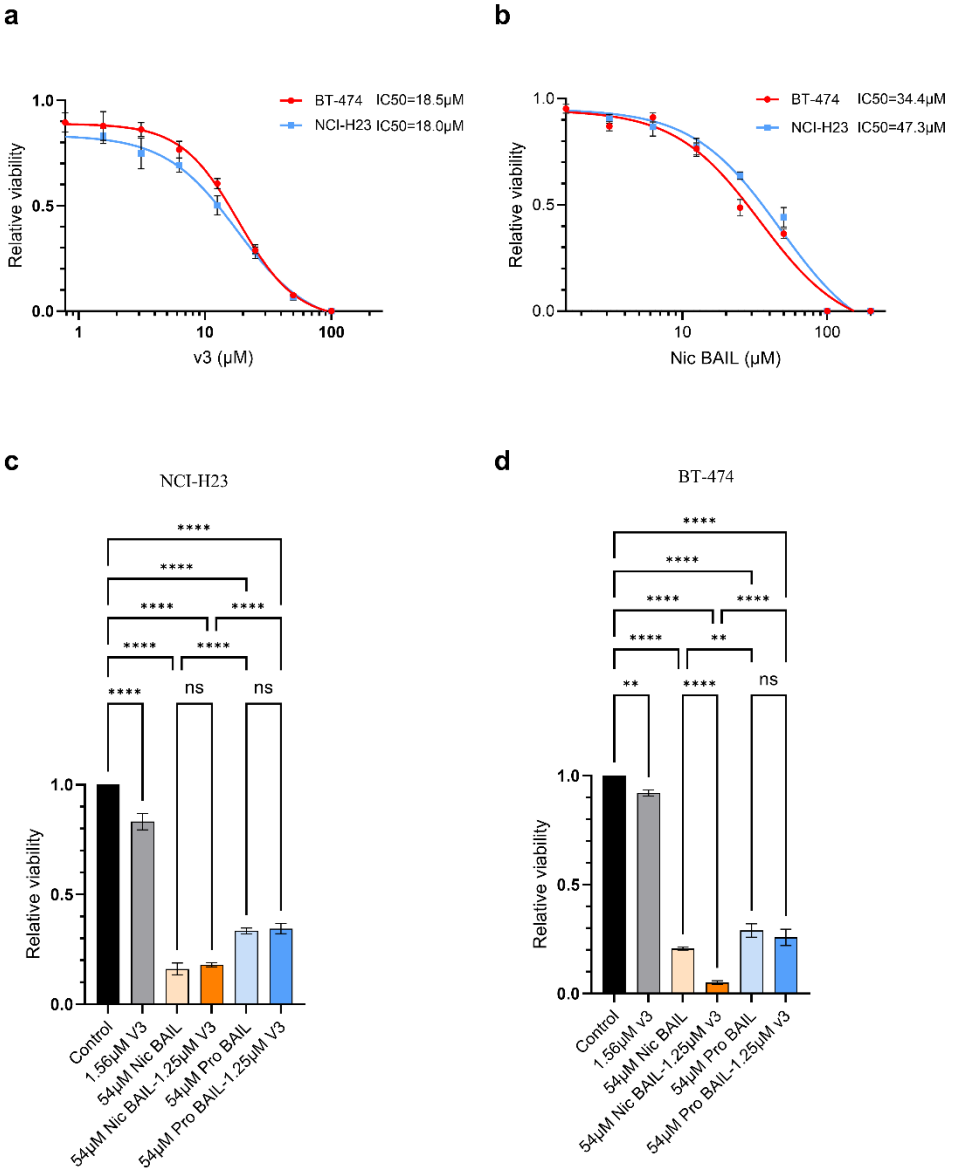


Figure 14. Dose-response curves and the half maximal inhibitory concentrations (IC_{50}) of v3 peptide (a) and Nic BAIL (b) on BT-474 and NCI-H23 cell lines; Cell viability of NCI-H23 (c) and BT-474 (d) after incubation for 48 h under different treatment conditions. Cell viability was normalized to the corresponding untreated control. Data are presented as mean ± SD from three independent experiments (n = 3). Statistical differences among treatment groups were evaluated using ordinary one-way ANOVA followed by Tukey's multiple comparisons test. Brackets indicate selected pairwise comparisons, with significance levels based on Tukey-adjusted p-values: ns, $p \geq 0.05$; *$p < 0.05$; **$p < 0.01$; ***$p < 0.001$; and ****$p < 0.0001$. Statistical significance was defined at $\alpha = 0.05$.

To evaluate the cellular effects of v3 and its SAIL-based formulations in different HER2-related biological contexts, two human cancer cell lines with different ERBB2 expression profiles were selected. BT-474 is a human breast cancer cell line derived from invasive ductal

carcinoma, characterized by HER2 overexpression and commonly classified as a hormone receptor-positive, HER2-positive luminal B model. NCI-H23 is a human non-small-cell lung cancer cell line derived from lung adenocarcinoma and was selected as a low ERBB2 expression comparator. The selection was based on the previous study by Abujubara et al.[183], which reported that the ERBB2 mRNA expression values of BT-474 and NCI-H23 were approximately 10.5 and 3.2, respectively (Table S1). To compare the effects of nanocarrier itself, a previously reported bi-amphiphilic ionic liquid Pro BAIL was included as a reference formulation[183]. It consists of an L-proline-derived cation [ProC_{10}] and a dodecyl sulfate anion [DS]. The fixed carrier concentration of 54 μM and peptide concentration of 1.25 μM were selected to maintain consistency with the formulation conditions investigated in the previous Pro BAIL study, thereby enabling comparison of the cellular responses to Pro BAIL-based and Nic BAIL-based formulations at matched concentrations. Cell viability was determined after 48 h of treatment using the CellTiter-Glo assay and normalized to the untreated control group.

Free v3 induced a concentration-dependent reduction in cell viability in both cell lines, with half-maximal inhibitory concentration (IC_{50}) values of 18.5 μM for BT-474 and 18.0 μM for NCI-H23 cells (Figure 14a). At 1.56 μM, a concentration slightly higher than the 1.25 μM v3 used in the nanoformulations, free v3 produced a significant but relatively modest reduction in viability in both cell lines compared with those induced by the carriers only and the nanoformulation. Together with the concentration-dependent response, these results indicate that within the concentration range relevant to the formulation, there is no pronounced difference in overall sensitivity to free v3 between the two cell lines under the experimental conditions. Nic BAIL also reduced cell viability in a concentration-dependent manner, with IC_{50} values of 34.4 μM in BT-474 cells and 47.3 μM in NCI-H23 cells (Figure 14b). The lower IC_{50} observed in BT-474 cells suggests a slightly greater sensitivity to Nic BAIL than NCI-H23 cells. At a fixed concentration of 54 μM used for the nanoformulation, Nic BAIL alone significantly reduced cell viability in both cell lines.

Despite this strong carrier-related effect, incorporation of 1.25 μM v3 into 54 μM Nic BAIL generated different responses in the two cell lines. In NCI-H23 cells, the Nic BAIL-v3 formulation did not significantly decrease viability compared to 54 μM Nic BAIL alone (Figure 14c). In contrast, in BT-474 cells, v3 incorporation resulted in a further reduction in viability compared with the corresponding Nic BAIL treatment alone. Although a substantial proportion of the overall viability reduction observed with the Nic BAIL-v3 formulation was attributable to the carrier itself, v3-associated additional reduction was still statistically significant (Figure 14d). Since 1.56 μM free v3 peptide produced only a relatively modest effect, the additional reduction observed in BT-474 cells cannot be attributed solely to the cytotoxicity of the peptide at the formulation concentration. The Pro BAIL formulations exhibited a different response profile. At a concentration of 54 μM, Pro BAIL alone reduced cell viability in both cell lines. However, incorporation of 1.25 μM v3 did not generate a statistically significant additional decrease in cell viability in both cell lines. Moreover, at the same nominal carrier concentration, Nic BAIL generally produced a greater reduction in cell viability than the corresponding Pro BAIL treatments in two cell lines. These differences indicate that the chemical identity of the SAILs carrier substantially influence the cellular response and further suggest that the biological effect of v3 is dependent on the carrier environment.

Collectively, these results indicate that both the carrier and the incorporated peptides contribute to the overall cellular response. Free v3 didn’t show intrinsic selectivity between BT-474 and NCI-H23 cells, while incorporation of v3 into Nic BAIL produced a statistically

significant additional reduction in viability specifically in BT-474 cells, which was not reproduced in NCI-H23 cells. This suggests that the biological activity of the Nic BAIL-v3 formulation may be influenced by the HER2/ERBB2 status of cells. Previous studies by Abujubara et al. reported that ErbB2 transmembrane-derived peptides can inhibit downstream PI3K/Akt and MAPK/ERK signaling pathways, and their incorporation into Pro BAIL nanocarriers enhances their activity through a combination of membrane-associated and signaling-related effects[183]. The current results are compatible with this model, but the strong carrier-associated effects occurred at 54 μM limit the distinguishment between peptide-specific activity and nanocarrier activity. Further investigations using lower carrier concentrations, FRET-based measurements of peptide direct association and cellular uptake investigation would be required to confirm this pharmacological synergy mechanism.

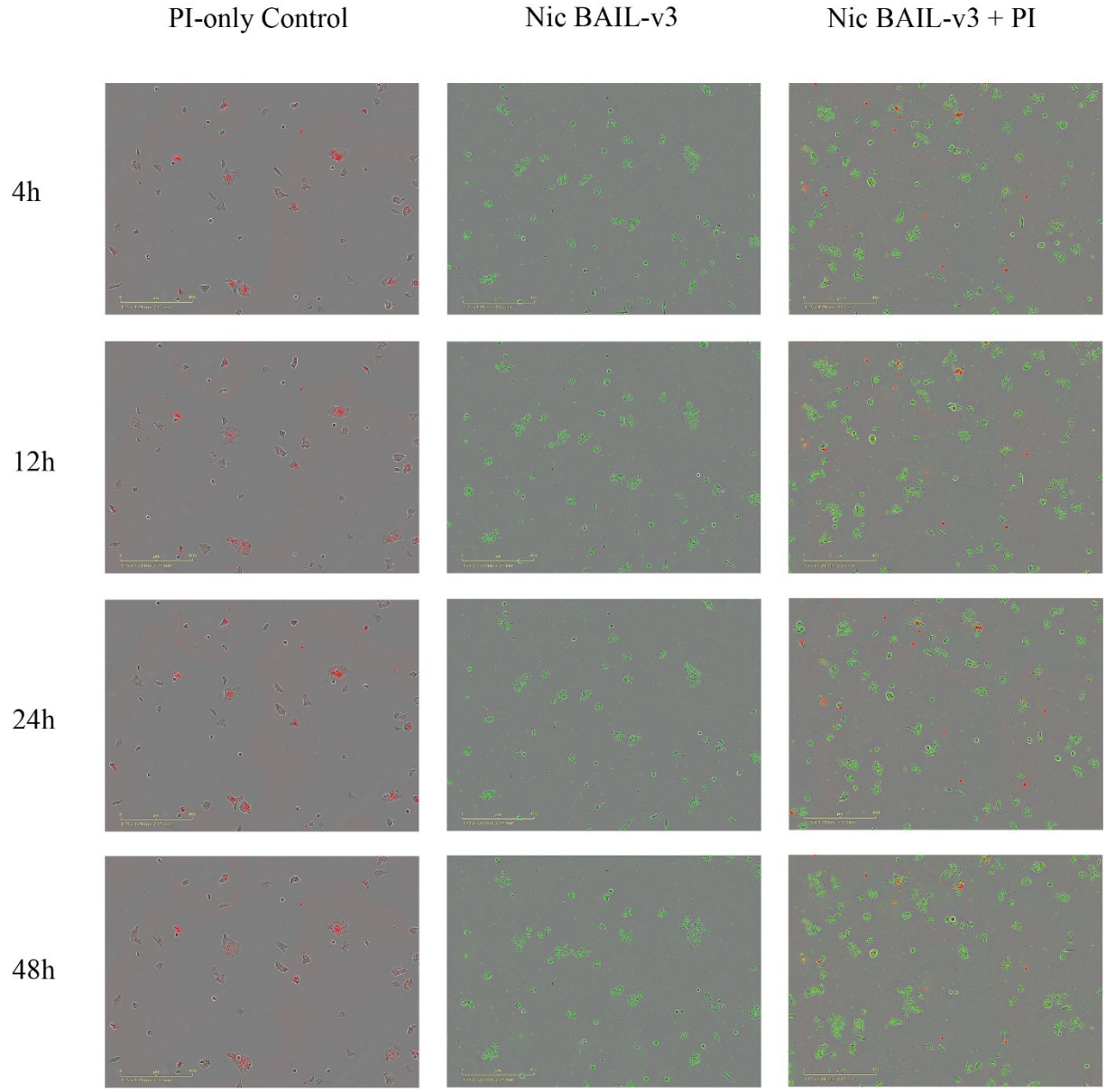


Figure 15. Representative phase-contrast and fluorescence overlay images show the morphology changes of BT-474 cells under different treatments. BT-474 cells were imaged at 4, 12, 24, and 48 h under three conditions: PI-only control, Nic BAIL-v3 formulation (54 μM Nic BAIL and 1.25 μM v3), and Nic BAIL-v3 formulation in the presence of PI.

To investigate the interaction of the Nic BAIL-v3 nanoformulation with BT-474 cells and observe changes in cell morphology during treatment, time-lapse live-cell imaging was performed

over 48 h. Cells were exposed to Nic BAIL-v3 nanoformulation and parallel imaging was also performed using propidium iodide (PI) staining to visualize cells exhibiting impairment of membrane integrity.

As shown in Figure 15, a distinct cell-associated green fluorescence signal was detectable after 4 h of incubation and persisted during the 48 h imaging period, indicating the association of the FAM-labelled v3 peptide with the cells. Morphologically, compared to the untreated control group, cells exposed to Nic BAIL-v3 nanoformulation progressively exhibited reduced spreading, increased cell rounding, and detachment. These deteriorated morphological changes were consistent with the decreased cell viability detected by CellTiter-Glo assay. Comparable green-fluorescence patterns and overall cellular morphology were also observed in the Nic BAIL-v3 groups with and without propidium iodide (PI), indicating that addition of PI did not alter the cellular response to the nanoformulation under the experimental conditions. However, no pronounced time-dependent increase in PI-positive cells (red) was visually apparent during the imaging period, suggesting that the progressive deterioration of cellular morphology was not accompanied by the acute loss of membrane integrity. Previous planar bilayer electrophysiology experiments demonstrated that the Nic BAIL-v3 nanoformulation exhibited membrane activity by increasing ionic conductance across artificial lipid bilayers. In contrast, PI fluorescence depends on the ability of a relatively large, membrane-impermeant dye to enter cells and interact with intracellular nucleic acids. Therefore, increased ionic conductance across an artificial lipid bilayer does not necessarily imply increased permeability to PI in living cells, particularly given the additional structural complexity of biological membranes. Consequently, the relationship between the membrane activity observed in the planar bilayer model and potential alterations in cellular membrane integrity remains to be further investigated and elucidated.

In summary, the present findings demonstrate that the combined application of v3 peptide and Nic BAIL vesicles enhances the inhibitory effect in a cell-line-dependent manner. Together with the sustained association of v3 peptide to BT-474 cells and the observed morphological deterioration, highlighting the potential of this nanoformulation as a novel strategy for HER2-targeted therapy.

3.6 Sustainability and Ethical Considerations

The development of new drug delivery systems also involves social, ethical, and environmental considerations which beyond their physicochemical and biological performance. The Nic BAIL-v3 nanoformulation investigated in this study represents an investigative approach to addressing the delivery challenges of highly hydrophobic ErbB2 transmembrane peptides. Such technologies may contribute to the future development of other peptide-based anticancer strategies.

From an ethical perspective, this study currently involves neither animal experiments nor the human participants, and the biological evaluation was evaluated using human cancer cell lines. Nevertheless, the membrane-active Nic BAIL nanocarriers raises important safety concerns. The significant reduction in cell viability induced by Nic BAIL alone indicates that the carrier itself possesses intrinsic biological activity, which may limit its suitability as a selective drug delivery vehicle. Before further therapeutic investigation, it is essential to systematically evaluate its effects on non-malignant cells, as well as potential off-target toxicity. A responsible scientific report requires to distinguish experimentally demonstrated effects from proposed mechanisms, particularly given that the peptide localization and direct association with receptor in this study have not yet been directly verified.

Environmental sustainability is another important consideration. Although ionic liquids can offer desired physicochemical properties, they are not inherently environmentally benign. These properties remain unclear because this study did not investigate the biodegradability, environmental persistence, or ecotoxicity of Nic BAIL. Furthermore, the synthesis and purification of Nic BAIL and peptides involved organic solvents and reagents that pose health and environmental risks, including dichloromethane, dimethylformamide, trifluoroacetic acid, and hexafluoroisopropanol, which require appropriate handling and waste management. Considering that the experiments were conducted in a suitable laboratory setting, researchers were equipped with protective equipment, risk assessments of the experiments and required reagents were performed beforehand, and all waste properly handled by specialized recycling companies, the risk of harm to personnel and the environment was minimal.

Overall, further development of Nic BAIL-based peptide delivery systems should integrate biological safety, environmental assessment, and responsible manufacturing which are essential for determining whether the potential therapeutic benefits can justify the associated ethical, environmental, and societal risks.

4. Conclusions and Perspectives

This study represents a nicotinium-based bi-amphiphilic surface-active ionic liquid (Nic BAIL) vesicle system for the delivery of the highly hydrophobic ErbB2 transmembrane peptide v3. Nic BAIL and the ErbB2-TM peptide variants were successfully synthesized, purified, and characterized.

After incorporation of v3 peptide, the Nic BAIL-v3 nanoformulation showed a vesicular structure and retained a predominant nanoscale population after dilution to the biological working concentration. However, these observations did not directly establish peptide loading or its localization within the vesicular structures. Planar bilayer electrophysiology demonstrated that Nic BAIL-v3 nanoformulation perturbed membrane electrical properties of artificial DPhPC bilayer, suggesting direct interaction with membranes and ability to alter membrane electrical barrier properties. In vitro Cell experiments showed that both free v3 and Nic BAIL reduced viability in a concentration-dependent manner. Importantly, the addition of 1.25 μM v3 into Nic BAIL caused a further significant reduction in HER2-high expression BT-474 cell viability, while this enhancement was not observed in HER2-low expression NCI-H23 cells. However, the present results are not sufficient to establish HER2-specific targeting or pharmacological synergy effect between Nic BAIL and v3. Qualitative live-cell imaging showed cell-associated accumulation of v3 peptide together with progressive morphological deterioration, but did not provide direct evidence of peptide internalization or loss of membrane integrity. These findings provide a preliminary basis for further investigation of membrane interactions and potential receptor-related biological activity of Nic BAIL-v3 nanoformulation.

Future studies should focus on determining peptide localization within Nic BAIL vesicles and quantifying peptide loading. The concentration-dependent biological effects of Nic BAIL-v3 should be evaluated using lower carrier concentrations that can reduce intrinsic carrier-associated viability inhibition. The effects of the nanoformulation on HER2 activation and downstream PI3K/Akt and MAPK/ERK signaling should be examined using appropriate molecular assays. More direct mechanistic studies should be conducted, such as using Förster resonance energy transfer (FRET) to provide further information on proximity and dimerization between receptor and peptides. Additionally, pharmacological, toxicological, metabolic, and pharmacokinetic properties of Nic BAIL should be systematically evaluated.

5. Experimental Section

5.1 Synthesis of nicotinium-based bi-amphiphilic surface-active ionic liquid (Nic BAIL)

5.1.1 Synthesis of dodecyl 2-bromoacetate

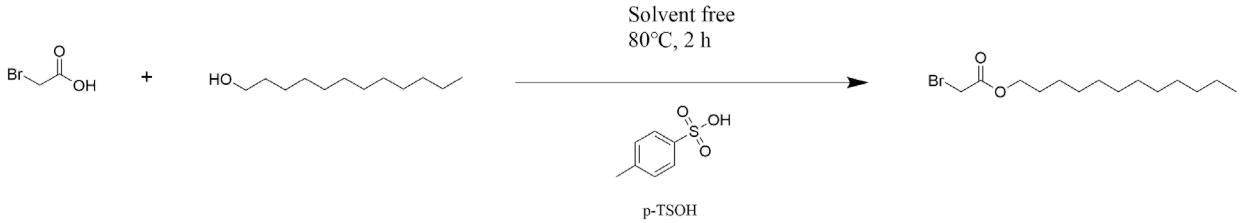


Figure 16. Synthetic scheme of dodecyl 2-bromoacetate.

Dodecyl 2-bromoacetate was synthesized by esterification of dodecan-1-ol with bromoacetic acid under solvent-free conditions. Dodecan-1-ol (10 mmol, 1.8634 g), bromoacetic acid (1.2 equiv, 12 mmol, 1.6674 g), and catalytic p-toluenesulfonic acid (0.098 g, ca. 5 mol %) were stirred at 80 °C for 2 h. Reaction progress was monitored by thin-layer chromatography (TLC) on silica gel G plates using *n*-hexane/ethyl acetate (98:2, v/v) as the mobile phase, and the spots were visualized by iodine staining (Rf = 0.3-0.6). After completion, the reaction mixture was cooled to room temperature, dissolved in DCM, and washed sequentially with saturated $NaHCO_3$ solution (1×) and H_2O (3×). The organic phase was dried over anhydrous Na_2SO_4 and then concentrated using a rotary evaporator under vacuum at 40℃ to afford dodecyl 2-bromoacetate as a slightly viscous, transparent, oily liquid product. The product was stored under N_2 at 4 ℃.

5.1.2 Synthesis of (R)-1-(2-(dodecyloxy)-2-oxoethyl)-3-(1-methylpyrrolidin-2-yl)pyridin-1-ium bromide (Nic MAIL)

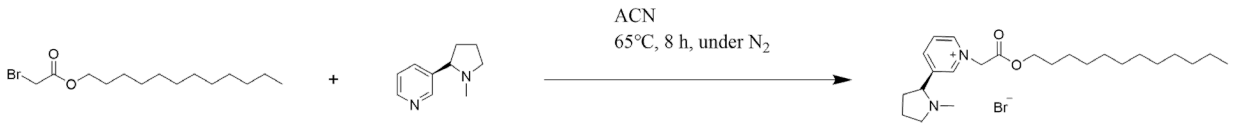


Figure 17. Synthetic scheme of [C_{12}ENic] [Br] (Nic MAIL).

Nic MAIL was prepared by quaternization of nicotine with dodecyl 2-bromoacetate. 1.0 mmol nicotine (162 mg, 161 μL) was dissolved in 5.0 mL ACN under N_2, and 1.2 mmol dodecyl 2-bromoacetate (1.2 equiv, 369 mg, 348 μL) was added dropwise with stirring. After homogenization at room temperature, the reaction mixture was heated to 65 °C under N_2 for 8 h. After completion, the mixture was cooled to room temperature, and the solvent was removed by a rotary evaporator under vacuum at 38 ℃. The crude product was dissolved in ACN/ H_2O (1:1, v/v) and purified by reversed-phase flash chromatography on a Biotage Isolera One system with the Biotage Sfär C18 D Duo column (100 Å, 30 μm, 30 g). Eluent A was H_2O with 0.1% TFA (v/v) and eluent B was ACN with 0.1% TFA (v/v). Elution was performed at a flow rate of 25 mL min^{-1} with UV detection at 254 and 280 nm with a collection threshold of 25 mAU. The gradient was as follows: 10% B for 3 column volumes (CV) for equilibration, 10% B for 1 CV, 10-30% B over 3 CV, 30-51% B over 3.4 CV, 51% B for 0.2 CV, 51-60% B over 1.5 CV, 60-95% B over 3 CV, and 95% B for 1 CV. Product-containing fractions from CV 7-10 were combined and concentrated by rotary evaporator under reduced pressure at 38 ℃, and further dried under high vacuum for 3 h to afford Nic MAIL as a highly viscous, light yellow liquid product. The

purified product was stored under N_2 at 4 °C.

5.1.3 Synthesis of (R)-1-(2-(dodecyloxy)-2-oxoethyl)-3-(1-methylpyrrolidin-2-yl)pyridin-1-ium dodecyl sulfate (Nic BAIL)

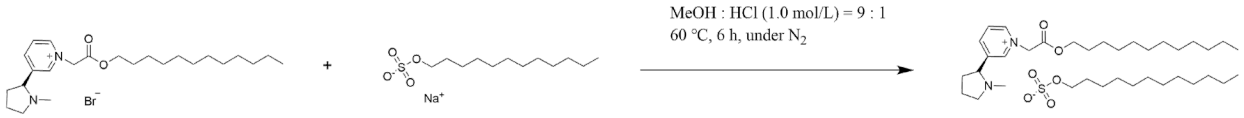


Figure 18. Synthetic scheme of [C_{12}ENic] [DS] (Nic BAIL).

Nic BAIL was obtained by anion exchange from Nic MAIL. 800 mg Nic MAIL was dissolved in 45 mL MeOH, and 5 mL 1.0 mol L^{-1} HCl was added. After stirring at room temperature for 10 min, 490 mg SDS (1.0 equiv) was added, and the reaction mixture was heated to 60 °C and stirred under N_2 for 6 h. Upon reaction completion, the reaction mixture was concentrated by a rotary evaporator under vacuum at 38°C. The flask was then connected to a high vacuum pump and run for 3 h to remove residual solvent. The crude product was dissolved in 50 mL DCM and filtered to remove inorganic salts. The organic phase was washed with 50 mL H_2O (3 ×) until no chloride was detected in the aqueous layer by the $AgNO_3$ test. The DCM layer was dried over anhydrous Na_2SO_4, concentrated by rotary evaporator under reduced pressure at 38 °C, and further dried under high vacuum for 3 h to afford Nic BAIL as a light yellow, sticky solid product. The product was stored under N_2 at 4 °C.

5.2 Characterization of Nic BAIL

5.2.1 Nuclear magnetic resonance (NMR) spectroscopy analysis

NMR spectra were recorded at the Swedish NMR Centre, University of Gothenburg, on a 600 MHz Oxford magnet (600#2, violet). Approximately 10 mg of product was dissolved in 1000 μL of $CDCl_3$ and transferred into 3 mm NMR tubes. All spectra were acquired at 25 °C.

5.2.2 Differential scanning calorimetry (DSC) measurement

DSC thermograms were recorded using a TGA/DSC 3+ STARe system (METTLER TOLEDO) under a N_2 atmosphere. Before measurement, samples were dried under vacuum for at least 24 h. Heating and cooling scans were performed at a rate of 5 °C min^{-1}. Thermograms from the third and fourth cycles, which showed good reproducibility, were used for analysis and presentation.

5.2.3 Direct-infusion ESI-MS characterization

Nic MAIL and BAIL were characterized by direct-infusion electrospray ionization mass spectrometry in both ESI+ and SEI- modes. Stock solutions were prepared by dissolving 1.0 mg of the product in 1.0 mL of H_2O/ACN (50:50, v/v) and were subsequently diluted 1000-fold with the same solvent mixture to a final concentration of 1.0 μg mL^{-1}. The diluted sample was loaded into a microsyringe and continuously infused into the ESI source using a syringe pump at a flow rate of 10 μL min^{-1}. Mass spectra were acquired over an m/z range of 100-4000 using a Waters SYNAPT G2-Si High Definition MS System at sensitivity mode with a scan time of 1.0 s for 20 min. The parameters of ESI source at positive mode were: capillary, 3.0 kV; sampling cone, 30 V; source offset, 50 V; source temperature, 120 °C; desolvation temperature, 450 °C; cone gas, 25 L h^{-1}; desolvation gas, 800 L h^{-1}; nebuliser, 6.5 Bar. The parameters of ESI source at negative mode were: capillary, 2.0 kV; sampling cone, 30 V; source offset, 50 V; source temperature, 120 °C; desolvation temperature, 400 °C; cone gas, 5 L h^{-1}; desolvation gas, 500 L h^{-1}; nebuliser, 3.0 Bar.

5.3 Purification of ErbB2-TM peptides (v1, v2, v3)

5.3.1 Preparative HPLC purification

All crude ErbB2-TM peptides (v1, v2, and v3) were purified by preparative HPLC using a Waters 1525 Binary HPLC Pump equipped with a Waters 2996 PDA detector. Separations were carried out on an ISAspher 100-5 Si (RP) column (250 × 20 mm) at room temperature (25 ℃). Eluent A was H_2O with 0.1% TFA (v/v) and eluent B was ACN with 0.1% TFA (v/v), and the flow rate was set to 10 mL min^{-1}. For purification, each crude peptide was dissolved in MeOH/ H_2O /HFIP (4:4:2, v/v/v) to a final concentration of 20 mg mL^{-1}. The column was equilibrated at 85% B/15% A for 15 min before the first injection. Peptide samples were injected at a volume of 1.0 mL per run, and elution was performed using a linear gradient from 85% B to 50% B over 60 min. For v2 and v3 peptides with FAM, eluent was monitored at 450 nm and collected manually from 31.5 to 40.5 min; for v1 peptide without FAM, eluent was monitored at 214 nm and collected manually from 30 to 39 min. The collected fractions were pooled, pre-cooled in liquid nitrogen, and then lyophilized to remove the solvent.

5.3.2 Analytical HPLC analysis

All peptides were analysed by analytical HPLC using a Waters e2695 Separations Module equipped with a Waters 2998 PDA detector with an ISAspher 100-3 Si (RP) column (50 × 4.6 mm) maintained at 50 ℃. 500 μM peptide solution was prepared by dissolving the required amount of peptide powder in ACN/H_2O (90:10, v/v). Eluent A was H_2O with 0.1% TFA (v/v) and eluent B was ACN with 0.1% TFA (v/v). The flow rate was set to 2.0 mL min^{-1}, and the injection volume was 10 μL. Before the first run, the column was equilibrated at 95% B/5% A for 15 min. Samples were then analyzed using the following gradient: 95% B hold for 2 min, 95% B to 70% B over 3 min, and then 70% to 50% B over 5 min. Chromatograms were extracted at 214 and 450 nm, the purity of peptide was analyzed at 214 nm based on peak area normalization method.

5.3.3 LC-MS analysis

Peptide samples were analyzed by LC-MS using a Waters SYNAPT G2-Si High Definition MS System coupled to a Waters ACQUITY UPLC System. Chromatographic separation was performed on an ISAspher 100-3 Si (RP) column (50 × 3.0 mm) maintained at 30 ℃. The mobile phases consisted of H_2O with 0.1% (v/v) formic acid (FA) (eluent A) and ACN with 0.1% (v/v) FA (eluent B). For analysis, peptide samples were prepared as highly diluted solutions in ACN/H_2O (50:50, v/v). Prior to analysis, the column was equilibrated at 85% B/15% A for 15 min at a flow rate of 0.5 mL min^{-1}. Subsequently, 1.0 μL of the peptide solution was injected and analyzed using a gradient from 85% B to 50% B over 10 min at a flow rate of 0.5 mL min^{-1}. Mass spectrometric detection was carried out in ESI+ mode using the method MS-Sen-ESIpos-100-4000_12min.

5.4 Generation of Nic BAIL vesicles and incorporation of peptides

32.75 mg Nic BAIL was dissolved in 5.0 mL 10 mM phosphate buffer (pH 7.4) to obtain a 10 mM stock solution. The stock solution was diluted to 1 mM and subjected to 10 freeze-thaw cycles while being maintained above the phase transition temperature in a 37 ℃ water bath before extrusion. Vesicles were generated at 37 ℃ by sequential extrusion through 0.2 and 0.1 μm polycarbonate (PC) membranes (20 passes each) using an Avanti mini-extruder. The extruded vesicle suspension was filtered through a 0.45 μm polytetrafluoroethylene (PTFE) membrane and used as soon as possible. 500 μM stock solutions of v1-3 peptides were prepared by dissolving 2.21 mg of v1, 2.48 mg of v2, and 2.67 mg of v3 in 1500 μL of 1,1,1,3,3,3-hexafluoroisopropanol (HFIP), separately. An appropriate volume of peptide stock

solution was added to the preformed Nic BAIL vesicle suspension to obtain the target peptide concentration in the Nic BAIL-peptide formulation. The mixtures were kept under reduced pressure for 2 h to remove HFIP before use.

5.5 Characterization of vesicle-peptide complexes

5.5.1 Dynamic light scattering (DLS) measurement

Dynamic light scattering (DLS) measurements were performed at 37 ℃ to determine the size distribution of vesicles using a Zetasizer Nano ZS (Malvern Instruments, U.K.). The quality and reliability of the measurements were assessed from the PDI values, correlograms and instrument quality reports. Scattered light was detected at a backscattering angle of 173°. Before measurement, samples were first vortexed and then added into cuvettes and equilibrated in the instrument for 120 s. Three consecutive measurements were then performed, and the results were presented as mean ± standard deviation.

5.5.2 Cryogenic transmission electron microscopy (Cryo-TEM) imaging

For the Cryo-TEM imaging, 10 mM Nic BAIL was prepared and extruded to obtain a stock vesicle suspension. Dilution of the Nic BAIL vesicles and preparation of concentrated formulation of 5400 μM Nic BAIL-125 μM peptide were performed using the same method described in Section 5.4. Quantifoil R1.2/1.3 Cu 300-mesh grids were glow-discharged under air atmosphere using negative polarity at 20 mA for 60 s. A 3 μL sample drop was applied to the glow-discharged grid and vitrified using a Thermo Fisher Vitrobot Mark IV plunge-freezing system. The Vitrobot chamber was maintained at 4 ℃ and 100% humidity. After sample application, the grid was allowed to equilibrate for 10 s, blotted for 5 s, and subsequently plunge-frozen in liquid ethane. Cryo-TEM images were acquired on a Talos Arctica transmission electron microscope operated at 200 kV and equipped with an X-FEG source and a Falcon III detector. Suitable imaging regions of the grid were selected based on ice quality and visibility. Images were recorded at a magnification of ×36000 and analyzed with ImageJ.

5.5.3 Planar bilayer electrophysiology of the vesicle-peptide complexes

The membrane activity of Nic BAIL-v3 complexes was investigated by planar bilayer electrophysiology using an Orbit Mini miniaturized bilayer recording device (Nanion Technologies, Munich, Germany) equipped with a MECA 4 recording chip (Ionera Technologies, Freiburg, Germany). A four-well chip containing 100 μm apertures was used. The current across each well was recorded at a sampling frequency of 1.25 kHz, a bandwidth of 0.625 kHz, and a current range of -2 to +2 nA. All measurements were conducted at room temperature. Each chip well was filled with 150 μL of 50 mM phosphate buffer (pH 7.4). 5.0 mg/mL stock solutions of 1,2-diphytanoyl-sn-glycero-3-phosphocholine (DPhPC, Avanti Polar Lipids, USA) were prepared in electronic-grade octane. Bilayers were formed across the cavities by the air bubble method. Successful bilayer formation was indicated by negligible baseline current fluctuations, whereas saturated current signals (±2 nA) indicated the absence of a stable membrane. In cases of unstable current traces or blocked apertures, the membrane was disrupted using the Zap function and reformed. After bilayer formation, the membrane was allowed to equilibrate for 60 s. Resistance and capacitance (RC) were then estimated using a predefined voltage protocol consisting of a triangular wave and a seal-test pulse. For the triangular wave, the amplitude (Vamp) was set to 100 mV and the period (Tperiod) to 20 ms. For the seal-test pulse, the pulse amplitude (Vpulse) was set to 100 mV, the pulse duration (Tpulse) to 200 ms, and the holding time (Thold) to 500 ms. Following the initial RC estimation, a constant holding potential of either -50 or +50 mV was applied, and the baseline current was recorded for 120 s. At 180 s, 15

μL of samples were added directly to the chip well to reach the desired final concentration while continuous current recording was maintained. After the current reached a new steady state after sample addition, RC estimation was repeated using the same voltage protocol to assess bilayer integrity after treatment.

5.6 In vitro cell experiments with Nic BAIL-v3 nanoformulation

5.6.1 Cell lines and culture

Human BT-474 and NCI-H23 cell lines were obtained from the American Type Culture Collection (ATCC). Cells were maintained in RPMI-1640 medium supplemented with 10% fetal bovine serum (FBS), 2 mM glutamine and 0.1% gentamicin and cultured in a humidified incubator at 37 ℃ under 5% CO_2. Cells were cultured to 70-80% confluence before being harvested for use or passaged. Cells were detached from the plates using TrypLE Express (Gibco) and resuspended in the fresh media at known concentration. Cell concentration and viability were determined by trypan blue exclusion using a Countess 3 FL Automated Cell Counter (Invitrogen) prior to use in subsequent studies.

5.6.2 Cell viability assay

For the peptides only treatment, a desired volume of peptide-HFIP stock solution corresponding to the required amount of peptide was dried under vacuum and redissolved in 25 mM Octyl β-D-glucopyranoside (OG) prepared in 10mM PH 7.4 PB to obtain a peptide stock concentration of 100 μM. 1000 μM Nic BAIL vesicle suspension and the 540 μM Nic BAIL-12.5μM v3 stock were prepared using the procedure described before. All stock solutions were diluted with corresponding culture medium to reach final assay concentrations. In all treatment groups, the volume of the added dose was kept below 3% (v/v) of the total volume of the final well volume. The cells were seeded in a white opaque 96-well plate with a clear bottom at a density of 5000 cells per well and allowed to attach prior to treatment. Cells were subsequently incubated with peptide, vesicles, and peptide-vesicle nanoformulation for 48 h. Following incubation, the cell viability was assessed using the CellTiter-Glo Luminescent Cell Viability Assay (Promega #G7570, Madison, Wisconsin) according to the manufacturer's instructions. Luminescence was recorded on a BioTek Synergy HTX plate reader (Agilent) and was used as an indicator of metabolically active cells. Cell viability was expressed as a percentage relative to the untreated control group. Each treatment was performed in triplicate in three independent experiments.

5.6.3 Live cell imaging

Live-cell imaging was performed using an Incucyte SX5 System (Sartorius) equipped with green, orange, and near-infrared (G/O/NIR) optical channels. Cells were maintained under standard culture conditions during imaging and monitored over time. The orange and green channels were used to monitor PI and Nic BAIL-v3 nanoformulation which contains visualizable FAM-labelled v3 peptide. Images were acquired at predefined time points for qualitative assessment of the spatial distribution of fluorescent peptide and cellular morphology.

5.7 Statistical Analysis

Data processing and presentation were performed using Microsoft Excel (Microsoft Corporation), Origin 2021 (OriginLab Corporation), and GraphPad Prism 10 (GraphPad Software, Boston, MA, USA). Data are presented as mean ± standard deviation (SD), unless otherwise stated. Statistical significance was defined as $p < 0.05$, with significance levels indicated as ns (not significant, $p \geq 0.05$), *$p < 0.05$, **$p < 0.01$, ***$p < 0.001$, and ****$p < 0.0001$. The number of replicates is specified in the corresponding figure legends.

Acknowledgements

I would like to express my sincere gratitude to Professor Alesia A. Tietze for giving me the opportunity to carry out my thesis project in her research group and for her continuous guidance and support throughout the past year. I am also very grateful to Daniel, Maryna, Luisa, Enoch, and Helal for their generous help, valuable discussions, and practical guidance during my thesis work, as well as for giving me the opportunity to contribute to and learn from other research projects within the group. Their support and willingness to share their knowledge greatly enriched my research experience.

I would also like to sincerely thank Professor Volkan Sayin for providing the opportunity and facilities to conduct the cell experiments in his group. My special thanks go to Dorota for her patient, hands-on guidance throughout the cell culture and in vitro experiments. Her practical support and detailed instruction were essential in helping me carry out this part of the project.

Finally, I would like to thank everyone who contributed, directly or indirectly, to this thesis project. I am deeply grateful for all the discussions, assistance, advice, encouragement, and support that makes this year both scientifically rewarding and personally memorable.

Statement on the Use of AI Tools

OpenAI's ChatGPT was used as a supplementary tool in brainstorming, literature discussion, and the understanding and interpretation of relevant scientific concepts. The draft and structural framework were written by the author, and ChatGPT was used to assist with translation and linguistic refinement, including improvements to grammar, clarity, and academic expression. All AI-assisted outputs were reviewed and revised by the author. The final wording, scientific interpretations, and conclusions reflect the author's own revisions and academic judgment. The author assumes full responsibility for the accuracy, originality, and integrity of this thesis.

References

[1] Wolff, A. C., Somerfield, M. R., Dowsett, M., Hammond, M. E. H., Hayes, D. F., McShane, L. M., Saphner, T. J., Spears, P. A., & Allison, K. H. (2023). Human Epidermal Growth Factor Receptor 2 Testing in Breast Cancer: ASCO-College of American Pathologists Guideline Update. *Journal of clinical oncology : official journal of the American Society of Clinical Oncology*, *41*(22), 3867–3872.

[2] Bartley, A. N., Washington, M. K., Colasacco, C., Ventura, C. B., Ismaila, N., Benson, A. B., 3rd, Carrato, A., Gulley, M. L., Jain, D., Kakar, S., Mackay, H. J., Streutker, C., Tang, L., Troxell, M., & Ajani, J. A. (2017). HER2 Testing and Clinical Decision Making in Gastroesophageal Adenocarcinoma: Guideline From the College of American Pathologists, American Society for Clinical Pathology, and the American Society of Clinical Oncology. *Journal of clinical oncology : official journal of the American Society of Clinical Oncology*, *35*(4), 446–464.

[3] Wolff, A. C., Hammond, M. E. H., Allison, K. H., Harvey, B. E., Mangu, P. B., Bartlett, J. M. S., Bilous, M., Ellis, I. O., Fitzgibbons, P., Hanna, W., Jenkins, R. B., Press, M. F., Spears, P. A., Vance, G. H., Viale, G., McShane, L. M., & Dowsett, M. (2018). Human Epidermal Growth Factor Receptor 2 Testing in Breast Cancer: American Society of Clinical Oncology/College of American Pathologists Clinical Practice Guideline Focused Update. *Journal of clinical oncology : official journal of the American Society of Clinical Oncology*, *36*(20), 2105–2122.

[4] Kunz, P. L., Mojtahed, A., Fisher, G. A., Ford, J. M., Chang, D. T., Balise, R. R., Bangs, C. D., Cherry, A. M., & Pai, R. K. (2012). HER2 expression in gastric and gastroesophageal junction adenocarcinoma in a US population: clinicopathologic analysis with proposed approach to HER2 assessment. *Applied immunohistochemistry & molecular morphology : AIMM*, *20*(1), 13–24.

[5] Slamon, D. J., Clark, G. M., Wong, S. G., Levin, W. J., Ullrich, A., & McGuire, W. L. (1987). Human breast cancer: correlation of relapse and survival with amplification of the HER-2/neu oncogene. *Science (New York, N.Y.)*, *235*(4785), 177–182.

[6] Bang Y. J. (2012). Advances in the management of HER2-positive advanced gastric and gastroesophageal junction cancer. *Journal of clinical gastroenterology*, *46*(8), 637–648.

[7] Morey, A. L., Brown, B., Farshid, G., Fox, S. B., Francis, G. D., McCue, G., von Neumann-Cosel, V., & Bilous, M. (2016). Determining HER2 (ERBB2) amplification status in women with breast cancer: final results from the Australian in situ hybridisation program. *Pathology*, *48*(6), 535–542.

[8] Van Cutsem, E., Bang, Y. J., Feng-Yi, F., Xu, J. M., Lee, K. W., Jiao, S. C., Chong, J. L., López-Sanchez, R. I., Price, T., Gladkov, O., Stoss, O., Hill, J., Ng, V., Lehle, M., Thomas, M., Kiermaier, A., & Rüschoff, J. (2015). HER2 screening data from ToGA: targeting HER2 in gastric and gastroesophageal junction cancer. *Gastric cancer : official journal of the International Gastric Cancer Association and the Japanese Gastric Cancer Association*, *18*(3), 476–484.

[9] Lei, Y. Y., Huang, J. Y., Zhao, Q. R., Jiang, N., Xu, H. M., Wang, Z. N., Li, H. Q., Zhang, S. B., & Sun, Z. (2017). The clinicopathological parameters and prognostic significance of HER2 expression in gastric cancer patients: a meta-analysis of literature. *World journal of surgical oncology*, *15*(1), 68.

[10] Yoon, J., Lee, S. H., Moon, S., Gebremedhn, H., Gebregiworgis, T., & Lee, K. Y. (2026). Integrative structural and dynamics studies of epidermal growth factor receptor (EGFR). Experimental & molecular medicine, 58(6), 1711–1720.

[11] Ogiso, H., Ishitani, R., Nureki, O., Fukai, S., Yamanaka, M., Kim, J. H., Saito, K., Sakamoto, A., Inoue, M., Shirouzu, M., & Yokoyama, S. (2002). Crystal structure of the complex of human epidermal growth factor and receptor extracellular domains. Cell, 110(6), 775–787.

[12] Cho, H. S., & Leahy, D. J. (2002). Structure of the extracellular region of HER3 reveals an interdomain tether. Science (New York, N.Y.), 297(5585), 1330–1333.

[13] Bouyain, S., Longo, P. A., Li, S., Ferguson, K. M., & Leahy, D. J. (2005). The extracellular region of ErbB4 adopts a tethered conformation in the absence of ligand. Proceedings of the National Academy of Sciences of the United States of America, 102(42), 15024–15029.

[14] Cho, H. S., Mason, K., Ramyar, K. X., Stanley, A. M., Gabelli, S. B., Denney, D. W., Jr, & Leahy, D. J. (2003). Structure of the extracellular region of HER2 alone and in complex with the Herceptin Fab. Nature, 421(6924), 756–760.

[15] Burgess, A.W., Garrett, T.P. (2008). EGFR Receptor Family Extracellular Domain Structures and Functions. In: Haley, J., Gullick, W. (eds) EGFR Signaling Networks in Cancer Therapy. Cancer Drug Discovery and Development. Humana Press.

[16] Ferguson, K. M., Berger, M. B., Mendrola, J. M., Cho, H. S., Leahy, D. J., & Lemmon, M. A. (2003). EGF activates its receptor by removing interactions that autoinhibit ectodomain dimerization. Molecular cell, 11(2), 507–517.

[17] Pinkas-Kramarski, R., Shelly, M., Guarino, B. C., Wang, L. M., Lyass, L., Alroy, I., Alimandi, M., Kuo, A., Moyer, J. D., Lavi, S., Eisenstein, M., Ratzkin, B. J., Seger, R., Bacus, S. S., Pierce, J. H., Andrews, G. C., & Yarden, Y. (1998). ErbB tyrosine kinases and the two neuregulin families constitute a ligand-receptor network. Molecular and cellular biology, 18(10), 6090–6101.

[18] Plowman, G. D., Culouscou, J. M., Whitney, G. S., Green, J. M., Carlton, G. W., Foy, L., Neubauer, M. G., & Shoyab, M. (1993). Ligand-specific activation of HER4/p180erbB4, a fourth member of the epidermal growth factor receptor family. Proceedings of the National Academy of Sciences of the United States of America, 90(5), 1746–1750.

[19] Riese, D. J., 2nd, & Stern, D. F. (1998). Specificity within the EGF family/ErbB receptor family signaling network. BioEssays : news and reviews in molecular, cellular and developmental biology, 20(1), 41–48.

[20] Qiu, C., Tarrant, M. K., Choi, S. H., Sathyamurthy, A., Bose, R., Banjade, S., Pal, A., Bornmann, W. G., Lemmon, M. A., Cole, P. A., & Leahy, D. J. (2008). Mechanism of activation and inhibition of the HER4/ErbB4 kinase. Structure (London, England : 1993), 16(3), 460–467.

[21] Diwanji, D., Trenker, R., Thaker, T. M., Wang, F., Agard, D. A., Verba, K. A., & Jura, N. (2021). Structures of the HER2-HER3-NRG1β complex reveal a dynamic dimer interface. Nature, 600(7888), 339–343.

[22] Bai, X., Sun, P., Wang, X., Long, C., Liao, S., Dang, S., Zhuang, S., Du, Y., Zhang, X., Li, N., He, K., & Zhang, Z. (2023). Structure and dynamics of the EGFR/HER2 heterodimer. Cell discovery, 9(1), 18.

[23] Tanner, K. G., & Kyte, J. (1999). Dimerization of the extracellular domain of the receptor for epidermal growth factor containing the membrane-spanning segment in response to treatment with epidermal growth factor. The Journal of biological chemistry, 274(50), 35985–35990.

[24] Bragin, P. E., Mineev, K. S., Bocharova, O. V., Volynsky, P. E., Bocharov, E. V., & Arseniev, A. S. (2016). HER2 Transmembrane Domain Dimerization Coupled with Self-Association of Membrane-Embedded Cytoplasmic Juxtamembrane Regions. Journal of molecular biology, 428(1), 52–61.

[25] Gullick, W. J., Bottomley, A. C., Lofts, F. J., Doak, D. G., Mulvey, D., Newman, R., Crumpton, M. J., Sternberg, M. J., & Campbell, I. D. (1992). Three dimensional structure of the transmembrane region of the proto-oncogenic and oncogenic forms of the neu protein. The EMBO journal, 11(1), 43–48.

[26] Bocharov, E. V., Mineev, K. S., Volynsky, P. E., Ermolyuk, Y. S., Tkach, E. N., Sobol, A. G., Chupin, V. V., Kirpichnikov, M. P., Efremov, R. G., & Arseniev, A. S. (2008). Spatial structure of the dimeric transmembrane domain of the growth factor receptor ErbB2 presumably corresponding to the receptor active state. The Journal of biological chemistry, 283(11), 6950–6956.

[27] Endres, N. F., Das, R., Smith, A. W., Arkhipov, A., Kovacs, E., Huang, Y., Pelton, J. G., Shan, Y., Shaw, D. E., Wemmer, D. E., Groves, J. T., & Kuriyan, J. (2013). Conformational coupling across the plasma membrane in activation of the EGF receptor. Cell, 152(3), 543–556.

[28] Matsushita, C., Tamagaki, H., Miyazawa, Y., Aimoto, S., Smith, S. O., & Sato, T. (2013). Transmembrane helix orientation influences membrane binding of the intracellular juxtamembrane domain in Neu receptor peptides. Proceedings of the National Academy of Sciences of the United States of America, 110(5), 1646–1651.

[29] Jura, N., Endres, N. F., Engel, K., Deindl, S., Das, R., Lamers, M. H., Wemmer, D. E., Zhang, X., & Kuriyan, J. (2009). Mechanism for activation of the EGF receptor catalytic domain by the juxtamembrane segment. Cell, 137(7), 1293–1307.

[30] Scheck, R. A., Lowder, M. A., Appelbaum, J. S., & Schepartz, A. (2012). Bipartite tetracysteine display reveals allosteric control of ligand-specific EGFR activation. ACS chemical biology, 7(8), 1367–1376.

[31] Arkhipov, A., Shan, Y., Das, R., Endres, N. F., Eastwood, M. P., Wemmer, D. E., Kuriyan, J., & Shaw, D. E. (2013). Architecture and membrane interactions of the EGF receptor. Cell, 152(3), 557–569.

[32] Pahuja, K. B., Nguyen, T. T., Jaiswal, B. S., Prabhash, K., Thaker, T. M., Senger, K., Chaudhuri, S., Kljavin, N. M., Antony, A., Phalke, S., Kumar, P., Mravic, M., Stawiski, E. W., Vargas, D., Durinck, S., Gupta, R., Khanna-Gupta, A., Trabucco, S. E., Sokol, E. S., Hartmaier, R. J., … Seshagiri, S. (2018). Actionable Activating Oncogenic ERBB2/HER2 Transmembrane and Juxtamembrane Domain Mutations. Cancer cell, 34(5), 792–806.e5.

[33] Zhang, X., Gureasko, J., Shen, K., Cole, P. A., & Kuriyan, J. (2006). An allosteric mechanism for activation of the kinase domain of epidermal growth factor receptor. Cell, 125(6), 1137–1149.

[34] Littlefield, P., Liu, L., Mysore, V., Shan, Y., Shaw, D. E., & Jura, N. (2014). Structural analysis of the EGFR/HER3 heterodimer reveals the molecular basis for activating HER3 mutations. Science signaling, 7(354), ra114.

[35] Jura, N., Shan, Y., Cao, X., Shaw, D. E., & Kuriyan, J. (2009). Structural analysis of the catalytically inactive kinase domain of the human EGF receptor 3. Proceedings of the National Academy of Sciences of the United States of America, 106(51), 21608–21613.

[36] Pinet, L., Wang, Y. H., Deville, C., Lescop, E., Guerlesquin, F., Badache, A., Bontems, F., Morellet, N., Durand, D., Assrir, N., & van Heijenoort, C. (2021). Structural and dynamic

characterization of the C-terminal tail of ErbB2: Disordered but not random. Biophysical journal, 120(10), 1869–1882.

[37] Bose, R., Molina, H., Patterson, A. S., Bitok, J. K., Periaswamy, B., Bader, J. S., Pandey, A., & Cole, P. A. (2006). Phosphoproteomic analysis of Her2/neu signaling and inhibition. Proceedings of the National Academy of Sciences of the United States of America, 103(26), 9773–9778.

[38] Kovacs, E., Zorn, J. A., Huang, Y., Barros, T., & Kuriyan, J. (2015). A structural perspective on the regulation of the epidermal growth factor receptor. Annual review of biochemistry, 84, 739–764.

[39] Lemmon, M. A., & Schlessinger, J. (2010). Cell signaling by receptor tyrosine kinases. Cell, 141(7), 1117–1134.

[40] Wallasch, C., Weiss, F. U., Niederfellner, G., Jallal, B., Issing, W., & Ullrich, A. (1995). Heregulin-dependent regulation of HER2/neu oncogenic signaling by heterodimerization with HER3. *The EMBO journal*, *14*(17), 4267–4275.

[41] Hellyer, N. J., Cheng, K., & Koland, J. G. (1998). ErbB3 (HER3) interaction with the p85 regulatory subunit of phosphoinositide 3-kinase. *The Biochemical journal*, *333 (Pt 3)*(Pt 3), 757–763.

[42] Junttila, T. T., Akita, R. W., Parsons, K., Fields, C., Lewis Phillips, G. D., Friedman, L. S., Sampath, D., & Sliwkowski, M. X. (2009). Ligand-independent HER2/HER3/PI3K complex is disrupted by trastuzumab and is effectively inhibited by the PI3K inhibitor GDC-0941. *Cancer cell*, *15*(5), 429–440.

[43] Hellyer, N. J., Kim, M. S., & Koland, J. G. (2001). Heregulin-dependent activation of phosphoinositide 3-kinase and Akt via the ErbB2/ErbB3 co-receptor. *The Journal of biological chemistry*, *276*(45), 42153–42161.

[44] Soltoff, S. P., Carraway, K. L., 3rd, Prigent, S. A., Gullick, W. G., & Cantley, L. C. (1994). ErbB3 is involved in activation of phosphatidylinositol 3-kinase by epidermal growth factor. *Molecular and cellular biology*, *14*(6), 3550–3558.

[45] Smirnova, T., Zhou, Z. N., Flinn, R. J., Wyckoff, J., Boimel, P. J., Pozzuto, M., Coniglio, S. J., Backer, J. M., Bresnick, A. R., Condeelis, J. S., Hynes, N. E., & Segall, J. E. (2012). Phosphoinositide 3-kinase signaling is critical for ErbB3-driven breast cancer cell motility and metastasis. *Oncogene*, *31*(6), 706–715.

[46] Ruiz-Saenz, A., Dreyer, C., Campbell, M. R., Steri, V., Gulizia, N., & Moasser, M. M. (2018). HER2 Amplification in Tumors Activates PI3K/Akt Signaling Independent of HER3. *Cancer research*, *78*(13), 3645–3658.

[47] Alessi, D. R., Deak, M., Casamayor, A., Caudwell, F. B., Morrice, N., Norman, D. G., Gaffney, P., Reese, C. B., MacDougall, C. N., Harbison, D., Ashworth, A., & Bownes, M. (1997). 3-Phosphoinositide-dependent protein kinase-1 (PDK1): structural and functional homology with the Drosophila DSTPK61 kinase. *Current biology : CB*, *7*(10), 776–789.

[48] Sarbassov, D. D., Guertin, D. A., Ali, S. M., & Sabatini, D. M. (2005). Phosphorylation and regulation of Akt/PKB by the rictor-mTOR complex. *Science (New York, N.Y.)*, *307*(5712), 1098–1101.

[49] Holbro, T., Beerli, R. R., Maurer, F., Koziczak, M., Barbas, C. F., 3rd, & Hynes, N. E. (2003). The ErbB2/ErbB3 heterodimer functions as an oncogenic unit: ErbB2 requires ErbB3 to drive breast tumor cell proliferation. *Proceedings of the National Academy of Sciences of the United States of America*, *100*(15), 8933–8938.

[50] Maehama, T., & Dixon, J. E. (1998). The tumor suppressor, PTEN/MMAC1, dephosphorylates the lipid second messenger, phosphatidylinositol 3,4,5-trisphosphate. *The Journal of biological chemistry*, *273*(22), 13375–13378.

[51] Saal, L. H., Holm, K., Maurer, M., Memeo, L., Su, T., Wang, X., Yu, J. S., Malmström, P. O., Mansukhani, M., Enoksson, J., Hibshoosh, H., Borg, A., & Parsons, R. (2005). PIK3CA mutations correlate with hormone receptors, node metastasis, and ERBB2, and are mutually exclusive with PTEN loss in human breast carcinoma. *Cancer research*, *65*(7), 2554–2559.

[52] Cheng, H., Liu, P., Ohlson, C., Xu, E., Symonds, L., Isabella, A., Muller, W. J., Lin, N. U., Krop, I. E., Roberts, T. M., Winer, E. P., Arteaga, C. L., & Zhao, J. J. (2016). PIK3CA(H1047R)- and Her2-initiated mammary tumors escape PI3K dependency by compensatory activation of MEK-ERK signaling. *Oncogene*, *35*(23), 2961–2970.

[53] Schulze, W. X., Deng, L., & Mann, M. (2005). Phosphotyrosine interactome of the ErbB-receptor kinase family. *Molecular systems biology*, *1*, 2005.0008.

[54] Batzer, A. G., Rotin, D., Ureña, J. M., Skolnik, E. Y., & Schlessinger, J. (1994). Hierarchy of binding sites for Grb2 and Shc on the epidermal growth factor receptor. *Molecular and cellular biology*, *14*(8), 5192–5201.

[55] Serra, V., Scaltriti, M., Prudkin, L., Eichhorn, P. J., Ibrahim, Y. H., Chandarlapaty, S., Markman, B., Rodriguez, O., Guzman, M., Rodriguez, S., Gili, M., Russillo, M., Parra, J. L., Singh, S., Arribas, J., Rosen, N., & Baselga, J. (2011). PI3K inhibition results in enhanced HER signaling and acquired ERK dependency in HER2-overexpressing breast cancer. *Oncogene*, *30*(22), 2547–2557.

[56] Smith, A. E., Ferraro, E., Safonov, A., Morales, C. B., Lahuerta, E. J. A., Li, Q., Kulick, A., Ross, D., Solit, D. B., de Stanchina, E., Reis-Filho, J., Rosen, N., Arribas, J., Razavi, P., & Chandarlapaty, S. (2021). HER2 + breast cancers evade anti-HER2 therapy via a switch in driver pathway. *Nature communications*, *12*(1), 6667.

[57] Matkar, S., An, C., & Hua, X. (2017). Kinase inhibitors of HER2/AKT pathway induce ERK phosphorylation via a FOXO-dependent feedback loop. *American journal of cancer research*, *7*(7), 1476–1485.

[58] Balz, L. M., Bartkowiak, K., Andreas, A., Pantel, K., Niggemann, B., Zänker, K. S., Brandt, B. H., & Dittmar, T. (2012). The interplay of HER2/HER3/PI3K and EGFR/HER2/PLC-γ1 signalling in breast cancer cell migration and dissemination. *The Journal of pathology*, *227*(2), 234–244.

[59] Hartman, Z. C., Yang, X. Y., Glass, O., Lei, G., Osada, T., Dave, S. S., Morse, M. A., Clay, T. M., & Lyerly, H. K. (2011). HER2 overexpression elicits a proinflammatory IL-6 autocrine signaling loop that is critical for tumorigenesis. *Cancer research*, *71*(13), 4380–4391.

[60] Rodriguez-Barrueco, R., Yu, J., Saucedo-Cuevas, L. P., Olivan, M., Llobet-Navas, D., Putcha, P., Castro, V., Murga-Penas, E. M., Collazo-Lorduy, A., Castillo-Martin, M., Alvarez, M., Cordon-Cardo, C., Kalinsky, K., Maurer, M., Califano, A., & Silva, J. M. (2015). Inhibition of the autocrine IL-6-JAK2-STAT3-calprotectin axis as targeted therapy for HR-/HER2+ breast cancers. *Genes & development*, *29*(15), 1631–1648.

[61] Chung, S. S., Giehl, N., Wu, Y., & Vadgama, J. V. (2014). STAT3 activation in HER2-overexpressing breast cancer promotes epithelial-mesenchymal transition and cancer stem cell traits. *International journal of oncology*, *44*(2), 403–411.

[62] Sonnenblick, A., Brohée, S., Fumagalli, D., Vincent, D., Venet, D., Ignatiadis, M., Salgado, R., Van den Eynden, G., Rothé, F., Desmedt, C., Neven, P., Loibl, S., Denkert, C., Joensuu,

H., Loi, S., Sirtaine, N., Kellokumpu-Lehtinen, P. L., Piccart, M., & Sotiriou, C. (2015). Constitutive phosphorylated STAT3-associated gene signature is predictive for trastuzumab resistance in primary HER2-positive breast cancer. *BMC medicine*, *13*, 177.

[63] Benlimame, N., He, Q., Jie, S., Xiao, D., Xu, Y. J., Loignon, M., Schlaepfer, D. D., & Alaoui-Jamali, M. A. (2005). FAK signaling is critical for ErbB-2/ErbB-3 receptor cooperation for oncogenic transformation and invasion. *The Journal of cell biology*, *171*(3), 505–516.

[64] Xu, Y., Benlimame, N., Su, J., He, Q., & Alaoui-Jamali, M. A. (2009). Regulation of focal adhesion turnover by ErbB signalling in invasive breast cancer cells. *British journal of cancer*, *100*(4), 633–643.

[65] Wang, S. E., Xiang, B., Zent, R., Quaranta, V., Pozzi, A., & Arteaga, C. L. (2009). Transforming growth factor beta induces clustering of HER2 and integrins by activating Src-focal adhesion kinase and receptor association to the cytoskeleton. *Cancer research*, *69*(2), 475–482.

[66] Lazaro, G., Smith, C., Goddard, L., Jordan, N., McClelland, R., Barrett-Lee, P., Nicholson, R. I., & Hiscox, S. (2013). Targeting focal adhesion kinase in ER+/HER2+ breast cancer improves trastuzumab response. *Endocrine-related cancer*, *20*(5), 691–704.

[67] Yakes, F. M., Chinratanalab, W., Ritter, C. A., King, W., Seelig, S., & Arteaga, C. L. (2002). Herceptin-induced inhibition of phosphatidylinositol-3 kinase and Akt Is required for antibody-mediated effects on p27, cyclin D1, and antitumor action. *Cancer research*, *62*(14), 4132-4141.

[68] Nagata, Y., Lan, K. H., Zhou, X., Tan, M., Esteva, F. J., Sahin, A. A., Klos, K. S., Li, P., Monia, B. P., Nguyen, N. T., Hortobagyi, G. N., Hung, M. C., & Yu, D. (2004). PTEN activation contributes to tumor inhibition by trastuzumab, and loss of PTEN predicts trastuzumab resistance in patients. *Cancer cell*, *6*(2), 117-127.

[69] Vacca, S., Gragera, M., Buschiazzo, A., Herreros, D., Krieger, J. M., Bonn-Garcia, S., Melero, R., Sorzano, C. O., Carazo, J. M., Medalia, O., & Plückthun, A. (2025). Structural analysis of HER2-trastuzumab complex reveals receptor conformational adaptation. *Science advances*, *11*(30), eadu9945.

[70] Arnould, L., Gelly, M., Penault-Llorca, F., Benoit, L., Bonnetain, F., Migeon, C., Cabaret, V., Fermeaux, V., Bertheau, P., Garnier, J., Jeannin, J. F., & Coudert, B. (2006). Trastuzumab-based treatment of HER2-positive breast cancer: an antibody-dependent cellular cytotoxicity mechanism?. *British journal of cancer*, *94*(2), 259-267.

[71] Shi, Y., Fan, X., Deng, H., Brezski, R. J., Rycyzyn, M., Jordan, R. E., Strohl, W. R., Zou, Q., Zhang, N., & An, Z. (2015). Trastuzumab triggers phagocytic killing of high HER2 cancer cells in vitro and in vivo by interaction with Fcγ receptors on macrophages. *Journal of immunology (Baltimore, Md. : 1950)*, *194*(9), 4379-4386.

[72] Molina, M. A., Codony-Servat, J., Albanell, J., Rojo, F., Arribas, J., & Baselga, J. (2001). Trastuzumab (herceptin), a humanized anti-Her2 receptor monoclonal antibody, inhibits basal and activated Her2 ectodomain cleavage in breast cancer cells. *Cancer research*, *61*(12), 4744-4749.

[73] Lange, T., Nentwich, M. F., Lüth, M., Yekebas, E., & Schumacher, U. (2011). Trastuzumab has anti-metastatic and anti-angiogenic activity in a spontaneous metastasis xenograft model of esophageal adenocarcinoma. *Cancer letters*, *308*(1), 54-61.

[74] Nami, B., Maadi, H., & Wang, Z. (2018). Mechanisms Underlying the Action and Synergism of Trastuzumab and Pertuzumab in Targeting HER2-Positive Breast Cancer. *Cancers*, *10*(10), 342.

[75] Phillips, G. D., Fields, C. T., Li, G., Dowbenko, D., Schaefer, G., Miller, K., Andre, F., Burris, H. A., 3rd, Albain, K. S., Harbeck, N., Dieras, V., Crivellari, D., Fang, L., Guardino, E., Olsen, S. R., Crocker, L. M., & Sliwkowski, M. X. (2014). Dual targeting of HER2-positive cancer with trastuzumab emtansine and pertuzumab: critical role for neuregulin blockade in antitumor response to combination therapy. Clinical cancer research : an official journal of the American Association for Cancer Research, 20(2), 456-468.

[76] Swain, S. M., Miles, D., Kim, S. B., Im, Y. H., Im, S. A., Semiglazov, V., Ciruelos, E., Schneeweiss, A., Loi, S., Monturus, E., Clark, E., Knott, A., Restuccia, E., Benyunes, M. C., Cortés, J., & CLEOPATRA study group (2020). Pertuzumab, trastuzumab, and docetaxel for HER2-positive metastatic breast cancer (CLEOPATRA): end-of-study results from a double-blind, randomised, placebo-controlled, phase 3 study. *The Lancet. Oncology*, *21*(4), 519-530.

[77] Stavenhagen, J. B., Gorlatov, S., Tuaillon, N., Rankin, C. T., Li, H., Burke, S., Huang, L., Vijh, S., Johnson, S., Bonvini, E., & Koenig, S. (2007). Fc optimization of therapeutic antibodies enhances their ability to kill tumor cells in vitro and controls tumor expansion in vivo via low-affinity activating Fcgamma receptors. *Cancer research*, *67*(18), 8882-8890.

[78] Rugo, H. S., Im, S. A., Cardoso, F., Cortés, J., Curigliano, G., Musolino, A., Pegram, M. D., Wright, G. S., Saura, C., Escrivá-de-Romaní, S., De Laurentiis, M., Levy, C., Brown-Glaberman, U., Ferrero, J. M., de Boer, M., Kim, S. B., Petráková, K., Yardley, D. A., Freedman, O., Jakobsen, E. H., … SOPHIA Study Group (2021). Efficacy of Margetuximab vs Trastuzumab in Patients With Pretreated ERBB2-Positive Advanced Breast Cancer: A Phase 3 Randomized Clinical Trial. *JAMA oncology*, *7*(4), 573-584.

[79] Rugo, H. S., Im, S. A., Cardoso, F., Cortes, J., Curigliano, G., Musolino, A., Pegram, M. D., Bachelot, T., Wright, G. S., Saura, C., Escrivá-de-Romaní, S., De Laurentiis, M., Schwartz, G. N., Pluard, T. J., Ricci, F., Gwin, W. R., 3rd, Levy, C., Brown-Glaberman, U., Ferrero, J. M., de Boer, M., … SOPHIA Study Group (2023). Margetuximab Versus Trastuzumab in Patients With Previously Treated HER2-Positive Advanced Breast Cancer (SOPHIA): Final Overall Survival Results From a Randomized Phase 3 Trial. *Journal of clinical oncology : official journal of the American Society of Clinical Oncology*, *41*(2), 198-205.

[80] Lambert, J. M., & Chari, R. V. (2014). Ado-trastuzumab Emtansine (T-DM1): an antibody-drug conjugate (ADC) for HER2-positive breast cancer. *Journal of medicinal chemistry*, *57*(16), 6949-6964.

[81] Hamblett, K. J., Jacob, A. P., Gurgel, J. L., Tometsko, M. E., Rock, B. M., Patel, S. K., Milburn, R. R., Siu, S., Ragan, S. P., Rock, D. A., Borths, C. J., O'Neill, J. W., Chang, W. S., Weidner, M. F., Bio, M. M., Quon, K. C., & Fanslow, W. C. (2015). SLC46A3 Is Required to Transport Catabolites of Noncleavable Antibody Maytansine Conjugates from the Lysosome to the Cytoplasm. *Cancer research*, *75*(24), 5329-5340.

[82] Erickson, H. K., Park, P. U., Widdison, W. C., Kovtun, Y. V., Garrett, L. M., Hoffman, K., Lutz, R. J., Goldmacher, V. S., & Blättler, W. A. (2006). Antibody-maytansinoid conjugates are activated in targeted cancer cells by lysosomal degradation and linker-dependent intracellular processing. *Cancer research*, *66*(8), 4426-4433.

[83] Lewis Phillips, G. D., Li, G., Dugger, D. L., Crocker, L. M., Parsons, K. L., Mai, E., Blättler, W. A., Lambert, J. M., Chari, R. V., Lutz, R. J., Wong, W. L., Jacobson, F. S., Koeppen, H.,

Schwall, R. H., Kenkare-Mitra, S. R., Spencer, S. D., & Sliwkowski, M. X. (2008). Targeting HER2-positive breast cancer with trastuzumab-DM1, an antibody-cytotoxic drug conjugate. *Cancer research*, *68*(22), 9280-9290.

[84] Diéras, V., Miles, D., Verma, S., Pegram, M., Welslau, M., Baselga, J., Krop, I. E., Blackwell, K., Hoersch, S., Xu, J., Green, M., & Gianni, L. (2017). Trastuzumab emtansine versus capecitabine plus lapatinib in patients with previously treated HER2-positive advanced breast cancer (EMILIA): a descriptive analysis of final overall survival results from a randomised, open-label, phase 3 trial. *The Lancet. Oncology*, *18*(6), 732-742.

[85] Nakada, T., Masuda, T., Naito, H., Yoshida, M., Ashida, S., Morita, K., Miyazaki, H., Kasuya, Y., Ogitani, Y., Yamaguchi, J., Abe, Y., & Honda, T. (2016). Novel antibody drug conjugates containing exatecan derivative-based cytotoxic payloads. *Bioorganic & medicinal chemistry letters*, *26*(6), 1542-1545.

[86] Pommier Y. (2006). Topoisomerase I inhibitors: camptothecins and beyond. *Nature reviews. Cancer*, *6*(10), 789-802.

[87] Nakada, T., Sugihara, K., Jikoh, T., Abe, Y., & Agatsuma, T. (2019). The Latest Research and Development into the Antibody-Drug Conjugate, [fam-] Trastuzumab Deruxtecan (DS-8201a), for HER2 Cancer Therapy. *Chemical & pharmaceutical bulletin*, *67*(3), 173-185.

[88] Ogitani, Y., Hagihara, K., Oitate, M., Naito, H., & Agatsuma, T. (2016). Bystander killing effect of DS-8201a, a novel anti-human epidermal growth factor receptor 2 antibody-drug conjugate, in tumors with human epidermal growth factor receptor 2 heterogeneity. *Cancer science*, *107*(7), 1039-1046.

[89] van der Lee, M. M., Groothuis, P. G., Ubink, R., van der Vleuten, M. A., van Achterberg, T. A., Loosveld, E. M., Damming, D., Jacobs, D. C., Rouwette, M., Egging, D. F., van den Dobbelsteen, D., Beusker, P. H., Goedings, P., Verheijden, G. F., Lemmens, J. M., Timmers, M., & Dokter, W. H. (2015). The Preclinical Profile of the Duocarmycin-Based HER2-Targeting ADC SYD985 Predicts for Clinical Benefit in Low HER2-Expressing Breast Cancers. *Molecular cancer therapeutics*, *14*(3), 692-703.

[90] Cortés, J., Hurvitz, S. A., Im, S. A., Iwata, H., Curigliano, G., Kim, S. B., Chiu, J. W. Y., Pedrini, J. L., Li, W., Yonemori, K., Bianchini, G., Loi, S., Borges, G. S., Wang, X., Bachelot, T., Nakatani, S., Ashfaque, S., Liang, Z., Egorov, A., & Hamilton, E. (2024). Trastuzumab deruxtecan versus trastuzumab emtansine in HER2-positive metastatic breast cancer: long-term survival analysis of the DESTINY-Breast03 trial. *Nature medicine*, *30*(8), 2208-2215.

[91] Tolaney, S. M., Jiang, Z., Zhang, Q., Barroso-Sousa, R., Park, Y. H., Rimawi, M. F., Saura, C., Schneeweiss, A., Toi, M., Chae, Y. S., Kemal, Y., Chaudhari, M., Şendur, M. A. N., Yamashita, T., Casalnuovo, M., Danso, M. A., Liu, J., Shetty, J., Herbolsheimer, P., Loibl, S., … DESTINY-Breast09 Trial Investigators (2026). Trastuzumab Deruxtecan plus Pertuzumab for HER2-Positive Metastatic Breast Cancer. *The New England journal of medicine*, *394*(6), 551-562.

[92] U.S. Food and Drug Administration. (2025, December 15). FDA approves fam-trastuzumab deruxtecan-nxki with pertuzumab for unresectable or metastatic HER2-positive breast cancer.

[93] Meric-Bernstam, F., Makker, V., Oaknin, A., Oh, D. Y., Banerjee, S., González-Martín, A., Jung, K. H., Ługowska, I., Manso, L., Manzano, A., Melichar, B., Siena, S., Stroyakovskiy, D., Fielding, A., Ma, Y., Puvvada, S., Shire, N., & Lee, J. Y. (2024). Efficacy and Safety of

Trastuzumab Deruxtecan in Patients With HER2-Expressing Solid Tumors: Primary Results From the DESTINY-PanTumor02 Phase II Trial. *Journal of clinical oncology : official journal of the American Society of Clinical Oncology*, *42*(1), 47-58.

[94] Smit, E. F., Felip, E., Uprety, D., Nagasaka, M., Nakagawa, K., Paz-Ares Rodríguez, L., Pacheco, J. M., Li, B. T., Planchard, D., Baik, C., Goto, Y., Murakami, H., Saltos, A., Pereira, K., Taguchi, A., Cheng, Y., Yan, Q., Feng, W., Tsuchihashi, Z., & Jänne, P. A. (2024). Trastuzumab deruxtecan in patients with metastatic non-small-cell lung cancer (DESTINY-Lung01): primary results of the HER2-overexpressing cohorts from a single-arm, phase 2 trial. *The Lancet. Oncology*, *25*(4), 439-454.

[95] Raghav, K., Siena, S., Takashima, A., Kato, T., Van den Eynde, M., Pietrantonio, F., Komatsu, Y., Kawakami, H., Peeters, M., Andre, T., Lonardi, S., Yamaguchi, K., Tie, J., Castro, C. G., Hsu, H. C., Strickler, J. H., Kim, T. Y., Cha, Y., Barrios, D., Yan, Q., … Yoshino, T. (2024). Trastuzumab deruxtecan in patients with HER2-positive advanced colorectal cancer (DESTINY-CRC02): primary results from a multicentre, randomised, phase 2 trial. *The Lancet. Oncology*, *25*(9), 1147-1162.

[96] Wood, E. R., Truesdale, A. T., McDonald, O. B., Yuan, D., Hassell, A., Dickerson, S. H., Ellis, B., Pennisi, C., Horne, E., Lackey, K., Alligood, K. J., Rusnak, D. W., Gilmer, T. M., & Shewchuk, L. (2004). A unique structure for epidermal growth factor receptor bound to GW572016 (Lapatinib): relationships among protein conformation, inhibitor off-rate, and receptor activity in tumor cells. *Cancer research*, *64*(18), 6652-6659.

[97] Xia, W., Mullin, R. J., Keith, B. R., Liu, L. H., Ma, H., Rusnak, D. W., Owens, G., Alligood, K. J., & Spector, N. L. (2002). Anti-tumor activity of GW572016: a dual tyrosine kinase inhibitor blocks EGF activation of EGFR/erbB2 and downstream Erk1/2 and AKT pathways. Oncogene, 21(41), 6255-6263.

[98] Geyer, C. E., Forster, J., Lindquist, D., Chan, S., Romieu, C. G., Pienkowski, T., Jagiello-Gruszfeld, A., Crown, J., Chan, A., Kaufman, B., Skarlos, D., Campone, M., Davidson, N., Berger, M., Oliva, C., Rubin, S. D., Stein, S., & Cameron, D. (2006). Lapatinib plus capecitabine for HER2-positive advanced breast cancer. *The New England journal of medicine*, *355*(26), 2733-2743.

[99] Rabindran, S. K., Discafani, C. M., Rosfjord, E. C., Baxter, M., Floyd, M. B., Golas, J., Hallett, W. A., Johnson, B. D., Nilakantan, R., Overbeek, E., Reich, M. F., Shen, R., Shi, X., Tsou, H. R., Wang, Y. F., & Wissner, A. (2004). Antitumor activity of HKI-272, an orally active, irreversible inhibitor of the HER-2 tyrosine kinase. *Cancer research*, *64*(11), 3958-3965.

[100] Martin, M., Holmes, F. A., Ejlertsen, B., Delaloge, S., Moy, B., Iwata, H., von Minckwitz, G., Chia, S. K. L., Mansi, J., Barrios, C. H., Gnant, M., Tomašević, Z., Denduluri, N., Šeparović, R., Gokmen, E., Bashford, A., Ruiz Borrego, M., Kim, S. B., Jakobsen, E. H., Ciceniene, A., … ExteNET Study Group (2017). Neratinib after trastuzumab-based adjuvant therapy in HER2-positive breast cancer (ExteNET): 5-year analysis of a randomised, double-blind, placebo-controlled, phase 3 trial. *The Lancet. Oncology*, *18*(12), 1688-1700.

[101] Lacouture M. E. (2006). Mechanisms of cutaneous toxicities to EGFR inhibitors. *Nature reviews. Cancer*, *6*(10), 803-812.

[102] Ariyadamrongkwan, J., & Muanprasat, C. (2025). Pathophysiological mechanisms underlying diarrhea across generations of EGFR-TKIs: The role of ERBB signaling and

potential therapies. *Biomedicine & pharmacotherapy = Biomedecine & pharmacotherapie*, *192*, 118562.

[103]Chan, A., Ruiz-Borrego, M., Marx, G., Chien, A. J., Rugo, H. S., Brufsky, A., Thirlwell, M., Trudeau, M., Bose, R., García-Sáenz, J. A., Egle, D., Pistilli, B., Wassermann, J., Cheong, K. A., Schnappauf, B., Semsek, D., Singer, C. F., Foruzan, N., DiPrimeo, D., McCulloch, L., … Barcenas, C. H. (2023). Final findings from the CONTROL trial: Strategies to reduce the incidence and severity of neratinib-associated diarrhea in patients with HER2-positive early-stage breast cancer. *Breast (Edinburgh, Scotland)*, *67*, 94-101.

[104]Kulukian, A., Lee, P., Taylor, J., Rosler, R., de Vries, P., Watson, D., Forero-Torres, A., & Peterson, S. (2020). Preclinical Activity of HER2-Selective Tyrosine Kinase Inhibitor Tucatinib as a Single Agent or in Combination with Trastuzumab or Docetaxel in Solid Tumor Models. *Molecular cancer therapeutics*, *19*(4), 976-987.

[105]O'Brien, N. A., Huang, H. K. T., McDermott, M. S. J., Madrid, A. M., Luo, T., Ayala, R., Issakhanian, S., Gong, K. W., Lu, M., Zhang, J., & Slamon, D. J. (2022). Tucatinib has Selective Activity in HER2-Positive Cancers and Significant Combined Activity with Approved and Novel Breast Cancer-Targeted Therapies. *Molecular cancer therapeutics*, *21*(5), 751-761.

[106]Murthy, R. K., Loi, S., Okines, A., Paplomata, E., Hamilton, E., Hurvitz, S. A., Lin, N. U., Borges, V., Abramson, V., Anders, C., Bedard, P. L., Oliveira, M., Jakobsen, E., Bachelot, T., Shachar, S. S., Müller, V., Braga, S., Duhoux, F. P., Greil, R., Cameron, D., … Winer, E. P. (2020). Tucatinib, Trastuzumab, and Capecitabine for HER2-Positive Metastatic Breast Cancer. *The New England journal of medicine*, *382*(7), 597-609.

[107]Curigliano, G., Mueller, V., Borges, V., Hamilton, E., Hurvitz, S., Loi, S., Murthy, R., Okines, A., Paplomata, E., Cameron, D., Carey, L. A., Gelmon, K., Hortobagyi, G. N., Krop, I., Loibl, S., Pegram, M., Slamon, D., Ramos, J., Feng, W., & Winer, E. (2022). Tucatinib versus placebo added to trastuzumab and capecitabine for patients with pretreated HER2+ metastatic breast cancer with and without brain metastases (HER2CLIMB): final overall survival analysis. *Annals of oncology : official journal of the European Society for Medical Oncology*, *33*(3), 321-329.

[108]Lin, N. U., Borges, V., Anders, C., Murthy, R. K., Paplomata, E., Hamilton, E., Hurvitz, S., Loi, S., Okines, A., Abramson, V., Bedard, P. L., Oliveira, M., Mueller, V., Zelnak, A., DiGiovanna, M. P., Bachelot, T., Chien, A. J., O'Regan, R., Wardley, A., Conlin, A., … Winer, E. P. (2020). Intracranial Efficacy and Survival With Tucatinib Plus Trastuzumab and Capecitabine for Previously Treated HER2-Positive Breast Cancer With Brain Metastases in the HER2CLIMB Trial. *Journal of clinical oncology : official journal of the American Society of Clinical Oncology*, *38*(23), 2610-2619.

[109]Shah, M., Wedam, S., Cheng, J., Fiero, M. H., Xia, H., Li, F., Fan, J., Zhang, X., Yu, J., Song, P., Chen, W., Ricks, T. K., Chen, X. H., Goldberg, K. B., Gong, Y., Pierce, W. F., Tang, S., Theoret, M. R., Pazdur, R., Amiri-Kordestani, L., … Beaver, J. A. (2021). FDA Approval Summary: Tucatinib for the Treatment of Patients with Advanced or Metastatic HER2-positive Breast Cancer. *Clinical cancer research : an official journal of the American Association for Cancer Research*, *27*(5), 1220-1226.

[110]Wilding, B., Woelflingseder, L., Baum, A., Chylinski, K., Vainorius, G., Gibson, N., Waizenegger, I. C., Gerlach, D., Augsten, M., Spreitzer, F., Shirai, Y., Ikegami, M., Tilandyová, S., Scharn, D., Pearson, M. A., Popow, J., Obenauf, A. C., Yamamoto, N., Kondo, S., Opdam, F. L., … Neumüller, R. A. (2025). Zongertinib (BI 1810631), an

Irreversible HER2 TKI, Spares EGFR Signaling and Improves Therapeutic Response in Preclinical Models and Patients with HER2-Driven Cancers. *Cancer discovery*, *15*(1), 119-138.

[111]Heymach, J. V., Opdam, F., Barve, M., Tu, H. Y., Wu, Y. L., Berz, D., Schröter, L., Botilde, Y., Sadrolhefazi, B., Serra, J., Yoh, K., & Yamamoto, N. (2025). HER2-Selective Tyrosine Kinase Inhibitor, Zongertinib (BI 1810631), in Patients With Advanced/Metastatic Solid Tumors With *HER2* Alterations: A Phase Ia Dose-Escalation Study. *Journal of clinical oncology : official journal of the American Society of Clinical Oncology*, *43*(11), 1337-1347.

[112]Heymach, J. V., Ruiter, G., Ahn, M. J., Girard, N., Smit, E. F., Planchard, D., Wu, Y. L., Cho, B. C., Yamamoto, N., Sabari, J. K., Zhao, Y., Tu, H. Y., Yoh, K., Nadal, E., Sadrolhefazi, B., Rohrbacher, M., von Wangenheim, U., Eigenbrod-Giese, S., Zugazagoitia, J., & Beamion LUNG-1 Investigators (2025). Zongertinib in Previously Treated *HER2*-Mutant Non-Small-Cell Lung Cancer. *The New England journal of medicine*, *392*(23), 2321-2333.

[113]U.S. Food and Drug Administration. (2025, August 8). FDA grants accelerated approval to zongertinib for non-squamous NSCLC with HER2 TKD activating mutations.

[114]Heymach, J. V., Yamamoto, N., Girard, N., Ruiter, G., Smit, E. F., Planchard, D., Nadal, E., Wu, Y. L., Zugazagoitia, J., Tu, H. Y., Baik, C. S., Yoh, K., Soo, R. A., Zhao, Y., Sabari, J. K., Wermke, M., Scheffler, M., Ahn, M. J., Fernamberg, K., Schroeter, L., … Beamion LUNG-1 Investigators (2026). First-Line Zongertinib in Advanced *HER2*-Mutant Non-Small-Cell Lung Cancer. *The New England journal of medicine*, *394*(17), 1675-1684.

[115]U.S. Food and Drug Administration. (2026, February 26). FDA grants accelerated approval to zongertinib for unresectable or metastatic non-squamous non-small cell lung cancer.

[116]Lei, Z., Chen, B., Koo, Y. M., & MacFarlane, D. R. (2017). Introduction: ionic liquids. *Chemical reviews*, *117*(10), 6633-6635.

[117]Shi, R., & Wang, Y. (2016). Dual ionic and organic nature of ionic liquids. *Scientific Reports*, *6*(1), 19644.

[118]Silva, W., Zanatta, M., Ferreira, A. S., Corvo, M. C., & Cabrita, E. J. (2020). Revisiting ionic liquid structure-property relationship: A critical analysis. *International journal of molecular sciences*, *21*(20), 7745.

[119]Hayes, R., Warr, G. G., & Atkin, R. (2015). Structure and nanostructure in ionic liquids. *Chemical reviews*, *115*(13), 6357-6426.

[120]Rooney, D., Jacquemin, J., & Gardas, R. (2009). Thermophysical properties of ionic liquids. *Ionic liquids*, 185-212.

[121]Lobo Ferreira, A. I., Rodrigues, A. S., Villas, M., Tojo, E., Rebelo, L. P. N., & Santos, L. M. (2019). Crystallization and glass-forming ability of ionic liquids: novel insights into their thermal behavior. *ACS Sustainable Chemistry & Engineering*, *7*(3), 2989-2997.

[122]Greaves, T. L., & Drummond, C. J. (2015). Protic ionic liquids: evolving structure–property relationships and expanding applications. *Chemical reviews*, *115*(20), 11379-11448.

[123]Hunt, P. A., Ashworth, C. R., & Matthews, R. P. (2015). Hydrogen bonding in ionic liquids. *Chemical Society Reviews*, *44*(5), 1257-1288.

[124]Ab Rani, M. A., Brant, A., Crowhurst, L., Dolan, A., Lui, M., Hassan, N. H., ... & Wilding, R. (2011). Understanding the polarity of ionic liquids. *Physical Chemistry Chemical Physics*, *13*(37), 16831-16840.

[125]Kaur, G., Kumar, H., & Singla, M. (2022). Diverse applications of ionic liquids: A comprehensive review. *Journal of Molecular Liquids*, *351*, 118556.

[126]Plechkova, N. V., & Seddon, K. R. (2007). Applications of ionic liquids in the chemical industry. *Chemical Society Reviews*, *37*(1), 123-150.

[127]Al-Bodour, A., Alomari, N., Perez-Duran, G., Rozas, S., Iglesias-Silva, G., Aparicio, S., ... & Atilhan, M. (2025). Ionic liquids as multidimensional materials: A review from fundamentals to applications. *Energy & Fuels*, *39*(27), 12791-12829.

[128]Tokuda, H., Hayamizu, K., Ishii, K., Susan, M. A. B. H., & Watanabe, M. (2004). Physicochemical properties and structures of room temperature ionic liquids. 1. Variation of anionic species. *The Journal of Physical Chemistry B*, *108*(42), 16593-16600.

[129]Tokuda, H., Hayamizu, K., Ishii, K., Susan, M. A. B. H., & Watanabe, M. (2005). Physicochemical properties and structures of room temperature ionic liquids. 2. Variation of alkyl chain length in imidazolium cation. *The Journal of Physical Chemistry B*, *109*(13), 6103-6110.

[130]Tokuda, H., Ishii, K., Susan, M. A. B. H., Tsuzuki, S., Hayamizu, K., & Watanabe, M. (2006). Physicochemical properties and structures of room-temperature ionic liquids. 3. Variation of cationic structures. *The Journal of Physical Chemistry B*, *110*(6), 2833-2839.

[131]Wang, Y., & Voth, G. A. (2005). Unique spatial heterogeneity in ionic liquids. *Journal of the American Chemical Society*, *127*(35), 12192-12193.

[132]Triolo, A., Russina, O., Bleif, H. J., & Di Cola, E. (2007). Nanoscale segregation in room temperature ionic liquids. *The Journal of Physical Chemistry B*, *111*(18), 4641-4644.

[133]Canongia Lopes, J. N., & Pádua, A. A. (2006). Nanostructural organization in ionic liquids. *The Journal of Physical Chemistry B*, *110*(7), 3330-3335.

[134]Silva, A. T., Teixeira, C., Marques, E. F., Prudêncio, C., Gomes, P., & Ferraz, R. (2021). Surfing the Third Wave of Ionic Liquids: A Brief Review on the Role of Surface-Active Ionic Liquids in Drug Development and Delivery. ChemMedChem, 16(17), 2604-2611.

[135]Egorova, K. S., Gordeev, E. G., & Ananikov, V. P. (2017). Biological activity of ionic liquids and their application in pharmaceutics and medicine. *Chemical reviews*, *117*(10), 7132-7189.

[136]Reichardt, C., & Welton, T. (2011). *Solvents and solvent effects in organic chemistry*. John Wiley & Sons.

[137]Weiß, N., Schmidt, C. H., Thielemann, G., Heid, E., Schröder, C., & Spange, S. (2021). The physical significance of the Kamlet–Taft π* parameter of ionic liquids. *Physical Chemistry Chemical Physics*, *23*(2), 1616-1626.

[138]Crowhurst, L., Mawdsley, P. R., Perez-Arlandis, J. M., Salter, P. A., & Welton, T. (2003). Solvent–solute interactions in ionic liquids. *Physical Chemistry Chemical Physics*, *5*(13), 2790-2794.

[139]Earle, M. J., Esperança, J. M., Gilea, M. A., Canongia Lopes, J. N., Rebelo, L. P., Magee, J. W., ... & Widegren, J. A. (2006). The distillation and volatility of ionic liquids. *Nature*, *439*(7078), 831-834.

[140]Greer, A. J., Jacquemin, J., Hardacre, C., & Keglevich, G. (2020). Industrial Applications of Ionic Liquids. *Molecules*, *25*(21).

[141]Cao, Y., & Mu, T. (2014). Comprehensive investigation on the thermal stability of 66 ionic liquids by thermogravimetric analysis. *Industrial & engineering chemistry research*, *53*(20), 8651-8664.

[142]MacFarlane, D. R., Forsyth, M., Izgorodina, E. I., Abbott, A. P., Annat, G., & Fraser, K. (2009). On the concept of ionicity in ionic liquids. *Physical chemistry chemical physics*, *11*(25), 4962-4967.

[143]Endres, F., & Zein El Abedin, S. (2006). Air and water stable ionic liquids in physical chemistry. *Physical chemistry chemical physics*, *8*(18), 2101-2116.

[144]Ueno, K., Tokuda, H., & Watanabe, M. (2010). Ionicity in ionic liquids: correlation with ionic structure and physicochemical properties. *Physical chemistry chemical physics*, *12*(8), 1649-1658.

[145]Ma, C., Laaksonen, A., Liu, C., Lu, X., & Ji, X. (2018). The peculiar effect of water on ionic liquids and deep eutectic solvents. *Chemical Society Reviews*, *47*(23), 8685-8720.

[146]Widegren, J. A., Laesecke, A., & Magee, J. W. (2005). The effect of dissolved water on the viscosities of hydrophobic room-temperature ionic liquids. *Chemical communications*, (12), 1610-1612.

[147]Buettner, C. S., Cognigni, A., Schröder, C., & Bica-Schröder, K. (2022). Surface-active ionic liquids: A review. Journal of Molecular Liquids, 347, 118160.

[148]Benedetto, A. (2023). Ionic liquids meet lipid bilayers: a state-of-the-art review. Biophysical Reviews, 15(6), 1909-1939.

[149]Blesic, M., Marques, M. H., Plechkova, N. V., Seddon, K. R., Rebelo, L. P. N., & Lopes, A. (2007). Self-aggregation of ionic liquids: micelle formation in aqueous solution. Green Chemistry, 9(5), 481-490.

[150]Dong, B., Li, N., Zheng, L., Yu, L., & Inoue, T. (2007). Surface adsorption and micelle formation of surface active ionic liquids in aqueous solution. Langmuir, 23(8), 4178-4182.

[151]Jiang, K., Liu, X., He, H., Wang, J., & Zhang, S. (2020). Insight into the formation and permeability of ionic liquid unilamellar vesicles by molecular dynamics simulation. Soft Matter, 16(10), 2605-2610.

[152]Israelachvili, J. N., Mitchell, D. J., & Ninham, B. W. (1976). Theory of self-assembly of hydrocarbon amphiphiles into micelles and bilayers. Journal of the Chemical Society, Faraday Transactions 2: Molecular and Chemical Physics, 72, 1525-1568.

[153]Muller, P. (1994). Glossary of terms used in physical organic chemistry. Pure Appl. Chem, 66(5), 1077-1184.

[154]Bharmoria, P., Rao, K. S., Trivedi, T. J., & Kumar, A. (2014). Biamphiphilic ionic liquid induced folding alterations in the structure of bovine serum albumin in aqueous medium. The Journal of Physical Chemistry B, 118(1), 115-124.

[155]Bharmoria, P., Mehta, M. J., Pancha, I., & Kumar, A. (2014). Structural and functional stability of cellulase in aqueous-biamphiphilic ionic liquid surfactant solution. The Journal of Physical Chemistry B, 118(33), 9890-9899.

[156]Singh, G., Kamboj, R., Mithu, V. S., Chauhan, V., Kaur, T., Kaur, G., ... & Kang, T. S. (2017). Nicotine-based surface active ionic liquids: Synthesis, self-assembly and cytotoxicity studies. Journal of colloid and interface science, 496, 278-289.

[157]Jiao, J., Han, B., Lin, M., Cheng, N., Yu, L., & Liu, M. (2013). Salt-free catanionic surface active ionic liquids 1-alkyl-3-methylimidazolium alkylsulfate: aggregation behavior in aqueous solution. Journal of colloid and interface science, 412, 24-30.

[158]Rao, K. S., Trivedi, T. J., & Kumar, A. (2012). Aqueous-biamphiphilic ionic liquid systems: self-assembly and synthesis of gold nanocrystals/microplates. The Journal of Physical Chemistry B, 116(49), 14363-14374.

[159]Mitchell, D. J., & Ninham, B. W. (1981). Micelles, vesicles and microemulsions. Journal of the Chemical Society, Faraday Transactions 2: Molecular and Chemical Physics, 77(4), 601-629.

[160]Jiao, J., Dong, B., Zhang, H., Zhao, Y., Wang, X., Wang, R., & Yu, L. (2012). Aggregation behaviors of dodecyl sulfate-based anionic surface active ionic liquids in water. The Journal of Physical Chemistry B, 116(3), 958-965.

[161]Brown, P., Butts, C., Dyer, R., Eastoe, J., Grillo, I., Guittard, F., ... & Heenan, R. (2011). Anionic surfactants and surfactant ionic liquids with quaternary ammonium counterions. Langmuir, 27(8), 4563-4571.

[162]Rao, K. S., Gehlot, P. S., Gupta, H., Drechsler, M., & Kumar, A. (2015). Sodium bromide induced micelle to vesicle transitions of newly synthesized anionic surface active ionic liquids based on dodecylbenzenesulfonate. The Journal of Physical Chemistry B, 119(11), 4263-4274.

[163]Sun, L., Gong, J., Xu, B., Wang, Y., Ding, X., Zhang, Y., ... & Xu, B. (2022). Ion-specific effects on vesicle-to-micelle transitions of an amino acid surfactant probed by chemical trapping. Langmuir, 38(20), 6295-6304.

[164]Roy, A., Dutta, R., Banerjee, P., Kundu, S., & Sarkar, N. (2016). 5-methyl salicylic acid-induced thermo responsive reversible transition in surface active ionic liquid assemblies: a spectroscopic approach. Langmuir, 32(28), 7127-7137.

[165]Lone, M. S., Afzal, S., Chat, O. A., Aswal, V. K., & Dar, A. A. (2021). Temperature-and composition-induced multiarchitectural transitions in the catanionic system of a conventional surfactant and a surface-active ionic liquid. ACS omega, 6(18), 11974-11987.

[166]Curreri, A. M., Mitragotri, S., & Tanner, E. E. (2021). Recent advances in ionic liquids in biomedicine. Advanced Science, 8(17), 2004819.

[167]Pal, A., & Yadav, A. (2016). Binding interactions of anesthetic drug with surface active ionic liquid. Journal of Molecular Liquids, 222, 471-479.

[168]Kulshrestha, A., Gehlot, P. S., & Kumar, A. (2020). Magnetic proline-based ionic liquid surfactant as a nano-carrier for hydrophobic drug delivery. Journal of materials chemistry B, 8(15), 3050-3057.

[169]Tahara, Y., Morita, K., Wakabayashi, R., Kamiya, N., & Goto, M. (2020). Biocompatible ionic liquid enhances transdermal antigen peptide delivery and preventive vaccination effect. Molecular pharmaceutics, 17(10), 3845-3856.

[170]Uddin, S., Islam, M. R., Chowdhury, M. R., Wakabayashi, R., Kamiya, N., Moniruzzaman, M., & Goto, M. (2021). Lipid-based ionic-liquid-mediated nanodispersions as biocompatible carriers for the enhanced transdermal delivery of a peptide drug. ACS applied bio materials, 4(8), 6256-6267.

[171]Kumar, R. A., Papaïconomou, N., Lee, J. M., Salminen, J., Clark, D. S., & Prausnitz, J. M. (2009). In vitro cytotoxicities of ionic liquids: effect of cation rings, functional groups, and anions. Environmental Toxicology: An International Journal, 24(4), 388-395.

[172]Cook, K., Tarnawsky, K., Swinton, A. J., Yang, D. D., Senetra, A. S., Caputo, G. A., ... & Vaden, T. D. (2019). Correlating lipid membrane permeabilities of imidazolium ionic liquids with their cytotoxicities on yeast, bacterial, and mammalian cells. Biomolecules, 9(6), 251.

[173]García, M. T., Bautista, E., de la Fuente, A., & Pérez, L. (2023). Cholinium-based ionic liquids as promising antimicrobial agents in pharmaceutical applications: surface activity, antibacterial activity and ecotoxicological profile. Pharmaceutics, 15(7), 1806.

[174]García, M. T., Bautista, E., Pérez, L., & Vázquez, S. (2025). Self-assembly, antimicrobial properties and biodegradability of ester-functionalized choline-based surface-active ionic liquids. Molecules, 30(6), 1280.

[175]Coleman, D., & Gathergood, N. (2010). Biodegradation studies of ionic liquids. Chemical Society Reviews, 39(2), 600-637.

[176]Pham, T. P. T., Cho, C. W., & Yun, Y. S. (2010). Environmental fate and toxicity of ionic liquids: a review. Water research, 44(2), 352-372.

[177]Mustahil, N. A., Baharuddin, S. H., Abdullah, A. A., Reddy, A. V. B., Mutalib, M. I. A., & Moniruzzaman, M. (2019). Synthesis, characterization, ecotoxicity and biodegradability evaluations of novel biocompatible surface active lauroyl sarcosinate ionic liquids. Chemosphere, 229, 349-357.

[178]Jordan, A., & Gathergood, N. (2015). Biodegradation of ionic liquids–a critical review. Chemical Society Reviews, 44(22), 8200-8237.

[179]Boethling, R. S., Sommer, E., & DiFiore, D. (2007). Designing small molecules for biodegradability. Chemical reviews, 107(6), 2207-2227.

[180]Paul, B. K. (2020). Unveiling the thermodynamic signature underlying the interaction of human serum albumin with sub-micellar concentrations of a surface active ionic liquid. Journal of Molecular Liquids, 318, 114078.

[181]Alves, M. M., Araujo, J. M., Martins, I. C., Pereiro, A. B., & Archer, M. (2021). Insights into the interaction of Bovine Serum Albumin with Surface-Active Ionic Liquids in aqueous solution. Journal of Molecular Liquids, 322, 114537.

[182]Sardar, R., Dutta, S., & Ghosh, S. (2026). Electrostatic control of protein–vesicle interactions in catanionic long-chain ionic liquid systems: insights from human serum albumin. Physical Chemistry Chemical Physics, 28(5), 3702-3720.

[183]Abujubara, H., Bharmoria, P., Raj, D., Alvarez, S. W., Liu, S., Zhylinskaya, M., ... & Tietze, A. A. (2026). Selective and Synergistic Targeting of ErbB2-Positive Cancer Cells with ErbB2 Transmembrane Peptide-Ionic Liquid Nanocarrier Formulation. *ACS Applied Materials & Interfaces*.

Appendix

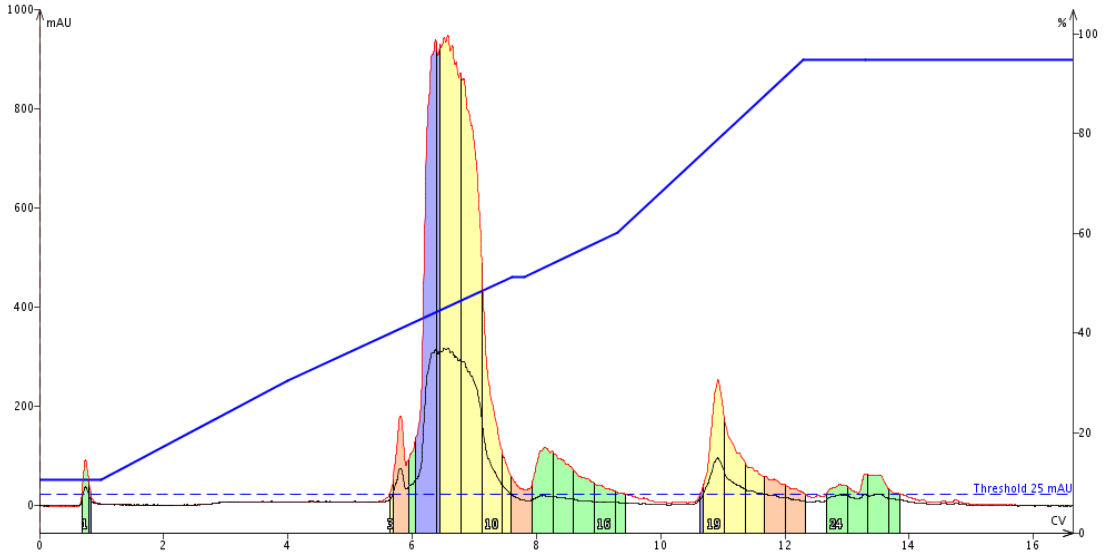


Figure S1. Purification of Nic MAIL using reversed-phase flash chromatography. Fractions from CV 7-10 were collected.

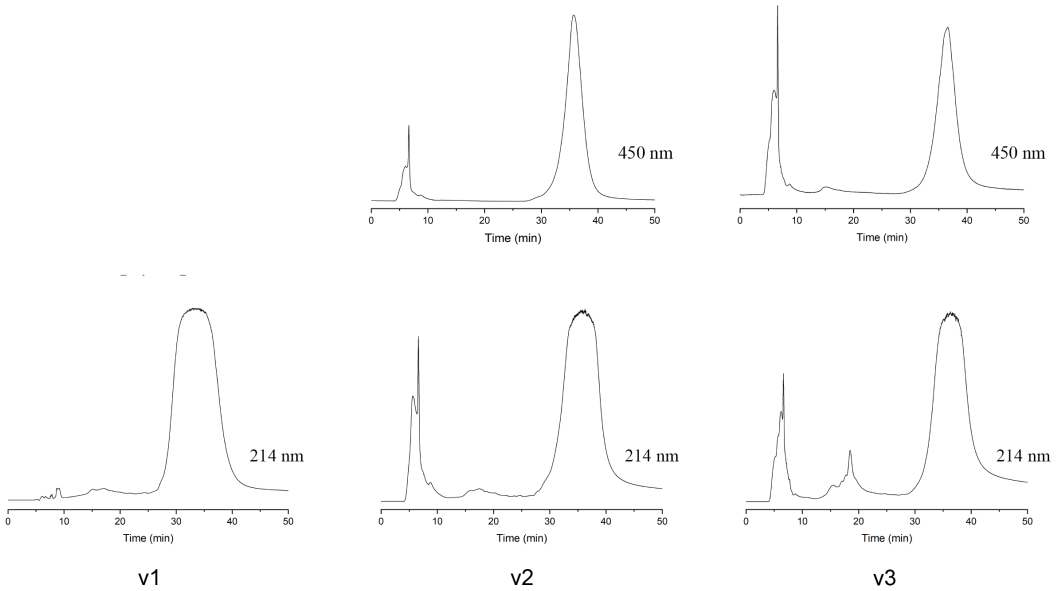


Figure S2. Preparative HPLC chromatograms at 214 nm and 450 nm of v1-v3 peptides.

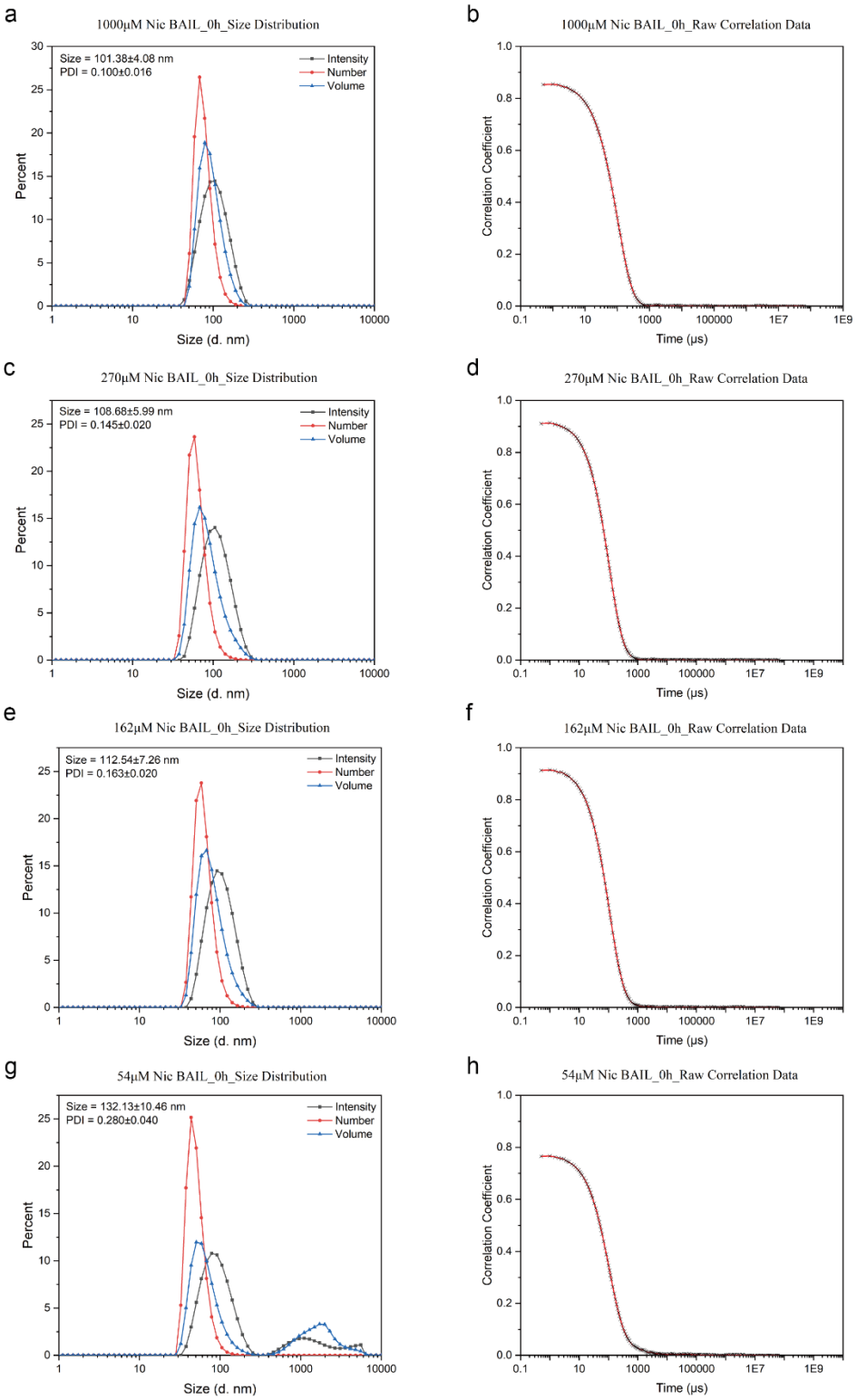


Figure S3. DLS profiles show the intensity, number and volume distribution of hydrodynamic size of Nic BAIL vesicles suspension at 1000 μM (a), 270 μM (c), 162 μM (e), and 54 μM (g) during step dilution with 10 mM pH7.4 PB at 25 ℃, with corresponding correlation coefficient vs decay time diagrams (b, d, f, h). Data are presented as mean ± SD (n=3).

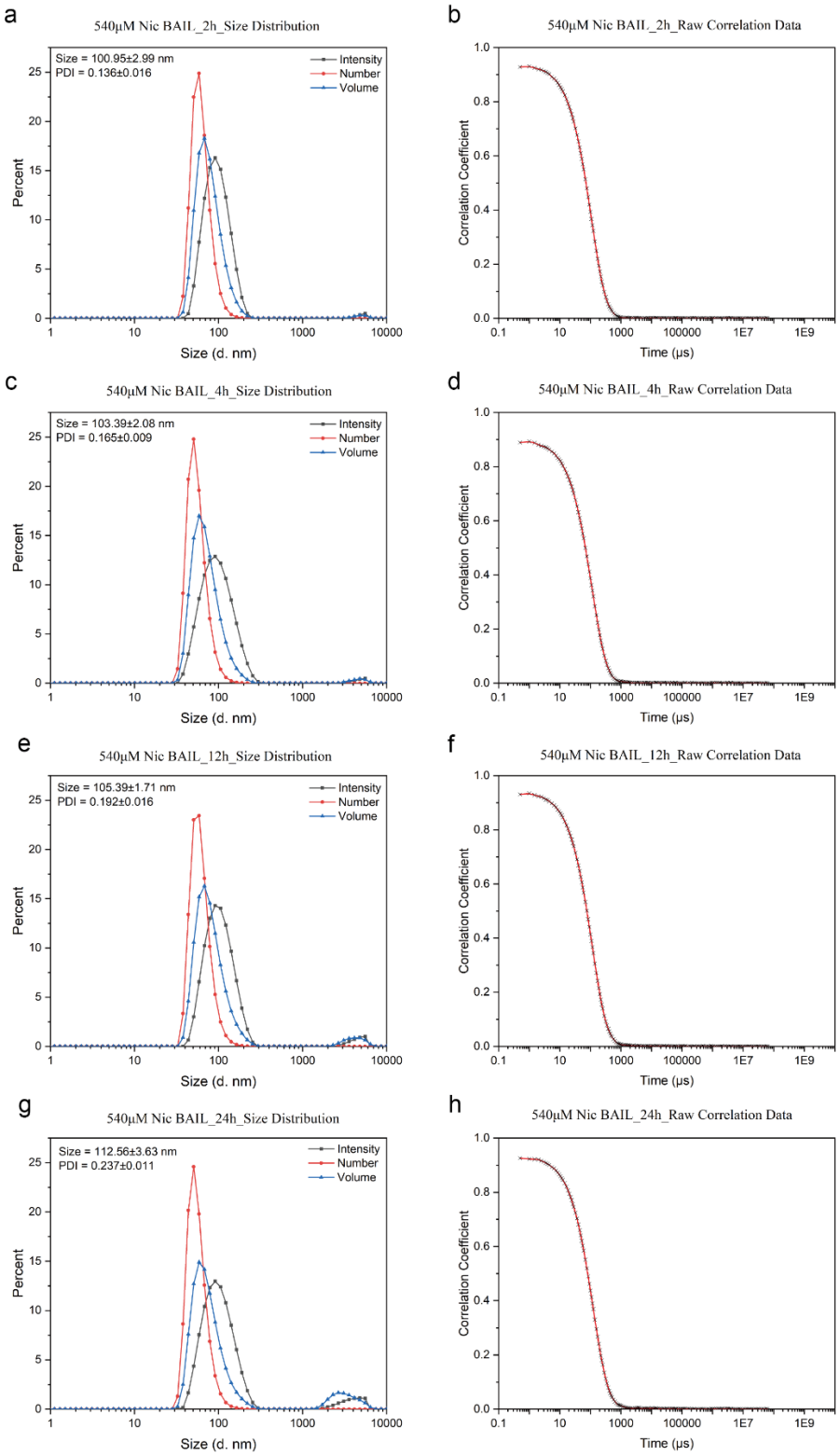


Figure S4. DLS profiles show the intensity, number and volume distribution of hydrodynamic size of Nic BAIL vesicles suspension in 10 mM pH7.4 PB stored at 25 ℃ for 2 h (a), 4 h (c), 12 h (e), and 24 h (g), with corresponding correlation coefficient vs decay time diagrams (b, d, f, h). Data are presented as mean ± SD (n=3).

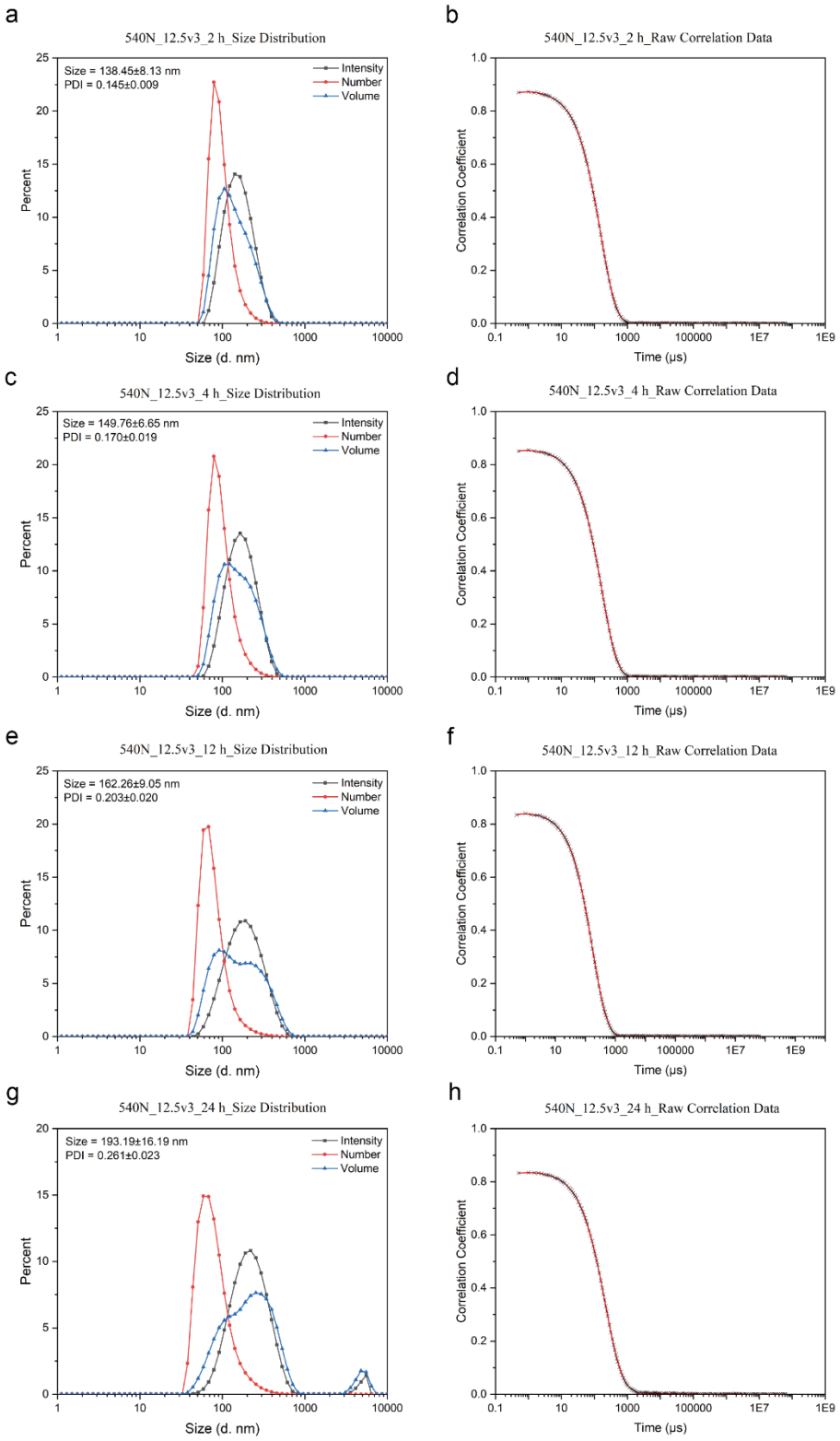


Figure S5. DLS profiles show the intensity, number and volume distribution of hydrodynamic size of 540 μM Nic BAIL-12.5 μM v3 nanoformulation in 10 mM pH7.4 PB stored at 25 °C for 2 h (a), 4 h (c), 12 h (e), and 24 h (g), with corresponding correlation coefficient vs decay time diagrams (b, d, f, h). Data are presented as mean ± SD (n=3).

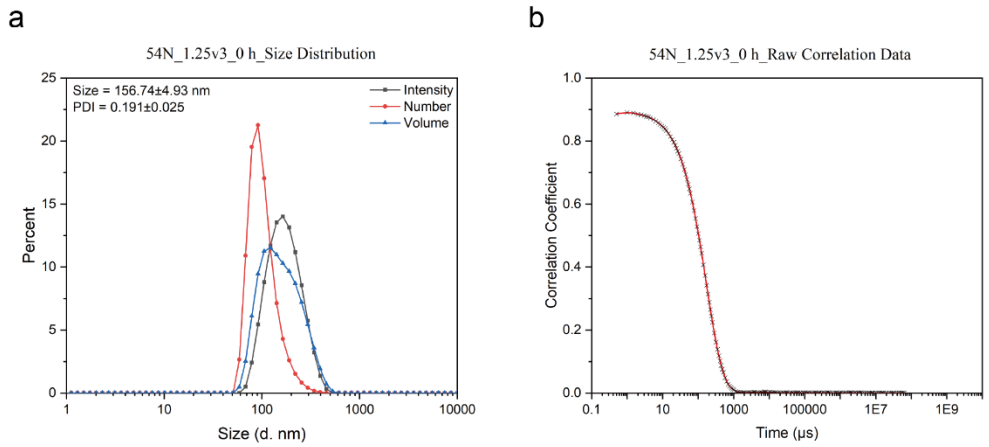


Figure S6. DLS profiles show the intensity, number and volume distribution of hydrodynamic size of the nanoformulation after direct dilution to working concentration of 54 µM Nic BAIL-1.25 µM v3 (a) with 10 mM pH7.4 PB at 25 ℃, with corresponding correlation coefficient vs decay time diagrams (b). Data are presented as mean ± SD (n=3).

Cell line	Cancer Type	Molecular Subtype	ERBB2 expression (RNA)	ERBB2 CRISPR effect
BT-474	Breast	HER2 overexpression	10.5	N/A
NCI-H23	Lung	-	3.2	-0.15

Table S1. ERBB2 RNA expression levels and CRISPR dependency scores of cancer cells sourced from the Cancer Dependency Map[183].

DEPARTMENT OF LIFE SCIENCES
CHALMERS UNIVERSITY OF TECHNOLOGY
Gothenburg, Sweden, 28 October 2026
www.chalmers.se



UNIVERSITY OF
GOTHENBURG



CHALMERS
UNIVERSITY OF TECHNOLOGY